Development of an Extreme Ultraviolet Frequency Comb for Precision Spectroscopy.

by

Dylan Yost

B.S., Colorado School of Mines, 2005

A thesis submitted to the

Faculty of the Graduate School of the

University of Colorado in partial fulfillment

of the requirements for the degree of

Doctor of Philosophy

Department of Physics

2011

This thesis entitled:
Development of an Extreme Ultraviolet Frequency Comb for Precision Spectroscopy.
written by Dylan Yost
has been approved for the Department of Physics

_____
Prof. Jun Ye

_____
Prof. Steven Cundiff

Date _____

The final copy of this thesis has been examined by the signatories, and we find that both the content and the form meet acceptable presentation standards of scholarly work in the above mentioned discipline.

Yost, Dylan (Ph.D., Physics)

Development of an Extreme Ultraviolet Frequency Comb for Precision Spectroscopy.

Thesis directed by Prof. Jun Ye

We describe an extreme-ultraviolet frequency comb produced via high repetition rate, intracavity high harmonic generation. The experimental apparatus consists of a high power frequency comb of 80 W average power, which excites a robust femtosecond enhancement cavity. On resonance, the enhancement cavity contains >8 kW of average power and is capable of driving the high harmonic process at a repetition rate of 154 MHz producing a frequency comb. More than 200 microwatts of XUV power is generated in each harmonic. While it is difficult to build a continuous wave laser below 100 nm, this source functions as millions of intrinsically calibrated narrow-linewidth sources in the XUV. With this unique radiation source, we were able to conduct high resolution, direct frequency comb spectroscopy on neutral argon atoms at a wavelength of 82 nm. This measurement demonstrates the efficacy of this technique for precision measurement.

Dedication

For Grace

Acknowledgements

When I was first came to work in Jun's lab, I was overwelmed by the energetic scientific atmosphere. As a new graduate student, I was obviously expecting the scientists at JILA to exhibit an unrivaled technical know-how and the propensity for rigorous scientific investigation. However, I was not expecting Jun's unbridled enthusiasm for science. For his guidance, scientific insights and friendship, I am very grateful.

Within my first year in the group, I was introduced to several postdocs and senior graduate students who selflessly took me under their wing. Jason Jones, Kevin Moll, Michael Thorpe, Seth Forman and Matthew Stowe were never too busy to provide guidance, or teach me something new. Within a few months of arriving in the group, I was working predominantly with Thomas Schibli on the XUV frequency comb project. In addition to being a thoughtful friend, I am extremely grateful to have gotten the chance to learn from Thomas, who possesses an unrivaled technical toolkit.

There is never a lack of talented post docs who come to do research in the Ye group. For the last few years of my time here I had the opportunity to work with two of the best, Arman Cingöz and Tom Allison. After Arman arrived, we decided to attempt to do spectroscopy with the XUV comb. While we had some challenges along the way, Arman never ran out of good ideas and was singularly focused until we finally had success. Tom joined us along the way and provided us with a needed boost of new ideas and tirelessly worked to improve the experiment and understand the enhancement cavity at a deeper level.

I would also like to thank our collaborators. Axel Ruehl, Ingmar Hartl and Martin Fermann at IMRA America provided us with the high power frequency comb without which the

vi

experiments in this thesis would not have been possible. Jennifer L. Tate, James Hostetter, Mette B. Gaarde and Kenneth J. Schafer provided us with exceptional theoretical support in our joint work to understand the mechanisms behind below-threshold harmonic generation.

Throughout my time in the Ye group, we worked closely with the IR frequency comb sub-group– Kevin Cossel, Florian Adler, Piotr Maslowski, Aleksandra Foltynowicz-Matyba, Ticijana Ban and Travis Briles. In our shared weekly group meetings, these individuals offered countless helpful suggestions for our experiment. There are now several new members in the frequency comb subgroup– Adam Fleisher, Bryce Bjork, and Craig Benko. It is already clear that in their hands the future of the XUV and IR frequency combs will be very safe.

Of course, during my time in Jun's group everyone has offered invaluable support to our experiment for which I am very grateful. By name, these individuals are Mike Bishof, Sebastian Blatt, Ben Bloom, Marty Boyd, Gretchen Campbell, Amodsen Chotia, Matt Hummon, Ben Lev, Andrew Ludlow, Marcio Miranda, Travis Nicholson, Silke Ospelkaus, Avi Pe'er, Brian Sawyer, Ben Stuhl, Matt Swallows, Dajun Wang, Jason Williams and Mark Yeo. All these individuals have been incredible assets and have always provided careful, thoughtful assistance. Mike Martin needs special mention both because he has, at times, provided very direct assistance to the XUV frequency comb project and has always been willing to discuss our experimental problems.

The instrument and electronics shops in JILA are the envy of scientific institutions around the world. We obviously would not have been able to complete the experiments discussed in this thesis without the diligent help of these extremely talented individuals. In the electronics shop, I am very grateful for the continued support provided by Terry Brown, James Fung-A-Fat, Carl Sauer, David Tegart and Mike Whitmore. I especially appreciate Terry's tireless enthusiasm and his careful explanations that have been so beneficial to my understanding of electronics. In the instrument shop, I would like to thank Dave Alchenberger, Todd Asnicar, Tom Foote, Hans Green, Kim Hagen, Blaine Horner, Tracy Keep, and Ariel Paul.

Jan Hall has always been available to offer sound advice on our experimental challenges. When we performed XUV spectroscopy of argon, Jan provided us with light from his cavity stabilized laser which helped to enable the experiment. Jan's enthusiasm for the most technical aspects of an experiment has created a unique heritage at JILA that I am glad to have experienced.

Finally, I would like to thank my family. My parents, Kevin and Sandy, and my brother Brendan have been a neverending source of encouragement throughout my entire education. Also, I would like to thank my wife Grace who has sacrificed a great deal while I was in graduate school. I am sure I could not have made it through without her constant support.

Contents

Chapter

Tables

Table

Figures

Figure

Chapter 1

Introduction

In the history of laser development, there have customarily been two distinct research communities with largely divergent goals. In fact, this dichotomy has existed from the very birth of the field. It was then, in 1960, that Theodore Maiman reported the first laser– a pulsed source with ruby as the gain medium [1]. This demonstration effectively created the field of nonlinear optics and initiated the development of increasingly powerful, short pulsed lasers. Conversely, in 1961, Ali Javan reported the first continuous-wave laser (the HeNe gas laser) [2], which initiated the field of laser spectroscopy whose practitioners have since strived to develop lasers with increasing spectral purity. Only in recent years have new fields arisen which must draw from the technical advancements of both communities. This thesis describes the development of an extreme ultraviolet (XUV) frequency comb, which is a prime example of one of these new, hybrid fields. Its development depends critically on the precise control of a seemingly violent nonlinear interaction, high harmonic generation (HHG), to produce a short-wavelength, temporally coherent source. Therefore, it is difficult to classify this work into either of the research communities. Instead, it rather exemplifies the symbiotic relationship which has arisen between the two groups in recent years. The motivation for building an XUV frequency comb is to help extend the techniques of laser spectroscopy to short-wavelength regions of the electromagnetic spectrum. While a seemingly humble goal, the scientific worth of such an endeavor could be inestimable when one considers the analogous developments of laser spectroscopy in the visible and infrared spectral domains.

Before the advent of the laser, scientists were aware from their experience in microwave spectroscopy that there were distinct advantages in terms of both sensitivity and resolution when one utilized a narrow-linewidth, stable radiation source for spectroscopy instead of a dispersive spectrometer [3]. Therefore, the scene was set for dramatic scientific advance once narrow-linewidth, visible radiation sources became available. After the first laser demonstrations, there was soon rapid development in the field of precision spectroscopy including intracavity Lamb-dip stabilization, narrow resonance reference cavities, saturated absorption spectroscopy and other Doppler-free techniques [4–6]. With these developments, the obtainable resolution and precision with laser spectroscopy quickly outpaced conventional spectrometers laying the groundwork for subsequent progress in the field of laser cooling and ultracold atoms [7].

With these ground-breaking developments, scientists began to attempt to link their spectroscopic measurements to the Cesium-133 rf frequency standard. However, optical frequencies are too high to be counted electronically and therefore the link from optical frequencies to the rf required frequency chains– incredibly complex systems of multiple lasers linked through optical frequency conversion and rf comparisons [8–11]. In 1983, through the use of frequency chains, the meter was redefined through the speed of light and the definition of the second– inexorably linking the measurement of length to the Cesium frequency standard [12]. This also defined the standard against which precision spectroscopy would be held in the future; true accuracy in optical spectroscopy would require a link to the radio-frequency standards. Therefore, any accurate measurement of an optical frequency would require a complicated and expensive frequency chain.

While laser spectroscopists were developing precision tools for spectroscopy, the pulsed laser community had been producing intense lasers with increasingly short pulse durations for nonlinear and time-resolved studies without a focus on the linewidth or frequency stability of their sources *per se*. The advances in short pulse phenomena had been startling with several dye laser systems in the 1980's demonstrating pulse durations in the femtosecond regime

[13–16]. With the first demonstration of Kerr-lens modelocking, femtosecond lasers became increasingly robust [17]. Finally, with the techniques of chirped pulse amplification [18] and nonlinear techniques like high harmonic generation it was possible to generate optical pulses only hundreds of attoseconds long [19], demonstrating incredible temporal resolution for time-resolved studies. Intriguingly, the solution to the difficulties faced by the laser spectroscopists in linking their measurements to the rf through frequency chains arose, in part, from techniques developed by the short-pulse laser community.

These advances ultimately resulted in the development of the optical frequency comb in the late 1990's [20–25], which has now completely supersceded the frequency chain technique (to the relief of many spectroscopists). The frequency comb arose from the realization that if one takes a pulsed laser such as a Kerr-lens modelocked laser and stabilizes the phase and timing between pulses, in the frequency domain, such a pulsed laser produces a comb of frequencies which can be described by $\nu_n = n f_r + f_0$. Here ν_n is an optical frequency, f_r and f_0 are rf frequencies and n is an integer. Therefore, this source relates optical frequencies to rf frequencies with ease. As techniques to stabilize these pulsed laser sources were developed, the field of laser spectroscopy was revolutionized since now frequency measurements could be made with incredible precision without the need for large, complicated and expensive frequency chains.

One of the main challenges left for precision spectroscopy lies with extending laser spectroscopy and the frequency comb technique to previously inaccessible wavelengths. Spectroscopic measurements in the extreme ultraviolet (XUV) spectral region are limited, in large part, because of the dispersive spectrometers available. Therefore spectroscopy in the XUV is in a very similar position as visible spectroscopy was before the 1960s. However, we have a great advantage in our attempts to extend ultrahigh precision spectroscopy to the XUV since we have the historic knowledge of the revolutionary developments in visible spectroscopy. We can follow that path by developing narrow-linewidth sources in the XUV and linking these sources to the rf frequency standards. However, to generate a laser-like source in the

extreme ultraviolet– especially one that has a broad spectral coverage and yet high spectral resolution– is a very challenging task. There are only a few gain media at these wavelengths which are suitable. Since most solid materials have significant oscillator strength in the XUV, only select gases or plasmas are sufficiently transparent to operate as a gain medium.

While challenging, the extension of ultrahigh resolution spectroscopy into the XUV will be revolutionary. Most two and three-body atomic systems have ground state transitions well into the XUV. For instance, the transition from the ground state to the first excited state in hydrogen lies at 121.5 nm. For helium, the $1s^2$-$1s2p$ transition is at 59 nm. The ground state transitions in hydrogen and helium-like ions are at even shorter wavelength and are currently quite unobtainable by traditional laser spectroscopy. Historically, the spectroscopic measurements of simple atomic systems such as these have provided a tremendous testbed for physical theories. The mapping of discrete spectral lines in atomic hydrogen revealed the necessity of a new theory of physics, Quantum Mechanics. The discovery of the Lamb shift led to the development of Quantum Electrodynamics (QED) [26]– the most successful theory in physics. Higher order QED corrections to the Lamb shift scale with powers of the atomic number and therefore spectroscopic measurements on helium and hydrogen-like ions could provide the most stringent tests of QED yet. Therefore, it is important that the study of simple atomic and ionic systems proceeds with increasing precision to provide a continued test of our best physical theories. In addition, the development of high precision laser spectroscopy in the XUV may prove crucial for the development of next-generation "nuclear" clocks [27–29] which could lead to advances in searches for spatial and temporal variation of fundamental constants [30, 31].

Due to the challenges of building a conventional laser outlined above, to achieve a laser-like source in the XUV, it seems that the best path forward is to utilize nonlinear interactions to convert a visible source. Frequency conversion can proceed by multiple, cascaded low-order harmonic processes (second-harmonic, third-harmonic and sum-frequency generation). However, when beginning with a visible source, obtaining an XUV source

through these processes is cumbersome if not impossible. A more straightforward way is to generate XUV radiation through one extremely nonlinear interaction- high harmonic generation. This process requires extremely high intensities ($> 10^{13}$ W/cm^2) that are only attainable with pulsed lasers. Thus, the most natural solution, satisfying this requirement and obtaining a narrow bandwidth source simultaneously, is the extension of the frequency comb technology to the XUV. In analogy with visible frequency comb development, these techniques will once again be forced to borrow heavily from the advances made by the ultrashort pulsed laser community, but this time in the areas of high harmonic generation and attosecond physics. Once produced, the XUV frequency comb can then be used directly for spectroscopy through the techniques of direct frequency comb spectroscopy (DFCS) [32]. Therefore, two significant breakthroughs for visible laser spectroscopy discussed above can be accomplished elegantly in one step.

The most obvious challenge to the creation of an XUV frequency comb through the HHG process is the very large peak intensity of $> 10^{13}$ W/cm^2 required in the fundamental frequency comb. In the field of intense light/matter interactions, this challenge has traditionally been overcome by decreasing the pulse rate of the modelocked laser driving the process so that the requirements on the average power of the laser are not too high. For example, a 1 kHz repetition rate, 1 mJ pulse energy laser will only have 1 W of average power but can easily reach the high intensity required for HHG if the pulse duration is below 100 fs and the beam is focused to less than 0.1 mm^2. However, to generate a frequency comb, temporal coherence must be maintained between pulses in the pulse train, which is very difficult to do with pulses that are arriving so infrequently. An equivalent way of stating this is that since the frequency comb spacing is given by the repetition rate, it is required that a 1 kHz frequency comb have individual comb linewidths of less than 1 kHz– a condition that cannot be met easily with any stabilized pulsed laser system. In addition, spectroscopic measurements utilizing DFCS proceed much more easily with a frequency comb produced from a high repetition rate source since: 1) Allowed transitions have broad linewidths, and

the frequency comb spacing must be larger than the transition width to resolve structure; 2) If multiple lines are excited simultaneously a widely spaced frequency comb can make the spectroscopic signal more easily interpreted; 3) In determining the absolute frequency of a transition a high repetition rate is technically convenient.

Therefore, most frequency combs have repetition rates in the 100 MHz to 1 GHz range. The average power required to drive the harmonic process at $\sim$100 MHz repetition rate can easily exceed several kilowatts and seems to present a significant barrier to the production of an XUV frequency comb. A major step forward in this regard came in 2005 with enhancement-cavity-assisted HHG [33, 34]. However, major hurdles remained in the useability of these sources and real world spectroscopic applications were unobtainable. Shortly after, the optical Ramsey technique was demonstrated in the vacuum ultraviolet [35] and extreme ultraviolet [36]. This technique is similar to the comb technique but cannot achieve ultrahigh resolution or the direct frequency link (which eliminates many systematic errors) offered by a true frequency comb measurement.

This thesis will address the continued development of the XUV frequency combs produced through femtosecond enhancement cavities. With the achievements detailed here we were able to dramatically increase the XUV power produced by our system and conduct coherence measurements both in the vacuum ultraviolet and extreme ultraviolet, confirming our frequency comb structure at these wavelengths. This work ultimately led to a DFCS measurement in neutral argon at a wavelength of 82 nm potentially opening the door for a wide array of ultrahigh resolution spectroscopy below 100 nm.

The rest of this chapter addresses the fundamentals of frequency combs and high harmonic generation with a focus on our ultimate goal of producing an XUV frequency comb. With this ground work laid, there are four chapters which discuss the femtosecond enhancement cavity, our experimental apparatus, the phase noise of the harmonic frequency comb, and our efforts to increase the average power of this source, respectively. This thesis culminates in the final chapter which discusses XUV direct frequency comb spectroscopy and

absolute frequency determination in argon at 82 nm.

1.1   Frequency combs

The frequency comb has had an impact on science and technology, which would have been impossible to predict immediately after the first demonstrations [20–22, 24]. As mentioned above, the utility of the frequency comb arises from its ability to provide a direct link from radio frequencies to optical frequencies. It performs this function very robustly and without major systematic effects which has led to a seemingly endless supply of new and diverse applications. A few of these include broadbandwidth spectroscopy for molecular fingerprinting [37], the production of cold polar molecules [38], the search for extrasolar planets [39], the generation of ultralow phase noise microwave signals and optical atomic clocks [40]. While there are a multitude of uses for the frequency comb, for our purposes we will focus primarily on the application for which it was originally developed– to link spectroscopic measurements to the rf frequency standards.

1.1.1   Fourier transform of a pulse train

Here, we perform the Fourier transform of a stabilized pulse train in order to derive the frequency spectrum. This formalism will be useful in gaining intuition regarding the frequency comb and the generation of an XUV frequency comb in the next section on high harmonic generation. Consider the pulse train which is emitted from a femtosecond pulsed laser (for example a Ti:Sapp modelocked laser). The train of pulses emitted will usually have a fairly regular repetition frequency, and the phase of the pulses will evolve in a roughly uniform fashion. Imagine that we stabilize both the repetition frequency and the pulse train's phase evolution perfectly (of course a real system will also possess noise in both these degrees of freedom). The mathematical representation of an infinite, stabilized pulse train

in the time domain can be written as

$$E(t) = E_0 \sum_{n=-\infty}^{\infty} e^{-(t-nt_r)^2/\tau^2} e^{i\omega_c t}. \tag{1.1}$$

where t_r is the time between pulses, τ is the pulse width and ω_c is the carrier frequency (the relationship $\omega_q = 2\pi f_q = \frac{2\pi}{t_q}$, relating frequency, angular frequency and period will be used several times without further explanation). A gaussian pulse shape is assumed for convenience but is not crucial for the relevent results. To do the Fourier transform of this field it is easier if we write it in terms of functions which have well known Fourier transforms.

$$E(t) = E_0 \left[\mathrm{comb}(t, t_r) * \mathrm{gauss}(t, \tau) \right] e^{i\omega_c t}. \tag{1.2}$$

Here the comb function is defined as

$$\mathrm{comb}(x, y) = \sum_{n=-\infty}^{\infty} \delta(x - ny), \tag{1.3}$$

the gaussian function is defined as

$$\mathrm{gauss}(x, y) = e^{-x^2/y^2}, \tag{1.4}$$

and "$*$" is the convolution operator. This form allows us to take the Fourier transform very easily if we know the transforms of the individual parts. It may not be immediately obvious what the transform of the $\mathrm{comb}(t, t_r)$ function is but it is easily derived as follows:

$$\mathcal{F}[\mathrm{comb}(t, t_r)] = \frac{1}{\sqrt{2\pi}} \int_{-\infty}^{\infty} dt\, e^{-i\omega t} \sum_{n=-\infty}^{\infty} \delta(t - nt_r) = \frac{1}{\sqrt{2\pi}} \sum_{n=-\infty}^{\infty} e^{-i\omega n t_r}. \tag{1.5}$$

If this final sum was approximated as an integral, the answer would be a dirac delta function. However, since it is a sum, we know that the delta function must repeat in the frequency domain with period $\frac{2\pi}{t_r}$; i.e. another comb function. Therefore, we find

$$\mathcal{F}[\mathrm{comb}(t, t_r)] \propto \mathrm{comb}(\omega, \frac{2\pi}{t_r}). \tag{1.6}$$

With this relation, it is trivial to determine the transform of equation 1.2.

$$\mathcal{F}[E(t)] = \tilde{E}_0 \left[\mathrm{comb}(\omega - \omega_c, \omega_r)\, \mathrm{gauss}(\omega - \omega_c, \frac{1}{4\tau}) \right]. \tag{1.7}$$

Here, $\tilde{E}_0$ encompasses several amplitude factors not taken into account explicitly.

It is clear that the Fourier transform of the pulse train is a comb of frequencies offset by the carrier frequency. A quick look back, shows that the frequency comb is a direct consequence of the repeating envelope function. The pulse shape is not crucial for the resulting frequency comb structure. A different shape of the pulses in the time domain would just lead to a different distribution of spectral power with the underlying comb function remaining unaffected. Therefore, the crucial ingredient to generate a frequency comb is that the envelope function, whatever it is, repeats exactly every repetition period, t_r. If this is not the case, then the comb teeth will have some finite width instead of being represented by delta functions.

If we are just concerned with the portion of equation 1.7 that gives the frequency comb structure, $\text{comb}(\omega - \omega_c, \omega_r)$, we notice that one parameter is the carrier frequency ω_c which is an optical frequency. This equation is inconvenient since we want to define the comb in terms of rf frequencies. However, since the comb function is a periodic function, we are at liberty to perform the following shift in our definition; $\text{comb}(\omega - \omega_c, \omega_r) \Rightarrow \text{comb}(\omega - \omega_c + p\omega_r, \omega_r)$, where p is an integer. For convenience, we define $\omega_o = \omega_c - p\omega_r$ where p is a large integer chosen so that $0 < \omega_o < \omega_r$. This is equivalent to the definition $\omega_o = \text{Remainder}(\frac{\omega_c}{\omega_r})$. The comb function can then be written out explicitly as

$$\text{comb}(\omega - \omega_0, \omega_r) = \sum_{n=-\infty}^{\infty} \delta[(\omega - \omega_0) - n\omega_r], \tag{1.8}$$

which shows that allowed frequencies are given by $\omega_n = n\omega_r + \omega_o$. This defines the underlying frequency comb structure with just two rf frequencies.

If we had spectral power all the way to dc, the frequency ω_0 could be understood as the offset of the first comb mode from zero. It is also easy to understand how the offset frequency, ω_0, is manifested in the pulse train in the time domain with a small amount of algebra.
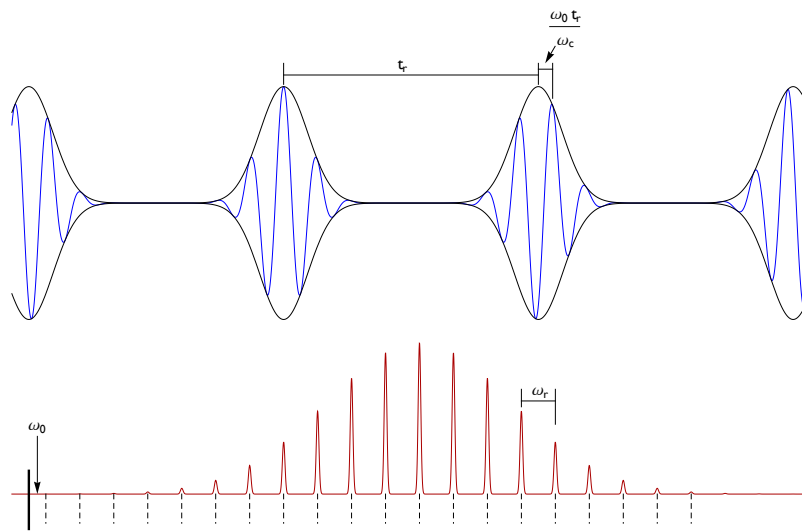
Figure 1.1: Example of a pulse train with an evolving phase and the corresponding frequency comb in the Fourier domain. Shown in the plot are ω_0 which is the offset of the frequency comb from dc, t_r which is the repetition period of the pulse train and $\mathrm{Remainder}(\frac{t_r}{t_c}) = \frac{\omega_0 t_r}{\omega_c}$ which is the timing difference between the peak of the pulse envelope and the peak of the electric field.

$$\omega_o = \text{Remainder}(\frac{\omega_c}{\omega_r}) = \text{Remainder}(\frac{t_r}{t_c})\frac{\omega_c}{t_r}, \tag{1.9}$$

$$\Rightarrow \text{Remainder}(\frac{t_r}{t_c}) = \frac{\omega_0 t_r}{\omega_c}. \tag{1.10}$$

The quantity $\text{Remainder}(\frac{t_r}{t_c})$ is easily identifiable by inspection as the slip in time of the peak of the envelope function from the peak of the underlying carrier from pulse to pulse as shown in Figure 1.1. Therefore, our physical understanding of the quantity ω_0 is that it is the direct result of an evolving phase underneath the pulse envelope function. Usually the quantity $\text{Remainder}(\frac{t_r}{t_c})\omega_c$ is defined as $\Delta\phi$ which can be understood as the phase slip between the pulse envelope and underlying carrier frequency. This gives $f_0 = \frac{\Delta\phi f_r}{2\pi}$ which is the most common definition of f_0, also known as the carrier envelope offset frequency.

1.1.2   Detecting the offset frequency

To experimentally realize a frequency comb in the lab, one must usually detect and stabilize the f_0 and f_r frequencies. To detect f_r is relatively easy since the repetition rate can be measured simply by detecting the pulse train with a photodiode. To detect the offset frequency is more difficult and it was the development of the self-referencing techniques that could produce a beatnote at the offset frequency that truly enabled frequency comb applications [20, 21].

An f-2f interferometer is the most basic and most commonly implemented self-referencing technique [20]. In this technique, the frequency comb must have an octave of spectrum. Femtosecond oscillators which span a whole octave of bandwidth are relatively uncommon although some have been demonstrated [41, 42]. Therefore, the normal way to achieve an octave of bandwidth for an f-2f beatnote is by broadening the spectrum of a short pulse in a microstructured fiber [43]. These fibers are specially designed to have zero group-velocity dispersion at the center wavelength of the pulse and a small core (≈ 2 μm). With the radi-

ation concentrated to such a small area (along with the dispersion properties of the fiber), there can be substantial nonlinear interactions (namely self-phase modulation, 4-wave mixing and Raman scattering) which can increase the spectral content of the pulse to cover an octave of bandwidth.

With an octave of bandwidth generated, it is possible to double the long wavelength side of the comb which will spectrally overlap with the short wavelength side of the original comb. The beatnote between the combs will have a strong component at f_0.

We can understand this process through the formalism above if we assume Gaussian transform limited pulses. This is highly unlikely when broadening a pulse in a fiber but it still gives a feel for the problem. By squaring equation 1.2 we obtain:

$$E^{(2)}(t) = E_0^{(2)} \left[\text{comb}(t, t_r) * \text{gauss}(t, \tau/\sqrt{2})\right]e^{i2\omega_c t}. \tag{1.11}$$

To obtain the ω_o frequency, the fundamental and harmonic combs are interfered and detected on a photodiode with a resulting intensity given by

$$I(t) = I_0 + I_b(t) \propto \left|E(t) + E^{(2)}(t)\right|^2, \tag{1.12}$$

$$I_b(t) \propto E^* E^{(2)} + E E^{(2)*}, \tag{1.13}$$

where the relevant time dependent signal of the beatnote is given by I_b. In the time domain this signal is explicitly given by

$$I_b = E_0 E_0^{(2)} \left[\text{comb}(t, t_r) * \text{gauss}(t, \tau/\sqrt{3})\right](e^{i\omega_c t} + e^{-i\omega_c t}). \tag{1.14}$$

Taking the Fourier transform of this intensity profile gives the following beatnote signal in the frequency domain,

$$I_b = E_0 E_0^{(2)} \text{ gauss}(\omega - \omega_c, \tau/\sqrt{3})[\text{comb}(\omega - \omega_o, \omega_r) + \text{comb}(\omega + \omega_o, \omega_r)]. \tag{1.15}$$

The intensity function in the frequency domain is shifted by the offset frequency giving a detectable signal at ω_o. Note that the intensity envelope of the comb function is also

13
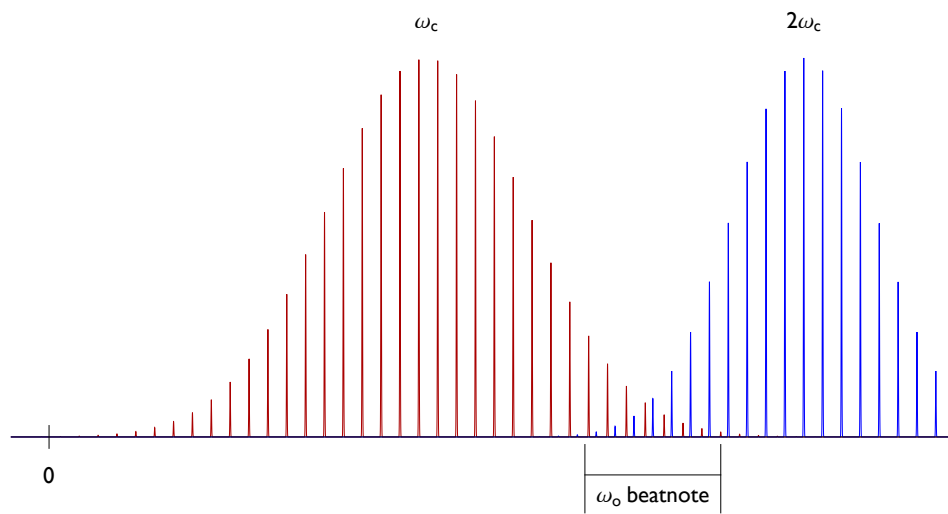
Figure 1.2: Pictorial example of an interferometer to detect the ω_o beatnote. The fundamental comb is centered around ω_c and shown in red and the second-harmonic comb is centered around $2\omega_c$ and shown in blue. The ω_0 beatnote signal is only obtained from a region where there is spectral overlap between the two frequency combs. A heterodyne beatnote arises between the neighboring comb modes of the two combs.

shifted by the carrier frequency. This means that for there to be any detectable rf frequency, the width of this envelope must reach all the way to near zero frequency where the offset frequency can be counted by traditional means. In other words, the spectrum of the fundamental comb must be large and therefore τ must be on the same order as $1/\omega_c$ for there to be an appreciable signal. This is fundamentally the same as requiring an octave spanning spectrum.

The operation of the f-2f interferometer can also be understood in the frequency domain and is shown in figure 1.2. The figure shows the electric field components of a frequency comb at the fundmental and the second harmonic of that frequency comb. The second harmonic of the frequency comb gives a comb structure define by $\omega_n^{(2)} = 2\omega_0 + n\omega_r$. Note that the offset frequency is doubled but the repetition rate is not (this is easily seen by considering the Fourier transform of equation 1.11). The difference frequencies between the two combs arising from the heterodyne beatnote will be given by $\omega_n^{(2)} - \omega_m = (n - m)\omega_r + \omega_0$. If we have an octave spanning spectrum then there will be overlapping spectrum at frequencies for which $n = m$ and a beatnote at ω_0 will result.

1.1.3   Control of the frequency comb

As seen in the previous section, it is possible to detect the rf frequencies f_r and f_0, fully defining the frequency comb. Not surprisingly, in a real laser system, the physical controls that we have on our laser system do not orthogonally control these frequencies. They instead adjust a linear combination f_r and f_0 [44]. In practice, this usually does not produce too many problems. If we have at least two frequency controls that are each controlling at least a different linear combination of f_r and f_0 (i.e. not completely degenerate degrees of freedom) then it is possible, at least in principle, to control the frequency comb completely. Usually, in stabilizing the frequency comb, it is often possible to ignore this detail and simply lock f_r using a single frequency control and then do the same for f_0 using the remaining frequency control. If the controls are nearly degenerate and the speed of the feedback loops

is of roughly the same magnitude then this can create feedback loop instabilities (colorfully known as the feedback loops "fighting each other") in which case some attempt should be made to orthogonalize the laser frequency controls on f_r and f_0.

One of the most obvious and useful frequency controls is the control of the length of the laser oscillator. This will adjust the timing between pulses in the pulse train (and thereby the repetition rate) and will usually have little effect on the pulse-to-pulse phase evolution. Remembering the definition of the offset frequency $f_0 = \frac{\Delta\phi f_r}{2\pi}$, it is clear then that a cavity length change will affect f_r and f_0 in nearly the same proportion. Other laser frequency controls will usually aim to control $\Delta\phi$ by changing the temporal dispersion within the laser cavity thereby changing predominantly f_0, although some small effect on f_r is also inevitable. In Ti:Sapp frequency combs, the intracavity dispersion is most often controlled by changing the pump power or by tilting a mirror in a spectrally dispersed portion of the laser cavity. In our fiber laser system, the dispersion is controlled by changing the pump power or the temperature of the output coupler (described in detail in Chapter 3). One point to keep in mind is that if a frequency comb is easily controlled with a certain parameter, free-running noise on that parameter will also cause noise in the frequency comb. For instance, it is imperative that the noise of our oscillator pump diode be as small as possible (as will be discussed in Chapter 4).

At many times, we are not concerned with the values of f_r and f_0 *per se*, but on the precise location and noise processes of the comb modes where there is optical power. Because these comb modes are defined by $\nu_n = n f_r + f_0$ where n is usually $\sim 10^4 - 10^7$, variations in the repetition frequency will have a much bigger effect on the comb modes in the optical domain than a similar change in f_0. Therefore, even though a cavity length change will affect both f_0 and f_r in exactly the same proportion, the effect in the optical domain will be dominated by the f_r change. If we consider a somewhat narrow bandwidth frequency comb, a change in the cavity length will seem to mostly move all the frequency comb modes together in concert. Of course the optical comb modes will also spread apart

from each other slightly (the spacing between the comb modes is defined by the repetition frequency). However this spreading motion will be barely perceptible at optical frequencies when compared to the shifting of all modes together.

If we consider another frequency control of our laser which predominantly affects f_0 through the temporal dispersion within the laser cavity, it is impossible to ignore the small change in f_r since its effect on the position of the optical comb modes can often be of the same order as the change in f_0. In fact the motion of the frequency comb in response to any of the varied ways to control the intracavity dispersion is usually best described by a fixed point formalism [44]. In that formalism, the spacing between the comb modes changes with actuation of the frequency control but there is a point in the frequency comb which is fixed because any motion at that point due to an f_r change is canceled by an associated f_0 change (this point may or may not lie within the bandwidth of the frequency comb). This motion can be visualized as a "breathing" about a fixed point. As an example, for a pure change in f_r, this fixed point is at dc. A pure change in f_0 results in a fixed point for at ∞. A real frequency actuator will not occur at either of these extremes and a method to change the intracavity dispersion can often result in a fixed point somewhere near the optical carrier.

1.1.4   Direct frequency comb spectroscopy

The use of frequency combs for spectroscopic applications often involve using a cw laser to excite a transition, with the comb simply acting to calibrate the absolute frequency of the cw laser. However, the techniques of direct frequency comb spectroscopy (DFCS) were developed to excite transitions directly with the frequency comb with no intermediate transfer laser [32]. These techniques have enabled intriguing new applications. The frequency comb has an incredibly broad bandwidth and this can be exploited in DFCS to perform massively parallel spectroscopy of many wavelengths simultaneously. This has tremendous advantage when it comes to molecular fingerprinting, for example [37]. Also, the frequency comb can couple an energy level to several others simultaneously. Therefore, it is possible

to control population and coherences through the adjustment of the phases of the frequency comb teeth coupling these states [45]. Finally, sometimes cw lasers are not available or convenient at a certain wavelength but that wavelength *is* accessible through a frequency comb. This last case applies to XUV frequency comb spectroscopy.

There are a number of challenges that can arise from direct comb excitation. A frequency comb can easily possess 10^4–10^6 comb teeth. If one tries to excite a single-photon transition and detect fluorescence, all comb teeth will contribute to the scattered photon background counts but only one comb tooth will contribute to the signal. This means that eliminating scatter from an DFCS experiment is much more crucial than in a cw spectroscopy experiment. The background problem is eliminated if one instead uses an absorption measurement but in that case the amplitude and shot-noise of the other frequency comb modes can quickly deteriorate signal. When exciting a two-photon transition with the frequency comb, pairs of comb modes centered at half the excitation energy can excite the transition. In this way, a much greater portion of the comb contributes to the signal. However, the dipole matrix elements for two-photon transitions are usually orders of magnitude lower than for single-photon transitions so scattered background will most likely still be a limitation.

The ability of the frequency comb to excite multiple transitions in an atom or molecule simultaneously is often an advantage, but it can also pose a difficulty when the signal to noise is low (as it is with XUV comb measurements). In the applications discussed for the XUV frequency comb in this thesis, the parallel spectroscopy of multiple transitions is not the goal, and multiple excitations simply produces an unwanted complication that must be taken into account (by using a high repetition rate laser, the signal is easier to interpret if multiple excitations occur).

1.1.5   Absolute frequency determination

Consider the simple case of exciting a single-photon transition with a frequency comb. To make an absolute frequency measurement with the comb, we need to determine the

frequency comb mode number with which we excite the transition. To accomplish this we must make at least two measurements of the transition frequency at different values of the repetition rate.

With two measurements we can solve for n.

$$n = \frac{f_{02} - f_{01} + \Delta n f_{r2} + \sqrt{2}\sigma}{f_{r1} - f_{r2}} \tag{1.16}$$

Here σ is the uncertainty in the extracted f_0 value for the two measurements (where here σ is taken to be the same for the two measurements). The integer Δn is the number of comb teeth that have scanned over the transition between our two measurements and we assume that we know this number exactly (for instance we have counted the number of times the transition has been excited). To successfully determine the mode number n, the uncertainty in the right hand side of the equation must be less than one. This means that if our measurement can only determine the line center to 1 MHz we must change the repetition rate of our laser by at least 1.4 MHz. For a 1 GHz repetition frequency comb, the laser cavity needs to be shortened/lengthened by 200 μm. For a 30 MHz frequency comb the laser cavity needs to be shortened/lengthened by 24 cm, most likely requiring a full realignment of the laser cavity. From this, a clear advantage of a high repetition rate frequency comb is evident.

It was assumed above that the integer Δn was known exactly. It is often impractical to count every comb tooth so an absolute frequency measurement will proceed through an algorithm which involves increasingly large jumps in the repetition frequency so that we can keep track of Δn. This process is described rigorously in the Chapter 6.

1.2   High harmonic generation

There is a conspicuous lack of lasers in the XUV. The difficulty in producing a laser with a wavelength below 100 nm can be understood, at least in part, through a common scaling argument [46]. To obtain population inversion in the XUV, the excitation rate in the gain medium must exceed the spontaneous emission rate. The spontaneous emission rate

of a transition is proportional ω^3 where ω is the carrier frequency. Additionally, the power required for a given excitation rate is proportional to ω (which is just the photon energy required to bridge the energy gap). In the XUV, ω is roughly an order-of-magnitude larger than in the visible so obtaining population inversion requires power roughly 10^4 times higher than in the visible. This along with the lack of transparent solid material in the XUV help to explain why there are so few lasers operating below 100 nm (for a few examples see [47–49]) and why they have found little utility in laser spectroscopy. To satisfy the technical definition of a laser, a device must rely on the stimulated emission of radiation. However, we are only concerned with certain properties of the generated radiation and not with the mechanism. Namely, the temporal coherence and collimation of the radiation must be equivalent to that which can be obtained in a laser. For this purpose, nonlinear conversion of a visible or infrared laser source into the XUV is also perfectly adequate.

The starting point for much of nonlinear optics is a perturbative ansatz which describes the interaction of matter with an intense electromagnetic field.

$$P(t) = \chi^{(1)}E(t) + \chi^{(2)}E^2(t) + \chi^{(3)}E^3(t)... \tag{1.17}$$

Here P is the dipole moment per unit volume or polarization, E is the electric field and $\chi^{(n)}$ are the nonlinear susceptibilities. This perturbative description is valid as long as the series converges. Perhaps, the most elementary phenomena, which can be gleaned from equation 1.17, is second harmonic generation. In this process, radiation of frequency ω is incident on a material with a non-negligible $\chi^{(2)}$ such that the polarization of the material responds at frequency 2ω. This polarization will radiate in phase and thus produce laser-like radiation at twice the drive frequency. This process and others like it are extremely useful for generating short wavelength radiation. However, just like in the case of the XUV lasers, the transparency of the material limits the efficient generation of short-wavelength radiation in nonlinear crystals to wavelengths above ~ 150 nm. To generate wavelengths shorter than 150 nm, gases must be used as the nonlinear medium. In gases, the conversion is significantly

less efficient [50] so while cascaded frequency conversion is possible with nonlinear crystals, it results in prohibitively low conversion in gases. Therefore it is difficult to use perturbative nonlinear optics to generate radiation much below ≈100 nm.

If the electric field incident on a dielectric is increased in amplitude until it is of comparable magnitude to the electric field binding the electrons to the nucleus $(\approx \frac{e}{a_0^2})$, then clearly a perturbative approach is no longer appropriate and the series in equation 1.17 fails to converge. Therefore, different physical descriptions are required to explain the observations of ultra-intense radiation with matter. For our purposes, the most salient phenomena that has come out of these studies is high-harmonic generation (HHG) [51–56]. In this process, radiation illuminating a gas is of such a high amplitude that the atomic potential is severely distorted such that an electron can tunnel out through the potential barrier, ionizing the atom. As the free electron oscillates in the electric field of the incident radiation gaining pondermotive energy, it can interact with the parent ion and generate radiation at harmonics of the fundamental. The great utility of this process is that many high-order harmonics are emitted with comparable efficiency up to some cutoff of harmonic energy. This is to be contrasted with perturbative interactions where higher order process fall off as $\sim I^{-q}$, where q is the harmonic order and I is the fundamental intensity. Therefore HHG provides a convenient technique for generating radiation throughout the XUV spectral region and into the soft X-ray [57].

1.2.1   Atomic response

There are many descriptions of the single-atom response in HHG which vary in their degree of rigor [53–56]. However, it is interesting to note that the characteristic features of HHG are well described by a semi-classical approach. For the work presented here, an in-depth, quantum mechanical treatment is unnecessary so we will focus on some aspects of a simple model, first introduced by Corkum [54]. In this ground breaking work, the ionization of the electron from the parent ion is calculated with tunnel ionization rates but

the interaction of the free electron in the incident electric field is treated classically. After ionization, the free electron is at the position of the parent ion with zero velocity. At this time it begins to accelerate in the direction of force from the incident field, completely free from any influence of the ion. As the oscillating incident field reverses direction, the electron will accelerate back towards the parent ion. There is a finite probability that the free electron will return to the position of the parent ion and radiatively recombine emitting a photon. This photon will possess all the kinetic energy gained in the interaction with the driving field plus the ionization energy of the atom.

The first step in this process is ionization of the target gas. The ionization rate is an important factor in determining the overall efficiency of the HHG process. When an atom is exposed to an intense oscillating electromagnetic field, there are a few different mechanisms that can produce ionization. These different processes are labeled multiphoton, tunneling, and over-the-barrier. In multiphoton ionization, the process proceeds by the absorption of several photons. The efficiency of this process will increase as the frequency of the driving field is increased since fewer photons are required to bridge the energy gap between the ground state and the continuum. In tunnel ionization, the field is larger and the atomic potential is distorted so much that the electron can tunnel through the potential energy barrier. If the field is increased even further, the atomic potential can be distorted to the point where the electron does not need to tunnel through a potential; the barrier to ionization has been completely removed. This is known as over-the-barrier ionization. The Keldysh parameter is used to estimate which process will be dominant at a given incident intensity and is given by

$$\gamma = \sqrt{\frac{U_I}{2U_p}}, \tag{1.18}$$

where U_I is the ionization threshold of the atom and U_p is the pondermotive energy. The ponderomotive energy is the average kinetic energy of a free electron in an oscillating elec-

tromagnetic field and is given by

$$U_p = \frac{e^2 E_0^2}{4\omega^2 m_e}.$$ (1.19)

Therefore, it is easy to see that the Keldysh parameter is proportional to the frequency of the driving laser and inversely proportional to the electric field strength. For a $\gamma \gg 1$ multiphoton ionization is dominant. For $\gamma \approx 1$ tunneling ionization is dominant and the frequency of the drive field is low enough as compared with the tunneling ionization rate that the adiabatic approximation can be used. In this limit, several authors have calculated tunnel ionization rates [58, 59]. The regime where $\gamma \ll 1$ corresponds to over-the-barrier ionization. Usually HHG is conducted in a regime where the Keldysh parameter is near one so that the ionization rates are fairly well approximated by the tunnel ionization models.

In the Corkum model, much can be learned by simply considering the classical electron trajectory. The classical electron trajectories in a linearly polarized electric field after ionization are given by

$$x = x_{0x} + v_{0x} - x_0 \cos \omega t,$$ (1.20)

$$v = v_{0x} + v_0 \sin \omega t,$$ (1.21)

where $x_0 = \frac{qE_0}{m_e\omega^2}$, $v_0 = x_0\omega$. The parameters v_{0x} and x_{0x} are chosen to ensure that the assumptions of zero position and velocity at the time of ionization are fulfilled. Solving for these parameters, given a tunneling time t_t, gives

$$x = x_0(\cos \omega t_t - \cos \omega t + \sin \omega t(\omega t_t - \omega t))$$ (1.22)

$$v = \omega x_0(\sin \omega t - \sin \omega t_t)$$ (1.23)

Some example electron trajectories from these equations at a few values of t_t are shown in Figure 1.3. As can be seen from the figure, there is different qualitative behavior of the electrons depending on the tunneling time. For some trajectories, the electron never returns to the position of the parent ion and no photon is emitted since recombination is impossible. For other trajectories, the electron returns to the ion after significantly less than one optical
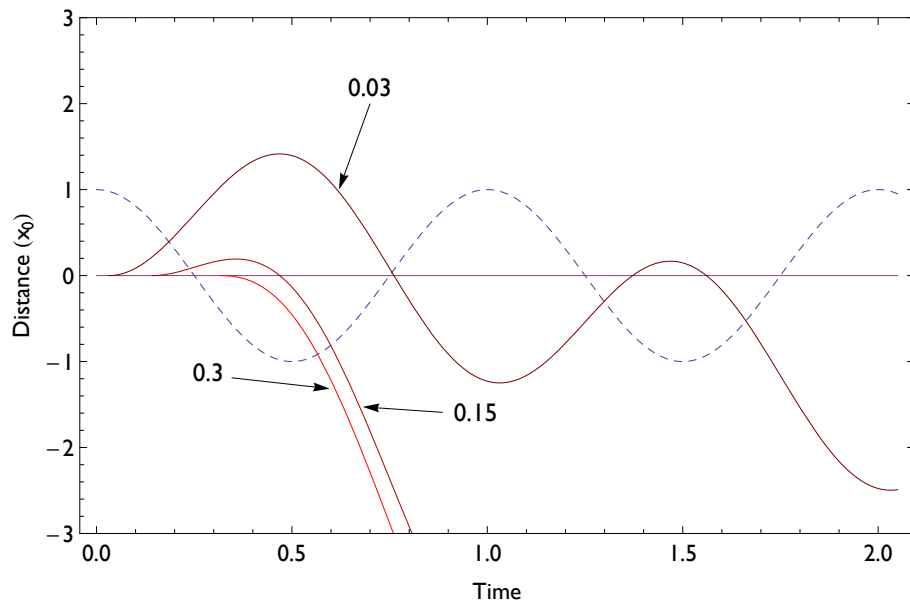
Figure 1.3: Plot showing the various categories of electron trajectories that occur for a given tunneling time and driving field. The driving field is shown by the dashed blue line and the electron trajectories are in shades of red. The different trajectories are labeled by their tunneling times, t_t of 0.03, 0.15, and 0.3. As can be seen from the figure, $\omega = 2\pi$ for these plots.

cycle– these are known as the "short" trajectories. The final class of electron trajectories are known as "long" trajectories and recombine with the parent ion after close to one full optical cycle later. For these trajectories, it is even possible that the electron combines after several optical cycles as the electron continues to oscillate about the position of the ion (as can be seen from the figure). However, the electron wavepacket will spread in space as it oscillates so that the probability of recombination after several optical cycles is small and the process is dominated by recombination in less than one cycle.
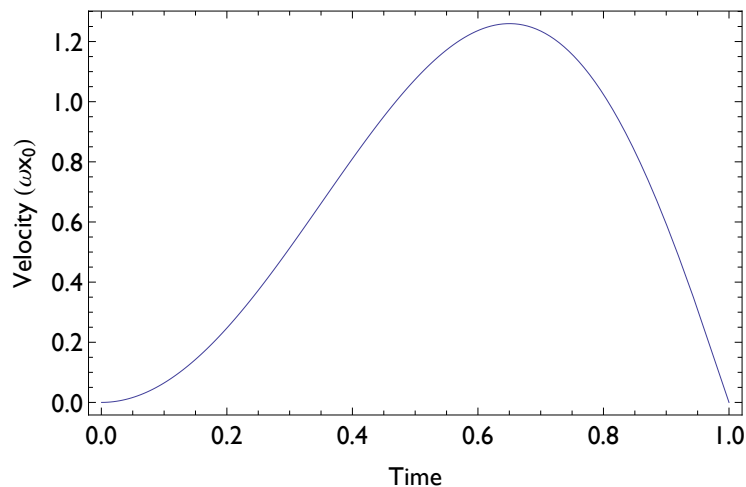
Figure 1.4: Velocity at the time of recombination plotted as a function of time away from the parent ion (the difference in recombination time and tunneling time). The time axis is in units of optical cycles so the plot includes very short tunneling times until exactly one optical cycle later.

It is instructive to plot the return velocity as a function of time away from the parent ion and this is shown in Figure 1.4. The figure shows that there are two separate paths (which can be labeled by their time away from the parent ion) which have the same velocity when returning to the parent ion. Since the photon energy is simply given by the kinetic energy of the electron plus the ionization energy, this results in two distinct processes which produce the same harmonic-photon energy (i.e. the long and short trajectories). Another interesting feature is that there is a well defined maximum return velocity given by $1.26\ \omega x_0$.

The pondermotive potential can be written as $\frac{m_e(\omega x_0)^2}{4}$ so that the maximum photon energy that can be generated from these trajectories is given by

$$\hbar\omega_{max} = U_I + 3.2\ U_p. \tag{1.24}$$

Note that exactly at the maximum energy, the short and long trajectories are no longer distinct and there is only one process that produces the harmonic photon.

Amazingly, this very simple classical picture agrees quite well with the experimental results. The maximum energy of harmonic emission is known as the cutoff and is well produced in both experiment and more detailed models by equation 1.24. Further, the existance of two processes for the emission of a specific harmonic photon energy can produce interference effects and a unique beam profile that have been measured experimentally and which will be discussed in greater detail in Chapter 4.

1.2.2   Phase matching

Up to this point, we have only considered the single atom response in the HHG process. However, high harmonics are typically generated in a gas target with a focused laser beam so macroscopic effects play a significant role in the efficiency of the process. Most notable of these effects is phase matching. It is imperative that harmonics generated at the front of the gas target be in phase with harmonics generated at the back of the target. Otherwise destructive interference can occur and harmonic power will drop dramatically. The phase of the fundamental light as it propagates through a focus can be written as

$$\phi_1 = [1 + \Delta n_p(\omega_1) + \Delta n_g(\omega_1)]kz - \tan^{-1}\left(\frac{z}{z_{R1}}\right). \tag{1.25}$$

Here Δn_p and Δn_g are the variations of the index of refraction due to the laser generated plasma and the neutral target gas respectively. The Rayleigh range of the fundamental is given by z_{R1} and the last term is the Gouy phase which is the phase shift when a beam passes through a focus. To arrive at the phase mismatch between the fundamental and harmonic

beam we have to additionally calculate the phase as a function of position for the harmonic beam.

$$\phi_q = [1 + \Delta n_p(\omega_q) + \Delta n_g(\omega_q)]kz - \tan^{-1}\left(\frac{z}{z_{Rq}}\right) + \frac{|\alpha_q|I_0}{1 + (z/z_{R1})^2}. \tag{1.26}$$

Here we have to include an additional term because the phase of the harmonic radiation linearly depends on the intensity that it was generated at [60]. The coefficient that describes this linear variation is given by α_q and must be multiplied by the intensity of the gaussian beam as it propagates. This coefficient is different for the two trajectories and roughly one order of magnitude larger for the long trajectories ($\alpha_q \sim 10^{-14}$ cm^2/W for the short trajectories and $\alpha_q \sim 10^{-13}$ cm^2/W for the long trajectories). Therefore, in general, phase matching calculation must be completed for the two trajectories separately. The Gouy phase of the harmonic beam depends on the harmonic beam Rayleigh range (z_{Rq}) which is usually larger but of the same order-of-magnitude as the fundamental Rayleigh range. To achieve phase matching we want to keep the phase mismatch constant over the generating medium. This phase mismatch is given by

$$\delta\phi = q\phi_1 - \phi_q \tag{1.27}$$

Since the phase of the fundamental must be multiplied by the harmonic order number, the phase shifts of the fundamental will usually dominate over the harmonic phase shifts. One exception to this is the intensity dependent phase.

We can therefore often simplify the phase mismatch to

$$\delta\phi \approx (\Delta n_p(\omega_1) + \Delta n_g(\omega_1))qkz - q\tan^{-1}\left(\frac{z}{z_{R1}}\right) - \frac{|\alpha_q|I_0}{1 + (z/z_{R1})^2}. \tag{1.28}$$

Our goal is to minimize the variations in this function over the generating medium. The plasma and neutral gas dispersion have opposite signs and can often be made to cancel each other at a certain plasma density ($\sim 10\%$ ionization [61]). The contribution of the Gouy phase shift is an odd function with respect to the focus while the intensity dependent phase is an even function so the variation of the two contributions can be made to cancel over a small region before the focus for the long trajectories. For the short trajectories,

the α_q parameter is too small to cancel the rapid variation of the phase mismatch from the fundamental Gouy phase shift (unless the harmonics are generated in a field approaching $\sim 5 \times 10^{14}$ W/cm^2). For this reason, it is challenging to cancel the variation in phase from the Gouy phase shift over a medium length on the order of z_{R1} and a better strategy is to keep the medium length roughly one order-of-magnitude shorter than z_{R1} for efficient phase matching. In high-repetition rate HHG experiments, the individual pulse energy is usually small so to achieve a high intensity, the focus and therefore z_{R1} should be made small.

1.2.3 Form of the harmonic spectrum

Here we show that by conducting HHG with a high repetition rate frequency comb, we obtain many harmonic orders each of which possesses underlying frequency comb structure. This is not meant to be a rigorous derivation but is mostly meant to offer intuition. For a more rigorous analysis see [62].

First we consider the form of the short bursts of harmonic radiation present in the HHG process in the time domain. The classical electron trajectory picture reproduces much of the relevent physics of HHG. However, a more realistic picture is to consider the electron wavepacket. In every half-cycle of the electric field, a portion of the electron wavepacket tunnels through the barrier and propagates in the potential given by the combination of the ionic potential and the external electric field. When the field reverses a small portion of the electron probability amplitude will return to the ion and interfere with the probability amplitude back in the ground state. From this, short bursts of high frequency radiation, often only hundreds of attoseconds long, will result every half cycle of the driving electric field.

Using the formalism used in the frequency comb section we can write the IR pulse as

$$E(t) = A(t)e^{i\omega_c t} \tag{1.29}$$

Here the envelope function of the pulse is given by $A(t)$. This functional form does not
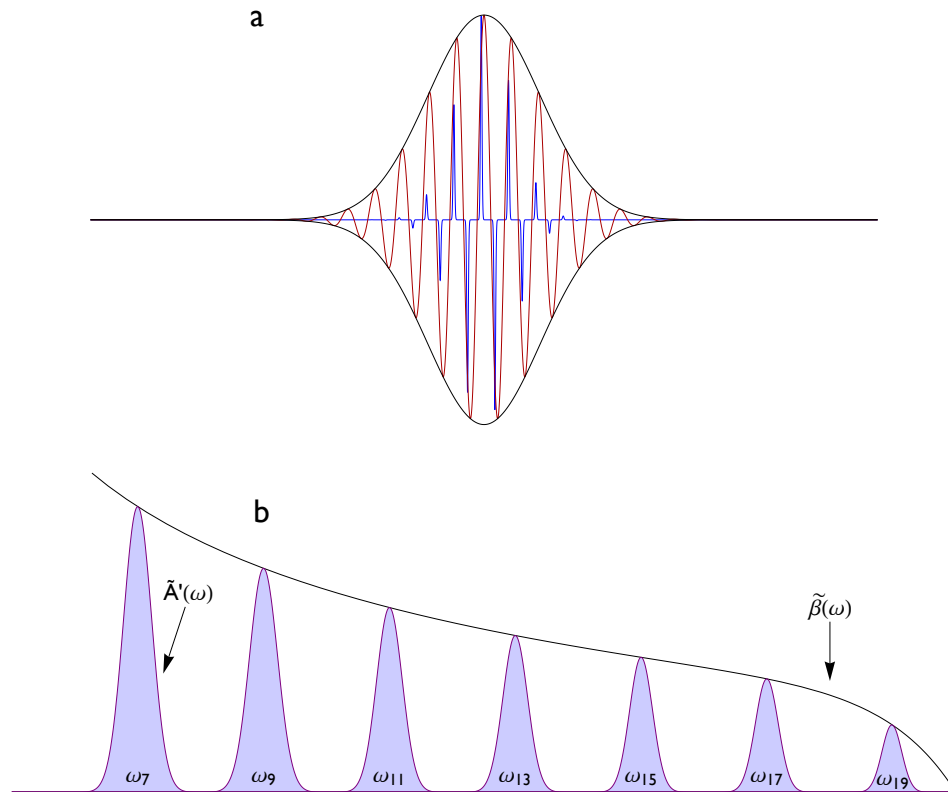
Figure 1.5: a) Depiction of a single IR pulse (red curve) and the underlying attosecond pulse train generated in the HHG process (blue curve). Since we are assuming a symmetric media, the attosecond bursts must repeat every half-cycle of the fundamental with every other burst receiving an overall π phase shift. b) The resulting harmonic spectrum.

matter for what follows but can be visualized as a Gaussian function. Now, consider the form of the short bursts of HHG radiation which is produced from an intense IR pulse and represented in Figure 1.5 in the time domain. We can also write down an approximate form of this radiation as follows.

$$E_{hh}(t) = A'(t) \times [(\mathrm{comb}(t, t_c) - \mathrm{comb}(t - t_c/2, t_c)) * \beta(t)]. \tag{1.30}$$

Here $A'(t) * \mathrm{comb}(t, t_c)$ is the envelope function of the high harmonic pulse train and $A'(t)$ will, in general, be different from $A(t)$. The underlying high harmonic pulse train is given by

$$(\mathrm{comb}(t, t_c) - \mathrm{comb}(t - t_c/2, t_c)) * \beta(t). \tag{1.31}$$

We assume that the high harmonics are generated in a symmetric media. In the second half cycle of the driving field, the media must respond exactly as it did in the first half cycle only π out of phase. This feature is therefore reproduced in equation 1.30 by the shifted and π out of phase comb functions. The shape of an individual harmonic burst is given by $\beta(t)$ where again the functional form is not critical for our discussion. It is well known that the attosecond bursts have a certain timing with respect to the driving field and this delay can also be taken into the form of $\beta(t)$. There is an assumption made in the form of equation 1.30 that the shape of the harmonic burst, $\beta(t)$, is independent of the driving field intensity. This is clearly an approximation but should be reasonable for a sufficiently long fundamental pulse. Given the form of equation 1.30, we can take the Fourier transform easily by following the frequency comb section.

$$\tilde{E}_{hh}(\omega) = \tilde{A}'(\omega) * [\mathrm{comb}(\omega - \omega_c, 2\omega_c)\tilde{\beta}(\omega)], \tag{1.32}$$

$$\Rightarrow \tilde{E}_{hh}(\omega) = \tilde{\beta}(\omega)[\tilde{A}'(\omega - \omega_c) + \tilde{A}'(\omega - 3\omega_c) + \tilde{A}'(\omega - 5\omega_c) + \tilde{A}'(\omega - 7\omega_c) +]. \tag{1.33}$$

From this we see that we get a series of odd harmonics of the carrier frequency. The overall power distribution between harmonic orders is determined by $\tilde{\beta}(\omega)$ and the individual shape of harmonic orders are given by $\tilde{A}'(\omega - q\omega_c)$.
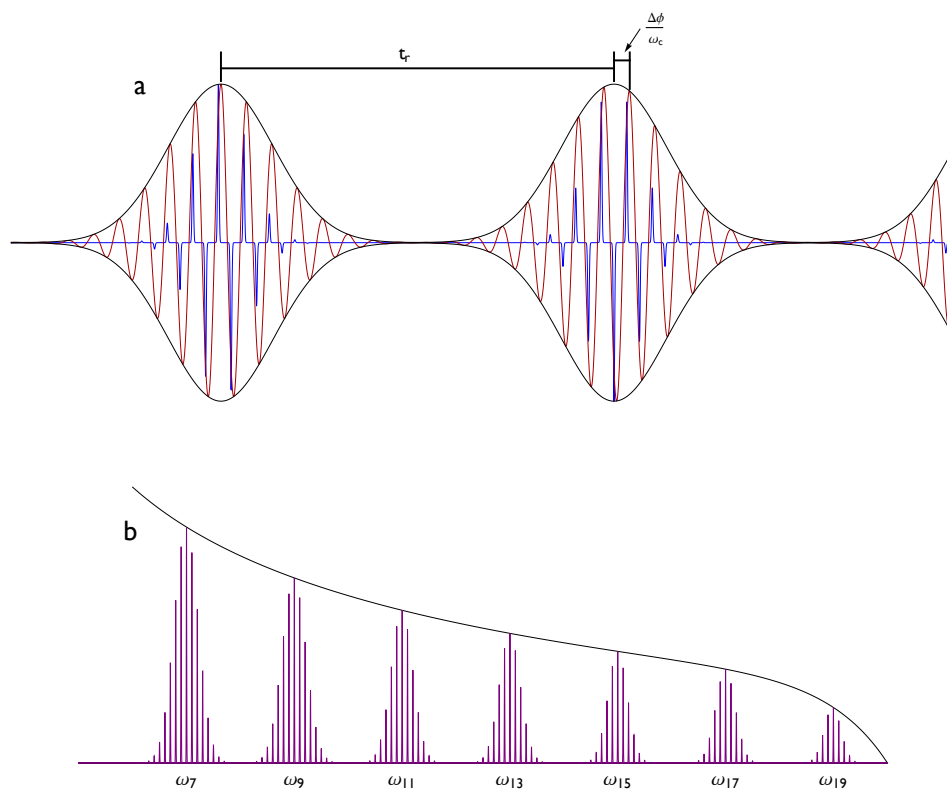
Figure 1.6: a) Depiction of the IR pulse train and the subsequent harmonic field. b) Depiction of the resulting harmonic spectrum with frequency comb structure underlying each harmonic order.

We now consider the form of this high frequency pulse train which is produced from an intense IR pulse train (instead of from an isolated IR pulse) and represented in figure 1.6a.

$$E(t) = A(t) * \text{comb}(t, t_r) e^{i\omega_c t}. \tag{1.34}$$

From a straightforward extension of equation 1.30 we get the following form for the high harmonic field.

$$E_{hh}(t) = [A'(t) * \text{comb}(t, t_r)] \times [(\text{comb}(t, t_c) - \text{comb}(t - t_c/2, t_c)) * \beta(t)]. \tag{1.35}$$

Once again, we can take the Fourier transform easily by following the frequency comb section.

$$\tilde{E}_{hh}(\omega) = [\tilde{A}'(\omega) \, \text{comb}(\omega, \omega_r)] * [\text{comb}(\omega - \omega_c, 2\omega_c)\tilde{\beta}(\omega)], \tag{1.36}$$

$$\Rightarrow \tilde{E}_{hh}(\omega) = \tilde{\beta}(\omega) \sum_{n=1}^{\infty} \tilde{A}'\left(\omega - (2n+1)\omega_c\right) \, \text{comb}\left(\omega - (2n+1)\omega_c, \omega_r\right), \tag{1.37}$$

$$\Rightarrow \tilde{E}_{hh}(\omega) = \tilde{\beta}(\omega)[\tilde{A}'(\omega - \omega_c) \, \text{comb}(\omega - \omega_o, \omega_r) + \tilde{A}'(\omega - 3\omega_c) \, \text{comb}(\omega - 3\omega_o, \omega_r) + \tag{1.38}$$

$$\tilde{A}'(\omega - 5\omega_c) \, \text{comb}(\omega - 5\omega_o, \omega_r) + \tilde{A}'(\omega - 7\omega_c) \, \text{comb}(\omega - 7\omega_o, \omega_r) + ...]$$

In the last step we again introduce $\omega_0 = \text{Remainder}(\frac{\omega_c}{\omega_r})$ which allows us to use the relation $\text{comb}(\omega - q\omega_c, \omega_r) = \text{comb}(\omega - q\omega_0, \omega_r)$. From this we see that we get a series of frequency combs at odd harmonics of the carrier frequency which is depicted in figure 1.6. Each frequency comb has an offset frequency of $q\omega_o$ where q corresponds to the harmonic order number. While we have not kept track of the exact the form of $\tilde{A}'(\omega)$, we know that the scale will be on the order of $\sim$100 THz in angular frequency units. Similarly for $\tilde{\beta}(\omega)$ we know that variations will occur on the scale of $\sim$10 PHz. Therefore we can understand $\tilde{A}'(\omega)$ as describing the shape of an individual harmonic frequency comb whereas $\tilde{\beta}(\omega)$ describes the relative amount of power present in the different harmonic orders.

From this result, we see that through the high harmonic process we do not simply generate a single XUV frequency comb. Instead we generate an array of frequency combs centered at odd harmonics of the driving carrier frequency. This provides a very versatile

source since there are many regions of spectral coverage which can be exploited. However, as discussed above, the average power requirements necessary to drive the HHG process at a high repetition rate are a major technical barrier. In Chapter 2, we discuss the femtosecond enhancement cavity which provides an elegant solution.

1.3 Noise in the HHG frequency comb

A further criterion for the generation of an XUV frequency comb is that the individual comb teeth must have linewidths below f_r. If this is not the case, then the individual comb teeth will blur into each other and we will have effectively created a broadband source– no more useful for precision frequency metrology than a low repetition rate HHG system. Ultimately, the comb linewidth is determined by the phase noise of the XUV comb, which is the result of the amplitude and phase noise present on the fundamental frequency comb. The way the noise is converted from the infrared comb to the XUV comb is therefore an important study that will ultimately determine the efficacy of our technique for ultrahigh resolution XUV spectroscopy. The phase noise of a narrow linewidth radiation source generated through perturbative harmonic generation is well understood; the phase noise of the fundamental will be multiplied by the harmonic order number, which is usually not catastrophic. However, perturbative nonlinear optics seems to be a very gentle process compared with high harmonic generation. In the case of HHG an electron is ripped off of an atom and violently thrown back to the parent ion and this process is sensitive to both the phase and amplitude noise of the driving laser pulse. Therefore, there is good reason for us to investigate the coherence of this process before attempting an ambitious physical measurement requiring a highly coherent source.

In a laser, phase noise can arise both from external perturbation and from quantum noise sources (for instance amplified spontaneous emission). Because of the quantum noise sources, even in the limit of no external noise processes, the laser still has a finite linewidth. It is reasonable to assume that the quantum noise sources in the HHG process itself are

small (one possibility could be plasma recombination, but this is not collimated radiation and is estimated to be small). Therefore we are more concerned with how perturbations in the driving field or atomic target are converted to phase noise in the harmonic comb. So in effect, what we are asking is how noise which is already present in the fundamental frequency comb is manifested in the harmonic frequency comb.

In conversion from an IR field to an XUV field through high harmonic generation, we can categorize these effects into phase-noise to phase-noise conversion processes (PPC), amplitude-noise to amplitude-noise conversion processes (AAC) and finally amplitude-noise to phase-noise conversion processes (APC). In principle, there could also be phase to amplitude noise conversion (PAC) but these processes should be small in the HHG process unless the fundamental pulse is very short (i.e. single cycle). PPC conversion processes are perhaps the easiest to understand and estimate. From our derivation of the harmonic frequency combs, we conclude that the phase noise of the harmonic frequency comb is the phase noise of the fundamental field multiplied by the harmonic order number. One way to see this is to consider the f_0 frequency in our fundamental field. Since earlier we found that the harmonic field offset frequency is the fundamental field offset frequency multiplied by its harmonic order number, we conclude that pulse-to-pulse phase variations are also multiplied by the harmonic order number in the HHG process. This picture is also reasonable since if our fundamental field has a Lorentzian comb linewidth $\Delta\nu$, the harmonic field will have a lorentzian comb linewidth given by $n\Delta\nu$ so that the relative linewidth $\frac{\Delta\nu}{\nu}$ is preserved in the harmonic process. While this picture seems reasonable, it should be stressed that it is still the subject of further experimental investigation.

AAC noise processes are also quite easy to understand but not trivial to calculate. In a perturbative harmonic generation process, the time-dependent amplitude of the generated field (averaged over the carrier frequency) is proportional to the amplitude of the fundamental field raised to the harmonic order number. For the high harmonic process, the harmonic dipole is roughly proportional to the ionization rate [63]. This ionization rate does not

follow a single power law but the its variation is significantly less rapid than $I_0(t)^n$ for plateau harmonics and is sometimes approximated as $I_0(t)^5$ [64]. In addition, the harmonic flux can saturate at high enough intensities due to depletion of neutral atoms along with the decrease in phase matching from the increased plasma density. So in total, the AAC noise processes should actually be suppressed as compared with perturbative nonlinear optical processes.

The most complex noise conversion mechanism in the HHG process comes from APC noise processes. This is because there are several separate effects that can contribute and because a good understanding of the strong-field processes in high-harmonic generation are required. These effects arise from two distinct contributions– plasma dispersion and the intensity-dependent dipole phase in high harmonic generation.

First we will consider the plasma related effects that contribute to amplitude-to-phase noise conversion. If the amplitude of our intracavity field varies, it is clear that the plasma density at the focus of our cavity will also vary. Since the plasma has a non-unity index of refraction, this will create a phase modulation. The index of refraction of a plasma is given by

$$n_p = \sqrt{1 - \frac{\omega_p^2}{\omega^2}} \tag{1.39}$$

where ω_p is the plasma frequency given by

$$\omega_p = \sqrt{\frac{Ne^2}{\epsilon_0 m_e}} \tag{1.40}$$

Where N is the electron number density, e is the electron charge and m_e is the electron mass. For our system, we estimate that the free electron density can approach 10^{17} cm^{-3} and therefore $\omega_p \leq 2 \times 10^{13}$ rad/s. It is clear that the resulting phase shifts will be much more severe for the fundamental intracavity field than for the harmonic field because of the longer wavelength. For harmonic fields below 150 nm, the resulting phase shift will be a maximum of ∼5 mrad, assuming that the plasma density is being modulated by 100%. For the fundamental field, the resulting phase shift will be a maximum of ∼40 mrad. These are

worst case scenarios and we can expect that the actual phase modulation will be far less. In our system we observe around 4% RMS intensity fluctuations at modulation frequencies below ~ 100 kHz. This would translate into only 20% plasma density fluctuations even if the plasma is not saturated. These effects by themselves therefore do not seem so detrimental.

In addition to plasma effects, there is also the intensity-dependent dipole phase [65] already discussed due to its relevance to phase matching. Its contribution to the phase of the harmonic field can be written as

$$\Delta\phi_d = \alpha_q I. \tag{1.41}$$

In our simplistic, semiclassical approach to harmonic generation, there are two distinct α_q parameters, which we understand as arising from the long and short trajectories. A full simulation of the time dependent Schrödinger equation shows that this view is too simplistic. The intensity dependent phase factors are not so distinct and are better represented by a distribution of α_q parameters, known as quantum paths. Still the view of distinct trajectories is sufficient for most of our discussion. The intensity dependent phase in high harmonic generation is distinct because there is no analogous process in perturbative harmonic generation. The magnitude of the α_q parameter is about $\frac{0.2\pi U_p}{\hbar\omega I}$ for the short trajectories. This works out to about 2×10^{-14} cm^2/W for the short trajectories. The long trajectories have an α_q parameter which is about an order of magnitude larger. Considering that the intensity to generate high harmonics is around 10^{13} W/cm^2, the phase variation from large amplitude fluctuation can now approach several radians for the long trajectories. Therefore, these effects are much more significant than the direct phase modulation of the harmonic radiation from the variations in plasma density. However, with a carefully designed system maintaining a low-level of amplitude noise, this effect would also not drastically broaden the combtooth linewidth unless the modulation process is happening at very high Fourier frequency.

From the estimates here, it is reasonable to believe that the frequency comb struc-

ture in the XUV through the harmonic generation process can be maintained. A more in depth discussion of the noise processes and experimental verification of the frequency comb coherence in both the VUV and XUV spectral regions is presented in Chapters 4 and 6.

Chapter 2

Principles of optical enhancement cavities

To achieve the high peak power, and thus corresponding high average power necessary to drive the high harmonic process at a repetition frequency of $\sim$100 MHz, we utilize an enhancement cavity. An enhancement cavity is a Fabry-Perot interferometer built with the specific intention of boosting the intensity within the optical cavity to drive some nonlinear process. This technique has been used since the 1960's to increase the conversion efficiency for second harmonic generation [66, 67]. Here, we use the enhancement cavity to enable HHG with a high repetition rate pulsed source [68]. To increase the power of a pulsed laser within an enhancement cavity is more challenging than with a cw laser because of the introduction of some new design constraints that will be discussed later in this chapter. In this section, we begin by deriving the intracavity field inside an enhancement cavity being excited by a continuous wave (cw) laser. Later, we generalize the result to excitation by a pulsed source (i.e. a frequency comb).

2.1   The cw enhancement cavity

Consider an optical cavity in a ring configuration with a narrow linewidth laser beam incident on one of the mirrors (called the input coupler) as shown in figure 2.1. We want to find the properties of the field within the optical cavity in steady state. The most straightforward way to proceed would be to match boundary conditions at the the reflective surfaces of the mirrors. However, the derivation proceeds very easily and intuitively if we instead
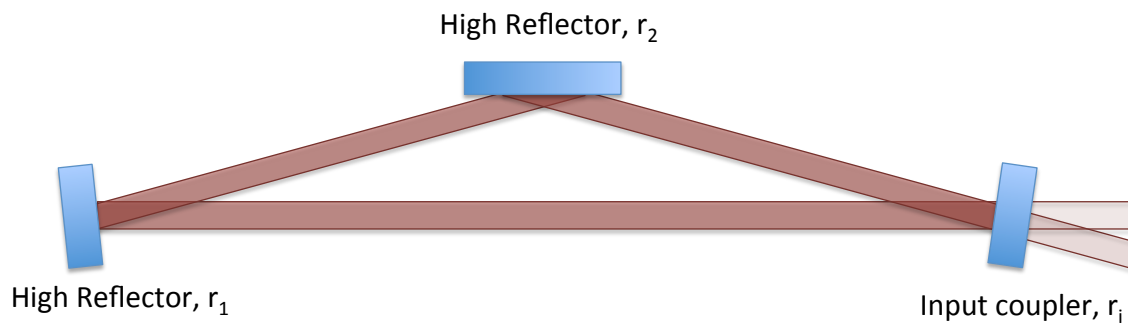
Figure 2.1: Diagram of a ring enhancement cavity for reference. In the diagram and the associated discussion, we ignore the transverse mode profile which is discussed later. A ring enhancement cavity is often more convenient than a linear enhancement cavities because it offers easy access to the beam reflected from the cavity. Also if the enhancement cavity is utilized for harmonic generation purposes, the harmonic light conveniently propagates in only one direction.

consider the addition of the electric fields from subsequent round trips within the cavity. For the first round trip, the field to the left of the input coupler in Figure 2.1 will be given simply by the field transmission coefficient t_i times the incident field. To find the true intracavity field, we must then add the components of the electric field which have entered the cavity at an earlier time and bounced around the cavity some number times. If we consider only the field which has just entered into the cavity along with the field which has bounced off of the other cavity mirrors and then back off of the input coupler a single time, then the field after the input coupler is given by $t_i + t_i r_n r_i e^{i\phi}$. Here the coefficient r_n is the effective field reflectivity of the other mirrors in the cavity. For instance, if there are two other cavity mirrors then $r_n = r_1 r_2$. The phase in this expression, ϕ, is the total phase shift that the field experiences while propagating once through the cavity. Now adding to this the field which has entered the cavity at all previous times, the field directly after the input coupler is given by

$$E_{cav} = E_0 t_i (1 + r_n r_i e^{i\phi} + (r_n r_i e^{i\phi})^2 + (r_n r_i e^{i\phi})^3 +). \tag{2.1}$$

The reflectivity coefficients are all less than 1 (coefficients greater than 1 would imply gain) so that equation 2.1 is a convergent geometric series which can be written as,

$$E_{cav} = \frac{E_0 t_i}{(1 - r_n r_i e^{i\phi})}. \tag{2.2}$$

This easily derivable equation is a good starting point to ascertain many of the physical properties of an enhancement cavity. The quantity ϕ takes into account both propagation phase shifts and phase shifts due to dispersive intracavity elements (mirrors, gas, transmissive optical elements etc.). Written out explicitly, $\phi = \frac{n\omega L}{c} + \phi_d(\omega)$ where ω is the carrier frequency, n is the index of refraction within the cavity (assumed to be a homogenous medium), L is the cavity length and $\phi_d(\omega)$ is the phase shift from the dispersive cavity elements. For simplicity we assume that n has no frequency dependence and therefore the dispersion in the index of refraction is taken up in $\phi_d(\omega)$. Note that when using dielectric mirrors, there is significant dispersion even from the cavity mirrors themselves (dielectric

mirrors are used exclusively in the enhancement cavities discussed in this thesis due to their high reflectivity and high damage threshold).

The experimental parameters we are most accustomed to dealing with are the optical powers, and the corresponding reflectivites $(R = r^2)$ and transmissions $(T = t^2)$. By taking the absolute value squared of equation 2.2 and rewriting in terms of R and T we obtain

$$I_{cav} = \frac{T_i I_0}{1 + R_n R_i - 2\sqrt{R_n R_i} \cos \phi}. \tag{2.3}$$

This expression can be arranged into the following form,

$$\Rightarrow I_{cav} = \frac{T_i I_0}{(1 - \sqrt{R_n R_i})^2} \frac{1}{1 + \frac{4\sqrt{R_n R_i}}{(1 - \sqrt{R_n R_i})^2} \sin^2 (\phi/2)}. \tag{2.4}$$

We will now define the quantities $F = \frac{4\sqrt{R_n R_i}}{(1 - \sqrt{R_n R_i})^2}$ (called the coefficient of finesse) and $\beta_E = \frac{T_i}{(1 - \sqrt{R_n R_i})^2}$ so that equation 2.4 can be written as:

$$I_{cav} = \beta_E I_0 \frac{1}{1 + F \sin^2 (\phi/2)}. \tag{2.5}$$

This is a convenient separation as there is now a function which contains all the phase/frequency dependence and with unit amplitude and a prefactor (β_E) which contains the power enhancement on resonance.

The prefactor, β_E, can be simplified significantly if one considers a cavity composed of mirrors with high reflectivities. In this case it is convenient to write the prefactor just in terms of transmission coefficients since they are small quantities.

$$\beta_E = \frac{T_i}{(1 - \sqrt{(1 - T_n)(1 - T_i)})^2} \approx \frac{4T_i}{(T_n + T_i)^2} \tag{2.6}$$

In arriving at this equation, we have only considered that energy is being lost from the enhancement cavity through the transmission of the optics. Of course, there are many other physical effects that could also lead to loss (scattering or absorption). However, there is nothing that prevents us from including these loss mechanisms into the T_n coefficient. Therefore, we can understand equation 2.6 as

$$\beta_E \approx \frac{4T_i}{(\text{Loss})^2} \tag{2.7}$$

where the loss is the total round trip loss inside the cavity including all optical transmission, absorption and scattering. We can make the same form of simplifications for the coefficient of finesse and arrive at

$$F \approx \left(\frac{4}{\text{Loss}}\right)^2 \tag{2.8}$$

One point to make note of is that the coefficient of finesse depends only on the total loss in the cavity. It does not matter whether this loss comes from the input coupler or from somewhere else in the cavity. The buildup, on the other hand, distinguishes between loss through the input coupler transmission and loss from somewhere else since it also depends on T_i.

State-of-the-art mirrors can easily achieve $R = .9999$ which for an impedance-matched ($T_i = \frac{\text{Loss}}{2}$) three-mirror cavity leads to $\beta_E = 5000$. This clearly demonstrates the great utility of a resonantly driven enhancement cavity in achieving power enhancement. It is exactly this property that we use to enable high harmonic generation with a modelocked laser source that, by itself, produces field strengths that are far inadequate for this purpose.

2.2   The femtosecond enhancement cavity

The frequency dependent part of equation 2.5 is given by $\frac{1}{1+F\sin^2(\phi/2)}$, where $\phi = \frac{n\omega L}{c} + \phi_d(\omega)$. In this section we will ignore the contributions of $\phi_d(\omega)$ and consider this contribution specifically in the next section. With $\phi_d(\omega)$ set to zero, we notice that the function is periodic with ω and repeats whenever the $\frac{n\omega L}{c} = 2\pi q$ where q is an integer. The frequency interval over which the function repeats is called the free spectral range (FSR) and for this example is $\frac{2\pi c}{nL}$ in angular frequency units. The use of the name "free spectral range" is for historical reasons as some of the earliest uses of Fabry-Perot interferometers were as spectrometers and the FSR was the maximum spectral content that a radiation source could have before it would couple to two or more resonances simultaneously, complicating the interpretation of transmission data from the Fabry-Perot interferometer.

A useful quantity to characterize an enhancement cavity is the finesse $\mathcal{F}$,(as compared with the coefficient of finesse, F, that we have been using thus far) which is defined as the ratio of the FSR to the full width at half maximum linewidth. From equation 2.5 and the definition of the FSR, the intracavity buildup will drop to one-half of the peak value when $F \sin^2 \frac{\pi \Delta \omega}{2 \times FSR} = 1$. For a reasonably high finesse this condition is met when the argument of the sine function is small so that we can write the condition as $\Delta \omega \approx \frac{2 \times FSR}{\pi} \sqrt{\frac{1}{F}}$. Therefore the finesse is given by $\mathcal{F} = \frac{\pi}{2} \sqrt{F} = \frac{2\pi}{Loss}$. The finesse should be thought of as a way to characterize the quality of an enhancement cavity in much the same way as the quality factor or Q (defined as the resonance width divided by the center frequency) for an rf resonator. In the case of optical resonators, the finesse is a more useful quantity than the Q because the optical center frequency is so large and the resonance so narrow in many cases that the Q is an unwieldy, large number. Also, both the power buildup and finesse of an optical cavity are determined by the reflectivity of the cavity mirrors with no dependence on the cavity length unless there is a homogenous absorbing medium filling the optical cavity. If one increases the mirror spacing for a given optical cavity (increase L in the equations above) by a factor of two, the finesse and buildup will stay the same however the Q of the cavity will increase by a factor of two. Therefore, for an optical cavity, the finesse is usually a more useful measure of the quality of the optical elements. With the definition of the finesse and free spectral range we can rewrite equation 2.5 as

$$I_{cav} = \beta_E I_0 \frac{1}{1 + \left(\frac{2\mathcal{F}}{\pi} \sin \left(\frac{\pi \omega}{FSR} \right) \right)^2}. \tag{2.9}$$

From the occurence of periodic resonances in a Fabry-Perot resonator, it is easy to see that the enhancement cavity is very well suited to enhance the power of a frequency comb. While a frequency comb has many comb modes that must be enhanced simultaneously, the enhancement cavity also has periodic resonances. Therefore, in principle the whole frequency comb can be enhanced if every frequency comb mode is matched to its respective resonance. Clearly, to achieve this, the repetition rate of the frequency comb must be
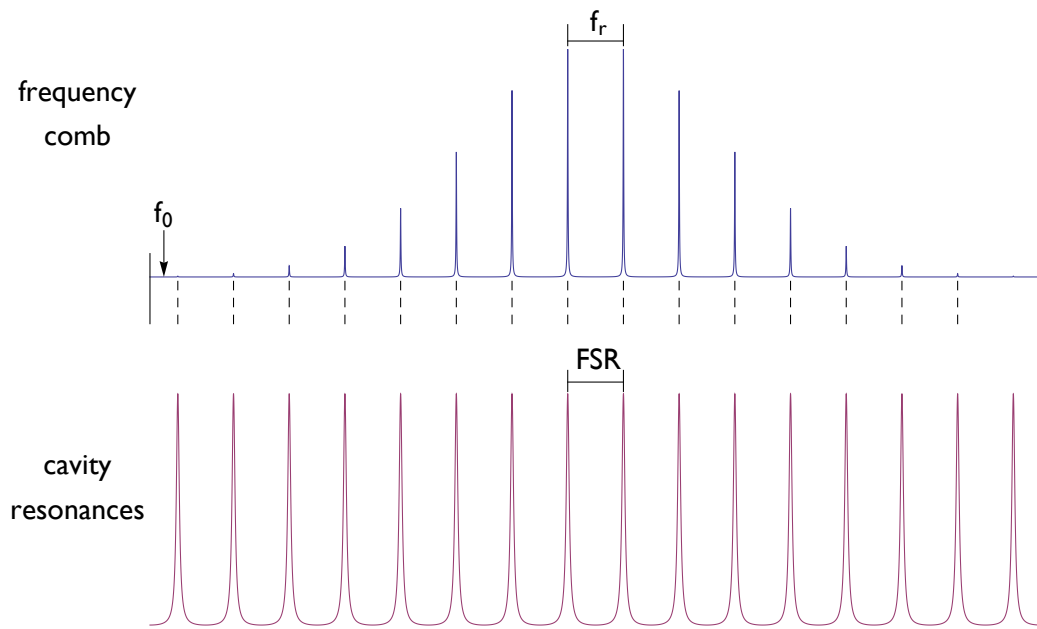
Figure 2.2: Diagram showing how by adjusting both the repetition and offset frequency of the frequency comb, one can simultaneously enhance every frequency comb mode by coupling each mode to an enhancement cavity resonance.

matched to the FSR of the enhancement cavity. When this condition is satisfied, the offset frequency can be adjusted until the resonance condition for all frequency components is satisfied simultaneously.

This process of satisfying the resonance condition can also be understood in the time domain and may be more intuitive. If we excite the cavity with a pulse train instead of by a cw laser, we can consider what occurs as the field is first building up. After the first pulse is incident on the cavity, a small pulse is transmitted by the input coupler and bounces once around the cavity. If we want to resonantly enforce the electric field of this pulse, we want to adjust the repetition rate of the laser so that when the intracavity pulse arrives back at the input coupler the next pulse in the pulse train is just arriving at the input coupler. This is equivalent to matching the FSR to the repetition rate of the laser. However, this is a necessary but not sufficient condition to achieving resonance because the field of the pulse also has an underlying phase. In general this underlying phase evolves in the pulse train of the excitation laser (due to the offset frequency) and in the pulse propagating back and forth in the cavity (due to dispersion which we will treat in the next section). Therefore, the phase evolution of the intracavity pulse after one round trip through the cavity must match the pulse-to-pulse phase evolution of the pulse train of the frequency comb exciting the cavity if we are to achieve constructive interference.

2.3   The effects of dispersion

Until now we have ignored the effects of intracavity dispersion by setting $\phi_d = 0$ in the previous section. The effect of this dispersion on an enhancement cavity will be to shift the position of the cavity resonances so that the FSR of a cavity is not a constant but will depend on the optical frequency. Since, for a modelocked laser, the spacing between comb modes is rigorously given by f_r, the conclusion at the end of the last section that we can resonantly enhance the whole frequency comb is only true over a given bandwidth for which the FSR is roughly constant. Therefore, the intracavity phase shifts will play a major role in

determining the design constraints of the enhancement cavity. Given a nonzero ϕ_d, we want to determine the cavity enhancement as a function of frequency. As a first step we Taylor expand the round trip phase shift of our cavity about some frequency ω_c' near but slightly different from our carrier frequency.

$$\phi_d = \phi_0 + \phi_1(\omega - \omega_c') + \phi_2(\omega - \omega_c')^2 + \phi_3(\omega - \omega_c')^3 \dots \tag{2.10}$$

The effects of these individual terms on a propagating pulse is shown in Figure 2.3. As can be seen in the figure, the effect of a constant phase shift ϕ_0 in the frequency domain is to to apply a phase shift to the underlying carrier of the pulse but to leave the pulse envelope unaffected. The effect of the first order term, ϕ_1, is to shift the envelope of the pulse, but the shape of the envelope and the underlying carrier are not affected. If we begin with a transform limited pulse, the higher order dispersion terms (ϕ_2 and higher) will cause the pulse envelope to broaden and distort.
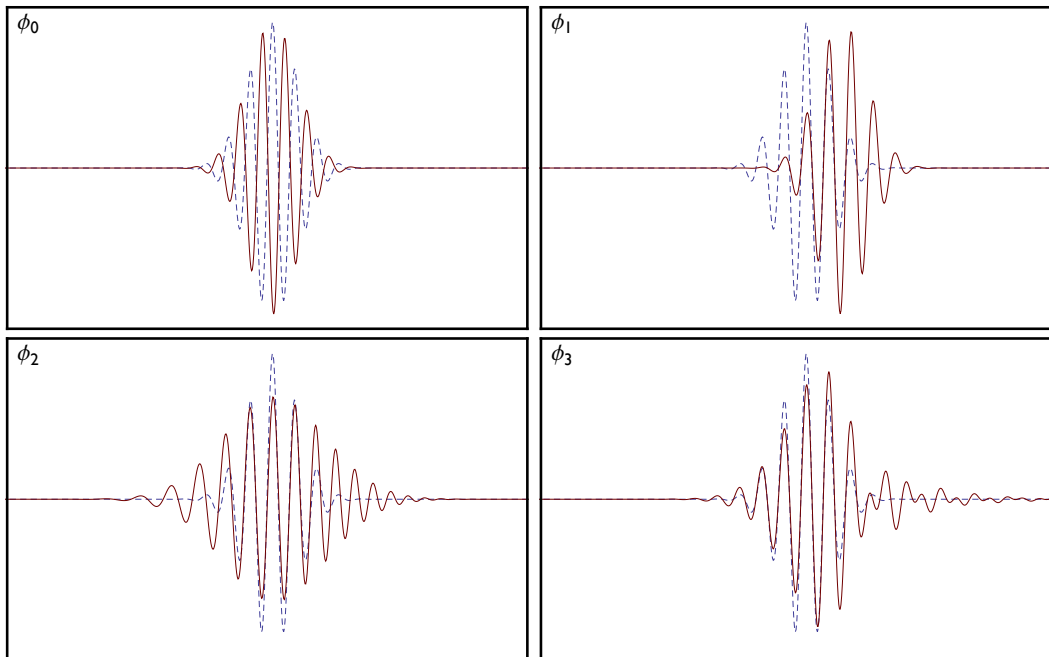
Figure 2.3: The effects of the individual dispersion terms defined in equation 2.10 on a short laser pulse

Consider a pulse propagating inside of an enhancement cavity that has a phase shift described by ϕ_0 with all other higher-order terms in equation 2.10 equal to zero. Every time the pulse returns to the input coupler, the phase underlying the pulse envelope will have shifted by some amount. To drive this pulse resonantly with our external frequency comb, we must make sure that subsequent pulses within the pulse train also possess this same phase evolution. This is accomplished by adjusting f_0 of the frequency comb.

The effects of a nonzero ϕ_1 is to cause the position of the pulse envelope to change while the shape of the pulse and the underlying carrier remains the same. This means that, in general, the position of the carrier with respect to the pulse envelope also changes. We can still excite the resonance of our enhancement cavity in this case by adjusting the repetition rate and offset frequency of the frequency comb according to $\Delta f_0 = \omega'_c \phi_1 f_r$ and $\Delta f_r = \phi_1 f_r^2$. Consequently, for a nonzero ϕ_0 and ϕ_1 the frequency comb parameters for maximum coupling about the expansion frequency, ω_c, is

$$f_0 = -(\phi_0 - \omega'_c \phi_1) f_r, \tag{2.11}$$

$$f_r = \frac{c}{nL}\left(1 + \phi_1 \frac{c}{nL}\right). \tag{2.12}$$

The effect of terms higher than ϕ_1 will cause distortions of the pulse envelope and underlying carrier as shown in Figure 2.3. There is no way to compensate for these effects completely by adjusting the repetition frequency and offset frequency and therefore the coherent addition of pulses within the cavity is impeded. The end result is that the intracavity pulse will be distorted with respect to the incident pulse and the pulse energy enhancement will be lower than what one might expect from a straightforward application of equation 2.6.

With a qualitative understanding of the effects of dispersion on our ability to couple a short pulse to an enhancement cavity, we can gain additional insight through equation 2.5. First of all, since we know that the effects of ϕ_0 and ϕ_1 can be eliminated by adjusting the
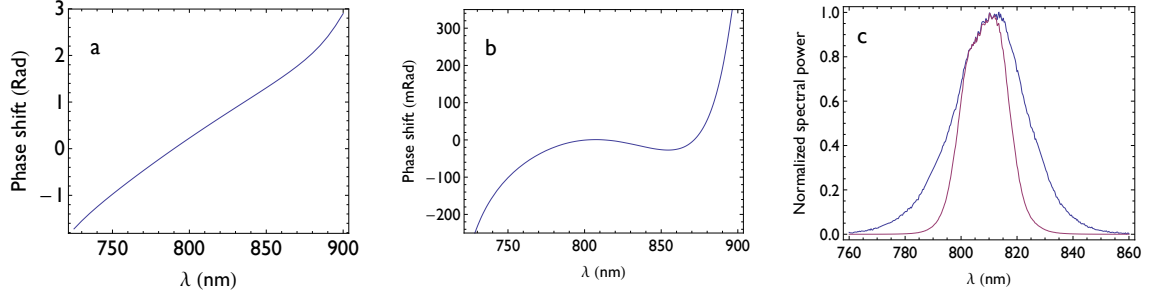
Figure 2.4: The effect of cavity mirror dispersion on the ability to couple a frequency comb to an enhancement cavity. a) Cavity phase shift curve calculated from the mirror phase shift curves provided by the manufacturer. b) The same as in a) only with the contributions from ϕ_0 and ϕ_1 subtracted given $\omega'_c \approx 810$ nm. c) The resulting filtered spectrum given a cavity finesse of about 1000 (red curve). For reference, the incident spectrum is also shown (blue curve)

degrees of freedom of our frequency comb, we will define a phase with these terms subtracted.

$$\phi'_d(\omega) = \phi - \phi_0 - \phi_1(\omega - \omega'_c) \tag{2.13}$$

We can understand the coupling of our comb to the periodic resonances by assuming that we have adjusted our frequency comb so that ϕ_0 and ϕ_1 are compensated and we obtain the following equation from equation 2.5.

$$I_{cav} = \beta_E I_0 \, \frac{1}{1 + F \sin^2\left(p\pi + \frac{\phi'_d(\omega)}{2}\right)} \tag{2.14}$$

Here p is an integer and labels the comb modes. In the case where $\phi'_d(\omega) = 0$, the intracavity buildup will be exactly that which would be obtained from a cw laser perfectly on resonance $(\beta_E I_0)$. If we include the effects of higher order dispersion (which for all cases considered in this thesis will be less than 2π) we will begin to attenuate portions of our spectrum away from ω'_c.

As an example, the spectral filtering that occurs because of intracavity dispersion is shown in Figure 2.4 using actual dielectric mirror phase shifts obtained from a manufaturer. These mirrors were used to build an enhancement cavity for Ti:Sapp modelocked laser system. The first panel shows a calculated intracavity round trip phase shift for the evacuated
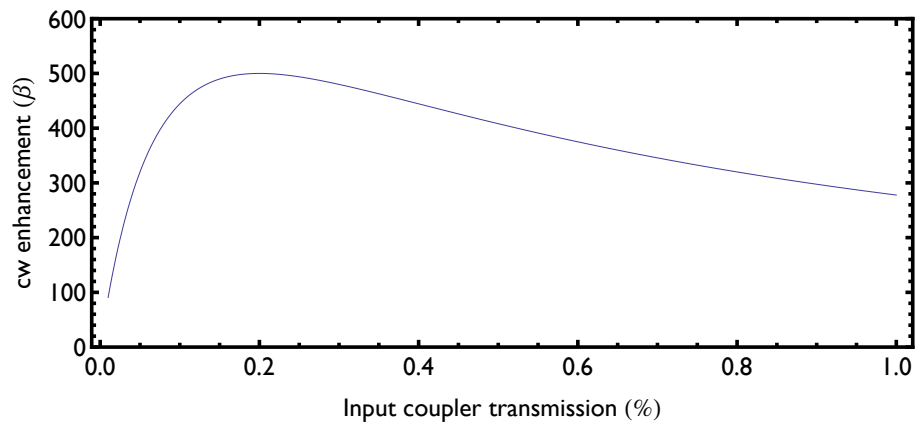
Figure 2.5: The enhancement of a cw Fabry-Perot cavity with 0.2 % cavity loss (excluding the input coupler transmission) as a function of input coupler transmission. This shows that the buildup is maximized when the input coupler transmission matches all other sources of loss which is known as an impedance matched cavity. However, as discussed in the text, the peak intracavity power is not necessarily maximized for an impedance matched femtosecond enhancement cavity. Note that the buildup decreases rather gradually as the input coupler transmission is increased for an overcoupled cavity (input coupler transmission larger than all other sources of loss).

optical cavity (so that n=1 and there is no residual gas dispersion) so that the dispersion is due entirely to the dielectric mirror phase shifts. The phase shift shown in Figure 2.4a has a large offset and linear component around 800 nm where we wish to couple in spectrum. However, as previously discussed, by adjusting the offset frequency and repetition rate of the frequency comb, we are able to eliminate these contributions leaving only the higher order terms. Figure 2.4b shows the resulting phase with ϕ_0 and ϕ_1 subtracted. Using an example spectrum from the Ti:Sapp frequency comb, we can estimate the degree of spectral filtering using the application of equation 2.14. This is shown in Figure 2.4c.

A somewhat counterintuitive effect is present in a femtosecond enhancement cavity as a direct result of this spectral filtering. If one were building an enhancement cavity for a cw laser with the goal of obtaining the highest peak power possible, it would be best to increase the reflectivities of the mirrors as much as possible while keeping the cavity impedance matched (transmission of the input coupler equal to all other sources of loss), raising both the finesse and the buildup. For a femtosecond enhancement cavity, as one increases the finesse, the spectral filtering becomes more severe. This spectral filtering will produce two effects. The first is that the average power in the cavity will be lower than what would be expected without the filtering. The second effect is that the pulse will be longer in the time domain. Both effects will serve to lower the peak power in the cavity and so, for a femtosecond enhancement cavity, one can sometimes obtain higher peak power with a lower finesse cavity depending on the dispersion of the mirror coatings.

It is then reasonable to ask if one should lower the finesse by lowering the transmission of the input coupler or by introducing loss somewhere else in the optical cavity. From inspecting equation 2.7, it can be deduced that one should increase the transmission of the input coupler to obtain a lower finesse while keeping the buildup as high as possible because the input coupler transmission appears in the numerator. From our treatment so far, this point seems trivial however it is often a point of confusion for someone more familiar with cw enhancement cavities. If we consider a cavity where the losses in the cavity (excluding

the input coupler transmission) are held constant, the best power enhancement is obtained when the intracavity losses are equal to the transmission of the input coupler (an impedance matched cavity) as shown in Figure 2.5. Therefore, the impression can arise that impedance matching is always best and therefore lowering the finesse should be done by introducing symmetric loss. However, in our case we are actually asking what is the best buildup that can be obtained for a given finesse. As can be seen from equation 2.7, for an impedance matched cavity the buildup is given by $\beta_E \approx \frac{\mathcal{F}}{\pi}$ whereas for a cavity where the loss is dominated at the input coupler $\beta_E \approx \frac{2\mathcal{F}}{\pi}$. Therefore to keep the cavity enhancement as high as possible, the transmission of the input coupler should be increased to lower the finesse and we should always strive for a cavity where the loss is dominated by the input coupler.

2.4   Transverse mode profile

The description thus far has focused on the methods we use to achieve a high peak power within the enhancement cavity. However, the atomic response in the high harmonic process depends on the intensity as opposed to the power (the intensity required is on the order of 10^{13} W/cm^2). We therefore also must design our cavity to have an intracavity focus to achieve this very high intensity. The basic cavity design is shown in figure 2.6. Target gas is usually injected at the location of the intracavity focus between the two curved mirrors.

As can be seen from figure 2.6, the curved mirrors are at an angle with the incident light. In addition to a small amount of spherical aberration, the angle on the curved mirrors produces a different focal length in the horizontal and vertical dimensions. This lack of cylindrical symmetry means that the transverse mode propagating within our enhancement cavity is well approximated by Hermite-Gaussian functions (instead of the Laguerre-Gaussian modes appropriate for cylindrically symmetric cavities). This means, in part, that it is necessary to determine the intracavity transverse mode profile for the horizontal and vertical dimensions separately. In our enhancement cavity, we only excite the TEM$_{00}$ intracavity mode so we will focus only on that component for what follows. The TEM$_{00}$ mode can be
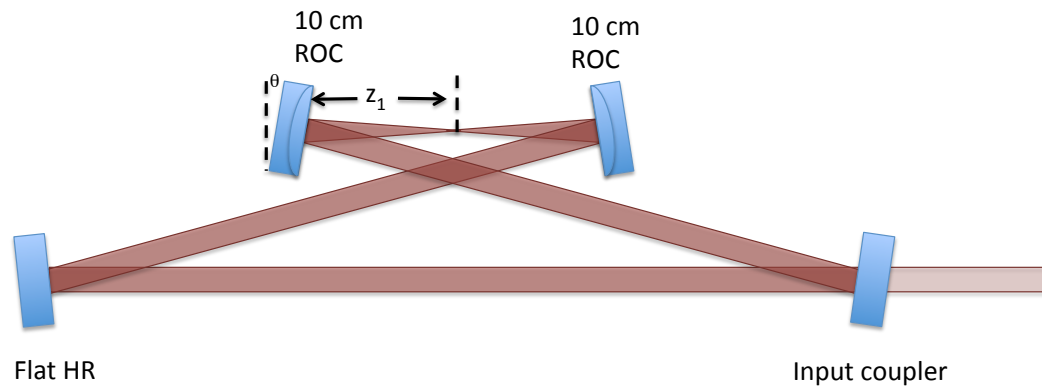
Figure 2.6: Diagram showing a typical cavity design with two curved mirrors to produce an intracavity focus. This intracavity focus is required to reach the very high intensities. In the figure, θ is the incident angle on the mirrors, and z_1 is half the distance between the curved mirrors. In the text, we also refer to z_2 which is the total propagation distance around the cavity minus the distance between the curved mirrors.

written as

$$u_{00}(x, y, z) = \frac{1}{\sqrt{q_x(z)q_y(z)}} \exp\left(-ik\left[\frac{x^2}{2q_x(z)} + \frac{y^2}{2q_y(z)}\right]\right). \tag{2.15}$$

With the Gaussian beam defined in this way the q parameter relates to the more commonly used experimental parameters of radius of curvature and spot size according to

$$\frac{1}{q} = \frac{1}{R'} - \frac{i\lambda}{\pi w^2}. \tag{2.16}$$

where R' is the beam radius of curvature and w is the beam spot size. It is well known that the complex q parameters (q_x and q_y) for Gaussian beams can be determined using the ABCD matrix formulation. We now briefly review the ABCD matrix formalism necessary for calculating the intracavity transverse mode for reference [69].

There is an ABCD matrix for all commonly encountered optical elements including propagation through free space. If one has a series of optical elements then the total matrix can be found by matrix multiplication of all the elements in order. If we define the total ABCD transfer matrix as

$$M_{tot} = \begin{pmatrix} A & B \\ C & D \end{pmatrix}, \tag{2.17}$$

then the q parameter at the exit is then found by

$$q_2 = \frac{Aq_1 + B}{Cq_1 + D}. \tag{2.18}$$

For our enhancement cavity, we will only encounter free space propagation, reflection off of flat surfaces (which is essentially an identity matrix) and reflection off of curved mirrors. For reference, the ABCD matrices for each of these elements is

$$\text{free space:} \quad M_{fs}(z) = \begin{pmatrix} 1 & z \\ 0 & 1 \end{pmatrix}, \tag{2.19}$$

$$\text{curved mirror horiz. (x):} \quad M_{mh}(R, \theta) = \begin{pmatrix} 1 & 0 \\ -2/[R\cos(\theta)] & 1 \end{pmatrix}, \tag{2.20}$$

$$\text{curved mirror vert. (y):} \quad M_{mv}(R,\theta) = \begin{pmatrix} 1 & 0 \\ -2\cos(\theta)/R & 1 \end{pmatrix}. \quad (2.21)$$

We can find the matrix which determines the beam profile after one round trip through the cavity if we know the matrices of every element through matrix multiplication. For instance, if we start at the focus then the total matrix for the horoizontal dimension is

$$M_{tot} = M_{fs}(z_1) \cdot M_{mh}(R,\theta) \cdot M_{fs}(z_2) \cdot M_{mh}(R,\theta) \cdot M_{fs}(z_1). \quad (2.22)$$

To find the transverse mode within the cavity, we want to look for the q parameter which will be indentical after every round trip through the cavity. This is equivalent to finding the eigenvalue of the matrix M_{tot}. Solving for the eigenvalue of the q parameter, the beam spotsize at the focus can be determined with equation 2.16 and is shown in figure 2.7. Here it can be seen that this cavity geometry allows spot sizes on the order of 10 μm. As compared with a millimeter sized beam, this is four orders of magnitude increase in intensity. The plot also shows how the beam becomes infinitesimally small when the distance between the curved mirrors reaches two extremes called the outer and inner stability edge. Outside these points the cavity is an unstable resonator (i.e. there is no eigenvalue for the cavity matrix).

It is often desirable to operate the enhancement cavity near a stability edge to increase the intensity at the focus. We have a choice in that case– we can either operate near the inner or the outer stability edge. From looking at figure 2.7 the two choices seem identical. However, in figure 2.8 we plot the beam spot size as it propagates throughout the long arm of the cavity near the inner and outer stability edges. From this plot, it is clear that for the outer stability edge, the beam has a more dramatic focus and smaller spot size at the midpoint. Since we have to bounce off of flat high reflectors in this portion of the cavity, the potential for intensity related damage to the optics becomes more severe when using the outer stability edge. For this reason we usually run our enhancement cavities near the inner stability edge.
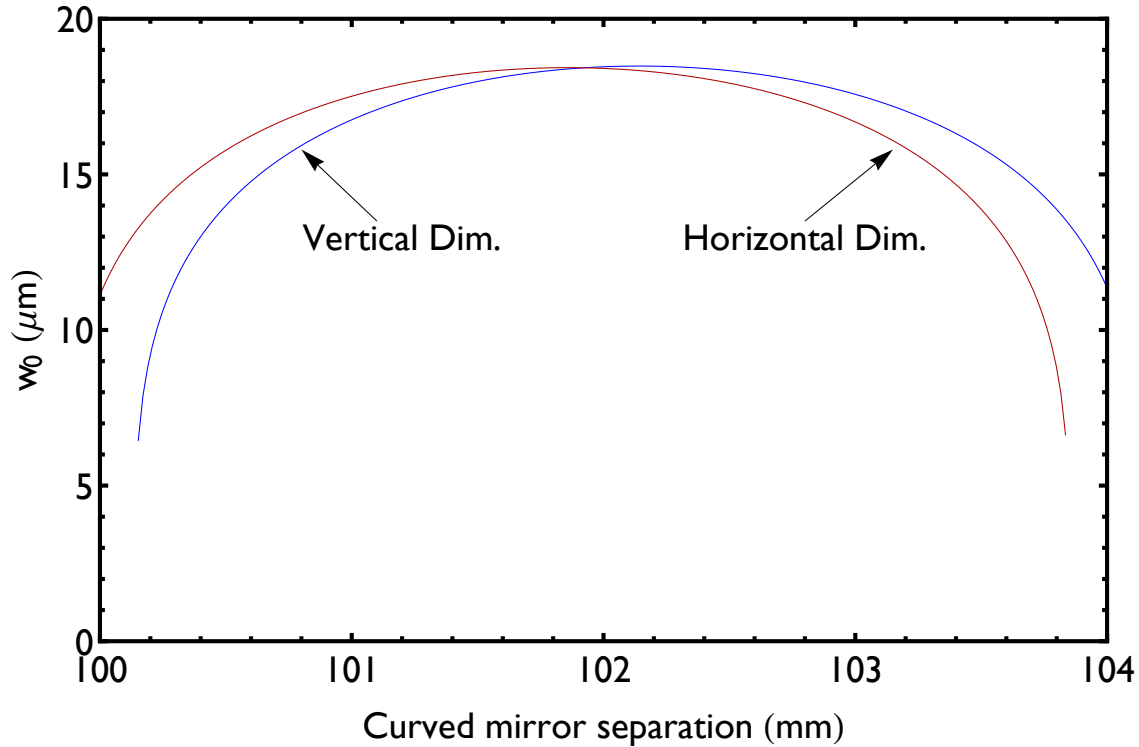
Figure 2.7: The spot size at the focus as a function of the distance between the two curved mirrors ($2z_1$). For this plot, the wavelength is 1070 nm, the radius of curvature of the two mirrors is 10 cm, the incident angle on the curved mirrors is 3° and z_2 is 2.6 m.
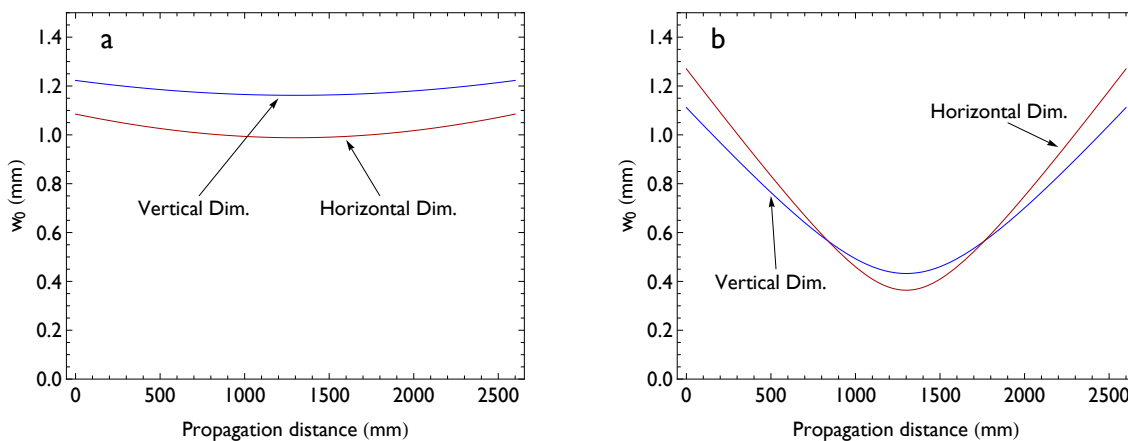
Figure 2.8: Plot showing the spotsize of the beam in the horizontal and vertical dimensions as it propagates through the long arm of the cavity (z_2) near the inner and outer stability edges. a) The inner stability edge with $2z_1 = 100.5$ mm. b) The outer stability edge with $2z_1 = 103.5$ mm.

Chapter 3

Experimental apparatus

In this chapter, the basic setup of the high-repetition rate HHG source is described. Some of the measurements made in this work were completed using a setup with small variants of what is described here. However, these variations are usually rather inconsequential and so what is described in this chapter gives a very good overview of our techniques.

3.1   The high power frequency comb

During the development of high repetition rate HHG sources in the Ye group, we have utilized both Ti:Sapp Kerr-lens modelocked lasers and Yb saturable-absorber modelocked fiber lasers as cavity excitation sources. Both lasers have their own advantages but eventually we chose to focus solely on the Yb fiber lasers. One of the main criteria that influenced our decision was that fiber lasers have a tremendous capability for robust, high average power operation. In principle, modern mirror coating technology can produce very high finesse cavities with power buildup exceeding 10,000 which could lead to the assumption that the average power of the excitation laser is not so critical. In practice, however, mirror dispersion, plasma phase shifts and mirror damage make high harmonic generation inside a very high finesse cavity impractical. In general, the lower the finesse of the enhancement cavity, the more robust the system will be. Therefore it is benefical to push the average power of the excitation laser as high as possible so that there is not a stringent requirement on the cavity finesse to reach large intracavity power.

The high power operation of fiber lasers is due, in large part, to the very efficient thermal management. The surface-area-to-volume ratio of an optical fiber is large, which allows for efficient radiative cooling. In addition, since the laser radiation is guided there are no problems with thermal lensing for reasonable fiber mode areas. In addition, the low quantum defect in Yb:glass based fiber lasers also leads to lower heat load on an amplifier. This also means that pump efficiencies in excess of 90% are possible and recently modelocked fiber lasers nearing 1 kW of average power have been reported [70].

Another difference in Yb fiber and Ti:Sapp lasers is the center wavelength. Yb fiber lasers produce spectrum centered near 1050 nm whereas Ti:Sapp operates near 800 nm. It has been discovered both theoretically and experimentally that the efficiency of the HHG process (considering only the single atom response and ignoring phase matching effects) is proportional to $\sim \lambda^{-5.5}$ [71, 72]. By moving to the longer wavelength we immediately suffer a decrease in efficiency by about a factor of 5 with all other things being equal. This feature of the HHG process has created interest in building enhancement cavities at 532 nm [73]. Moving to shorter wavelength has been met with difficulty however because the cracking of hydrocarbons becomes much more efficient at shorter wavelength which can produce mirror contamination within the enhancement cavity. In the end, we decided to sacrifice the efficiency of the harmonic process for the robust, high power nature of both the laser source and enhancement cavity. In the future, if one desires to push these systems to even shorter wavelength, the longer fundamental wavelength will facilitate a higher cutoff energy of harmonic radiation and will therefore be advantageous.

The laser system we use as a cavity excitation source is a modelocked Yb-fiber frequency comb built by our collaborators Axel Ruehl, Ingmar Hartl, and Martin Fermann at IMRA, America and fully described in [74]. This laser uses chirped pulse amplification to produce 80 W of average power with 120 fs pulse duration and 154 MHz repetition frequency. The chirped pulse amplifier uses a compression ratio of 3100 to ensure that the pulse undergoes linear amplification (i.e. spectral broadening and power dependent phase shifts are negligible)

which makes for a much more controllable system. While the system shown in [70] is higher powered than our system, control of the f_0 and f_r frequencies has not been demonstrated and therefore our system is currently the highest average power frequency comb. A diagram of the laser system is depicted in Figure 3.1 as a reference for the following discussion.

The laser oscillator is a Fabry-Perot type fiber laser, which is modelocked with a saturable absorber (center spectrum 1050 nm). The saturable absorber has a subpicosecond lifetime and is mounted in the free-space section of the oscillator on a fast, multi-layer piezoelectric transducer (PZT). With this transducer, fast control ($\approx$ 75 kHz bandwidth) of the oscillator length is available. The gain fiber is a highly doped phosphosilicate fiber pumped by a fiber coupled diode at 976 nm. Most of the fiber length is wrapped around a drum PZT whose radius expands and contracts depending on the applied voltage. This will stretch the gain fiber and produce roughly an order of magnitude larger repetition frequency tuning in comparison with the saturable absorber actuator and is used for large, slow adjustments of the repetition frequency.

The output coupler of the oscillator is a chirped fiber-Bragg grating [75] which has roughly 5% reflectivity at our center wavelength. This low reflectivity produces a very low finesse laser cavity which results in phase noise at high fourier frequencies. We will discuss techniques to mitigate this in Chapter 4. The fiber-Bragg grating is mounted on a Peltier junction to control its temperature. A change in temperature changes the dispersion of the fiber-Bragg grating. If we choose to parameterize the comb with the f_r and f_0 frequencies, then this temperature change will adjust the f_0 frequency predominantly. Since it is a temperature change, this is a rather slow feedback taking several seconds to settle after a step adjustment. A change in roughly 5 °C results in change in the offset frequency by a full repetition period (we commonly adjust the temperature within 20-30 °C).

The oscillator output is about 100 mW and is stretched to 870 ps in a fiber stretcher with a total length of > 380 m. The dispersion of the stretcher is precisely tuned to compensate for the dispersion of other fibers in the system and the final grating compressor.
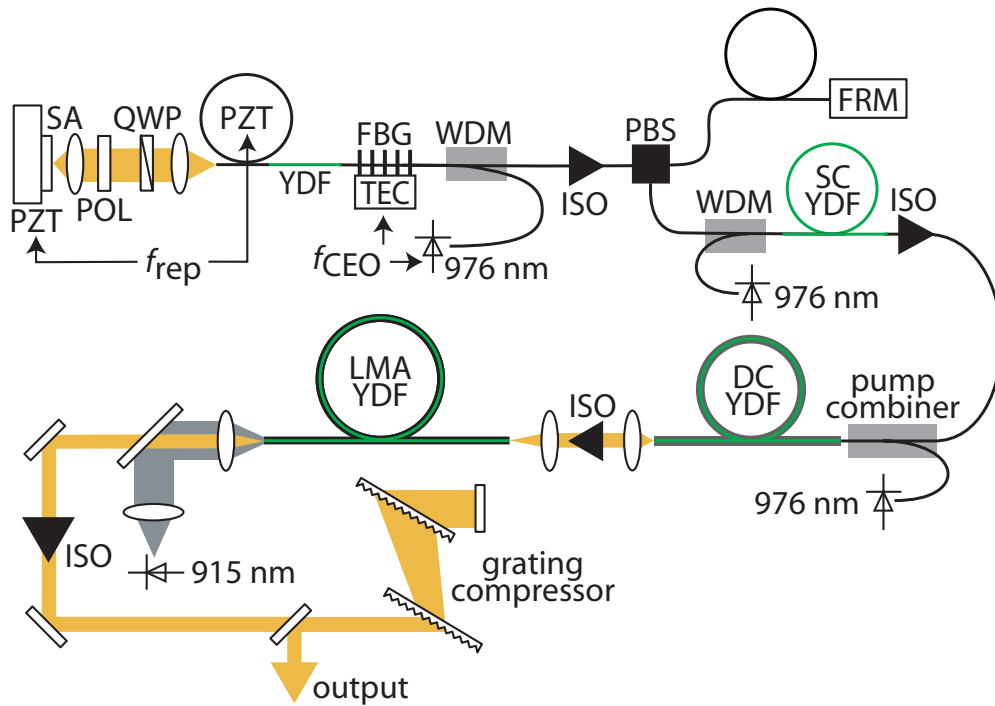
Figure 3.1: High power Yb fiber fiber frequency comb. The acronyms in the figure are given by: PZT, piezo actuator; SA, saturable absorber; POL, polarizer; QWP, quarter-wave plate; YDF, Yb-doped fiber; FBG, fiber Bragg grating; TEC, thermoelectric cooler; WDM, wavelength division multiplexer; ISO, optical isolator; PBS, polarizing beam splitter; FRM, Faraday rotator mirror; SC, single-clad: DC, double-clad; and LMA, large mode area.

The losses in the fiber stretcher are relatively large and a 10-m single-clad Yb amplifier fiber pumped with 0.6 W of 976 nm radiation is required to replace the power lost in the stretcher. This is connected to an 8-m polarization-maintaining cladding-pumped Yb fiber thatg is pumped with 10 W at 976 nm, which brings the net power up to 3.4 W. This light is then free-space coupled into a 9 m, large mode area fiber (700 μm^2) which is pumped by fiber coupled 915 nm diode bars. The choice to pump the amplifiers and oscillators with 976 nm or 915 nm comes from the form of the two absorption bands in Yb fiber systems. The band at 976 nm is more narrow and has a lower quantum defect whereas the band at 915 nm is broader and therefore there is less constraint on the pump linewidth. Before compression the output of the laser is 108 W. Compression is achieved with a pair of polymer transmission gratings with 1590 lines/mm in the Littrow confiiguration. The beam is magnified to roughly 1 cm in diameter before being sent through the compressor to decrease the peak intensity on the polymer gratings. A compressor efficiency of 72% was obtained, which is why the maximum compressed power is 80 W instead of the full 108 W. The pulse duration after compression is 120 fs. At the output, the spectrum is centered at 1070 nm with roughly 20 nm of bandwidth.
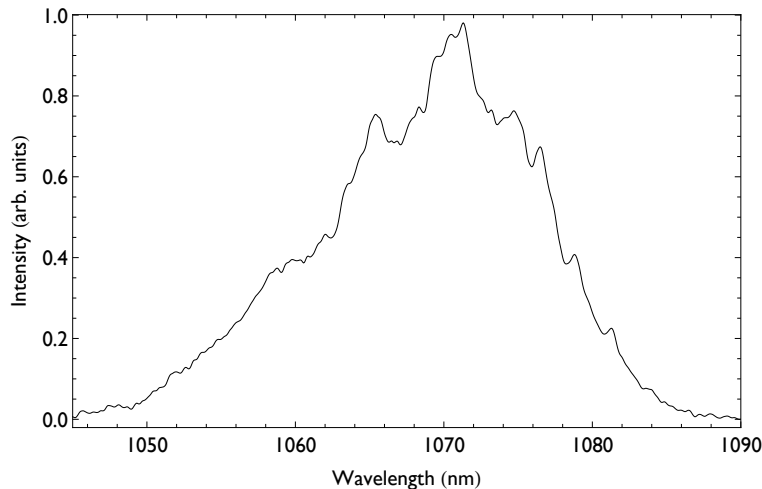
Figure 3.2: The normalized spectral output of the power amplifier. The relatively narrow bandwidth of 20 nm is well suited to enhancement cavity applications.

3.2   The enhancement cavity

Before sending the beam to the enhancement cavity, it is reduced in diameter by a factor of two in a Galilean telescope (combination of one positive and one negative lens). Since, we usually operate the cavity on the inner stability edge as described in Chapter 2, only a very gentle focus is required for optimal mode matching. This can be accomplished by a slight adjustment of one lens in the demagnification telescope. Due to thermal lensing in our system, the negative lens is placed on a translation stage and adjusted to compensate as the amplifier power is increased.

There is also a relatively small but noticeable power-dependent misalignement of the beam before the cavity. To correct for this, the misalignement is measured by detecting the position of the beam near the enhancement cavity with a quadrant photodiode (looking at the small transmission through a high reflecting mirror). A steering mirror near the power amplifier is placed on a piezoelectric actuated mirror mount that is then actively adjusted to compensate.

The whole enhancement cavity is within a large vacuum chamber evacuated with a 300 l/s turbo pump. Operating the experiment in vacuum is necessary since at atmospheric pressure, the harmonic light is absorbed. The optical mounts inside the chamber are placed on a copper breadboard that rests on cut Viton O-rings set directly on the vacuum chamber. The vacuum chamber itself sits on rubber flask stoppers, one-inch thick. The combination of two layers of rubber and the copper breadboard were chosen to minimize external laboratory perturbations coupling to the enhancement cavity.

The enhancement cavity is built in a bowtie ring configuration. The ring configuration is more desirable than a linear cavity because the radiation reflected from the cavity can be monitored easily without polarization optics. This is convenient as we have to generate an error signal from the reflected light to lock the frequency comb to the cavity. Also, the harmonic radiation generated from the traveling wave that is present in a ring configuration
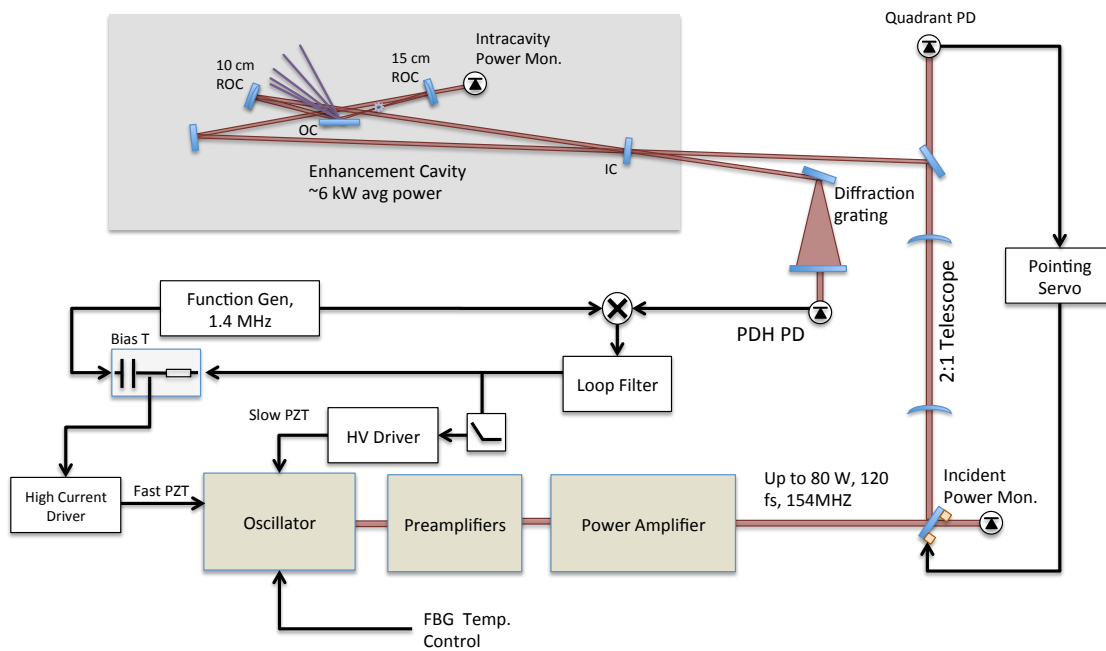
Figure 3.3: Enhancement cavity setup. The acronyms in the figure are given by: PZT, piezo actuator; FBG, fiber Bragg grating; HV, high voltage; PDH, Pound Drever Hall. Much of this figure shows the electronics necessary for the PDH cavity lock. Also shown is the beam pointing servo and intracavity and incident power moniters. The harmonic output coupler will be discussed later in the chapter.

will propagate in only one direction. The free spectral range is chosen to match the repetition rate of the laser and therefore the cavity is 1.95 meters long in total.

The mirror coatings are highly reflective (99.99%), high damage threshold dielectric stacks. We have used a variety of different input couplers with different transmissions but we have found the best results are obtained with a 1.5% transmission input coupler (our choice of input couplers is discussed more in Chapter 5). As discussed previously, since the input coupler transmission is the dominant loss in the enhancement cavity, the buildup is given by $\frac{2\mathcal{F}}{\pi}$. Therefore the finesse is ~ 400 and the highest buildup obtainable is ~ 250. This optimum buildup can be degraded by imperfect transverse mode matching. Some imperfection is, in fact, guaranteed because the resonant beam in the cavity is slightly elliptical as a result of the bowtie geometry and the slight incident angle on the intracavity curved mirrors that we do not compensate. In practice, we usually record a buildup of ~ 200 with the alignment optimized. In principle, spectral filtering can also cause a decrease in buildup but in our case the finesse of the cavity is low, the bandwidth of the laser is only 20 nm and we have eliminated transmission optics from the cavity so the residual dispersion is due only to mirror dispersion. Given these factors we can easily couple our entire laser spectrum into the cavity with minimal spectral filtering.

The intracavity focus is formed with two curved mirrors with a radius-of-curvature (ROC) of 10 cm and 15 cm (although we often also use a symmetric cavity with two 10 cm ROC mirrors). The choice of mirror curvatures is important since, on the one hand, it is important to keep the focus small to achieve a significant ionization rate. At the same time, to achieve proper phase matching, it is important to keep the Rayleigh range as long as possible. The use of an assymmetric cavity is helpful because the harmonic output coupler, which we will discuss in later in the chapter, must be placed between the curved mirrors. In this region, the area of the beam is rapidly increasing as one moves away from the focus. Therefore, by placing the output coupler on the 15 cm ROC mirror side of the focus, it is possible to place the optic further away from the focus and reduce the peak intensity on the

mirror that decreases the risk of damage to that optic.

3.3   Comb-cavity stabilization

Here we discuss the implementation of a feedback loop which keeps the laser on resonance with the cavity. As discussed in Chapter 1, to resonantly enhance the entire frequency comb it is necessary to control two degrees of freedom of the comb. However, it was also discussed in Chapter 1 that parameterizing the comb into f_r and f_0 is not always advantageous. This is, in part, because physical noise processes often do not affect these parameters in an orthogonal way. Also, since we are interested in the precise positions of the frequency comb modes in the optical domain about a fairly narrow spectral region (only 20 nm of bandwidth), control of f_r and f_0 produces a nearly degenerate effect. For this reason it is better to parameterize the motion of the comb into a translation motion (whereby the comb modes shift together and the spacing between comb modes does not change) and a fixed-point motion whereby the spacing between comb modes changes with one point near the center of the spectrum held fixed. We will refer to the first motion as a translation mode and the latter as the central breathing mode. It is interesting to note that in this parameterization, changes in the laser cavity length produce mainly changes in the translation mode.

As it turns out, for our laser system almost all of the laser noise which must be canceled in the feedback loop arises from variations in translation mode with very little noise arising from the central breathing mode. This makes sense if one considers that our bandwidth is very narrow. Different noise processes will have their own fixed point motion and as long as this fixed point does not lie close to the center frequency of the comb, these noise processes will all appear to produce essentially translation mode noise. For this reason, to couple the entire frequency comb into the enhancement cavity, it is only necessary to control the translation mode of the laser actively to first bring a few comb modes onto resonance with the cavity near the center of the laser spectrum. Then, the central breathing mode of the frequency comb can be adjusted slowly by hand until the entire frequency comb is on

resonance.

To actively control the translation mode frequency, we have to generate an error signal that can be used in a feedback loop. There are two common methods for achieving this which are called the Hänsch-Couillard (or polarization cavity lock) [76] and the Pound-Drever-Hall (or PDH cavity lock) [5] . These two methods are similar in many ways. The Hansch-Couillard relies on comparing the phase of two different polarizations reflected from the cavity whereas the PDH lock places sidebands on the carrier and then compares the phase of the carrier with the phase of sidebands upon reflection from the cavity. A feature of the PDH lock is that the capture range is determined by the modulation frequency. This can be contrasted with the Hansch-Couillard lock where the capture range is determined by the the cavity linewidth. If the modulation frequency can be increased significantly past the cavity linewidth, the PDH cavity lock will be much more robust against large environmental perturbations which would otherwise cause the lock to break.

For this reason, we implement a PDH lock for our enhancement cavity. The normal method to place high frequency side bands on the laser is to use an electro-optic modulator (EOM). However, the generally low damage threshold of EOMs makes this method not desireable for our experiment. In principle we could place the EOM before the power amplifier but this is not possible in our setup for lack of sufficient space. Instead, we modulate the fast length control actuator in the laser oscillator to produce sidebands. There is a major challenge in that the broadband frequency response of that actuator begins to roll-off at about 70 kHz which is very low for PDH sidebands (consider that the resonance width of our cavity is ~400 kHz). However, individual mechanical resonances can be found in the saturable absorber actuator which are much higher in frequency. Therefore we commonly place sidebands on our laser at 1.4 MHz by utilizing a resonance of the saturable absorber transducer.

Since we have a frequency comb and not a cw laser, we are actually placing symmetric sidebands on each individual mode of the comb. Upon reflection from the cavity, different

parts of the spectrum will in general produce different PDH error signals depending on that spectral regions resonance conditions. We therefore disperse our reflected light off of a diffraction grating before detecting the beatnote on a photodiode. We demodulate this signal with our 1.4 MHz modulation frequency using a double balanced mixer to produce the PDH error signal. Since the dispersion of this diffraction grating is certainly not high enough to resolve single comb teeth, one should think of the resulting error signal as being due to the coherent addition of error signals from neighboring comb teeth within a certain spectral region. Using this error signal, we apply negative feedback onto the fast length transducer in the laser oscillator. This will keep that portion of spectrum that is being detected locked to the resonance of the enhancement cavity.

The feedback loop utilizes cascaded integrators and a proportional stage with the crossover frequency to proportional gain at 100 kHz. The zero placed in the transfer function at 100 kHz frequency is chosen to roughly correspond to the rolloff of our fast piezoelectric transducer. The fast actuator can only make adjustments to the length of the enhancement cavity by about 1 μm. Low frequency mechanical perturbations and temperature drifts will cause this actuator to run out of range in a few seconds. We therefore integrate the low frequency drift of this actuator and feed back onto the intracavity fiber stretcher. In this way the fast actuator will always be centered around its nominal zero position and will only be forced to correct the fast frequency changes. If the laboratory is reasonably stable in temperature, the combination of slow and fast actuators won't run out of range for hours.

To keep all modes of the frequency comb on resonance with the cavity, it is important to adjust both degrees of freedom of the frequency comb. To adjust the central breathing motion of the frequency comb we adjust the temperature of the fiber-Bragg grating maximizing the intracavity power to couple in the full frequency comb. The transmission through one mirror of the enhancement cavity is monitored for this purpose and also to obtain an accurate measure of the intracavity buildup. Of course, a change in the temperature of the fiber Bragg grating will not operate only on the central breathing mode of the comb. However, as

we adjust the temperature, our active feedback on the translation mode will automatically compensate for any residual changes in translation mode that occur from the temperature change of the fiber-Bragg grating.

On resonance we are able to couple our entire spectrum into the cavity without significant spectral filtering effects. With a buildup of $\sim$200 we can commonly achieve 5-8 kW of average intracavity power. This corresponds to the excitation laser being run somewhat derated at about 25 W to 30 W. By focusing to ~ 1000 μm^2 we achieve peak intensities well above 10^{13} W/cm^2, which is sufficient for high harmonic generation.

3.4   Injection of xenon gas

At the intracavity focus, we inject a target gas of xenon atoms with a ≈ 100 μm diameter glass nozzle. As discussed in Chapter 1, this small diameter is necessary for optimum phase matching since the gas target interaction region should be about one order of magnitude less than the Rayleigh range (which for our cavity is about 1 mm). We place a backing pressure of one to several atmospheres of pressure on the nozzle (in Chapter 5 the optimum pressure is discussed in more detail). The position of the nozzle is adjusted precisely with the aid of a motorized 3-D translation stage. It is extremely challenging to align this very small nozzle accurately at the beam focus. Since the nozzle provides an effusive gas flow it is necessary to place the tip of the nozzle within roughly one nozzle diameter of the beam or else there will be an appreciable decrease in gas density. In addition, if the gas is allowed to expand, the target size will increase which will result in decreased efficiency from the geometric phase matching factors. Therefore when the nozzle is positioned correctly for maximum harmonic buildup, it is also very close to an extremely intense beam and it is common to melt the glass tip of the nozzle shut, in which case it has to be replaced or polished open.

With our single 300 l/s turbo, the gas load from the gas target can cause the background xenon gas pressure to rise to several militorr. This is undesirable both because it could limit the mechanical lifetime of the turbo pump and also because the high level of gas within the
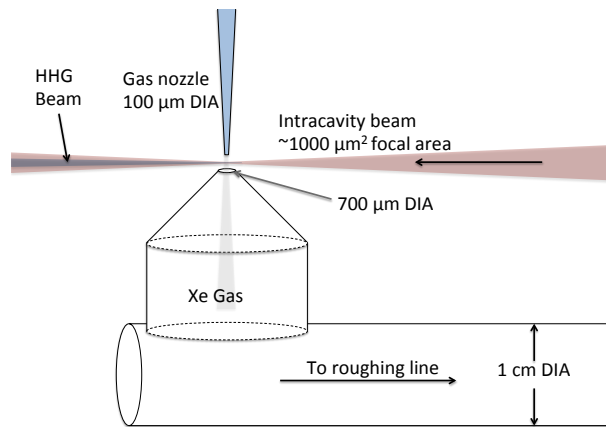
Figure 3.4: Diagram of the focal region within our enhancement cavity. The gas dump is precisely installed so that a majority of the gas emitted from the nozzle is sent to a roughing pump.

chamber absorbs harmonic power. To mitigate this effect we built the cone structured device shown in figure 3.4. This very top of the cone has a 700 μm diameter hole which is placed directly under the nozzle and intracavity beam. The other side of the cone is connected to our roughing pump through a 0.5 m long, 1 cm diameter tube. It turns out that the conductance of the long roughing tube line is actually about an order-of-magnitude higher than the 700 μm diameter hole so a majority of the gas which enters the hole from the nozzle exits without putting load on the turbo pump or causing the background pressure to rise. It is difficult to get the cone sufficiently close so that all the gas from the nozzle enters the cone, however we notice a drop in background xenon pressure of about a factor of 5 with this device installed correctly. After the harmonics are generated, they are outcoupled from the cavity using the diffraction grating output coupling method described in the next section.

3.5   The output coupler

One of the biggest technical challenges to intracavity high harmonic generation is how to outcouple the harmonic radiation. Inside the enhancement cavity, the harmonics are generated collinearly with the fundamental light and will eventually impinge on a cavity mirror. In an enhancement cavity whose main purpose is to increase the efficiency of second harmonic generation, this is usually not a problem because there are coatings for dielectric mirrors that transmit the second harmonic radiation but reflect the fundamental. This is not so easy for an enhancement cavity that produces XUV radiation. This is because there is essentially no solid material that is sufficiently transparent at XUV wavelengths.

In addition, the output coupling technique should not add loss, dispersion, or nonlinearity to the enhancement cavity as these effects can all prevent the efficient coupling between the enhancement cavity and the excitation laser. The original demonstrations of intracavity high harmonic generation used a thin sapphire plate at Brewster's angle for this purpose [33, 34]. Since the index of the sapphire is less than unity at the harmonic wavelengths, one can achieve a large Fresnel reflection of the harmonic radiation while introducing only

a small round-trip loss to the fundamental pulses. This method is not ideal though in that nonlinear processes within the Brewster's plate introduce nonlinear pulse distortion at high intensities, which can limit the power scaling of such a system [77].

Another proposed method for coupling harmonics out of the enhancement cavity is to drill a small hole in the curved mirror after the intracavity focus [78]. Since the harmonic light will diverge less than the fundamental light, most of the harmonic light will pass through the hole, while most of the fundamental light will be reflected. Although this method allows for power scaling, the small hole invariably introduces additional loss to the cavity. This intracavity loss can be somewhat mitigated by coupling a higher-order transverse mode (e.g., TEM_{01}) into the cavity at the cost of losses outside the cavity owing to mode conversion from a TEM_{00} transverse mode to a TEM_{01}. Even so, in practice it is very difficult to keep intracavity losses small using this method. Also, the harmonic radiation generated with a TEM_{01} fundamental beam will display a complicated transverse mode profile that is not ideal for subsequent experiments. A similar proposed technique uses a slotted mirror and two colliding pulses to produce noncollinear HHG [79]. This method also suffers from additional cavity loss for the fundamental light, and the implementation is very challenging technically.

Our solution to these challenges is to use a special optic as an output coupler that serves a dual purpose– it is a diffraction grating for the harmonic radiation but a low-loss mirror for the fundamental. To manufacture this optic, we utilize a dielectric mirror coating, engineered for low dispersion and high reflectivity at our fundamental wavelength of 1070 nm with a 70° angle of incidence and with s polarization. The top layer of this coating is SiO_2 and we etch a 420 nm period diffraction grating directly into this surface. This optic is placed directly after the intracavity focus so that the fundamental radiation takes a shallow bounce off of it before continuing on to the second curved mirror. In figure 3.5, we depict the cross section of this optic. In principle the diffraction grating structure does not produce loss for the fundamental light because the period of the grating is small enough so that only zeroth-order diffraction is possible and the optic looks like a perfect mirror. For the harmonic
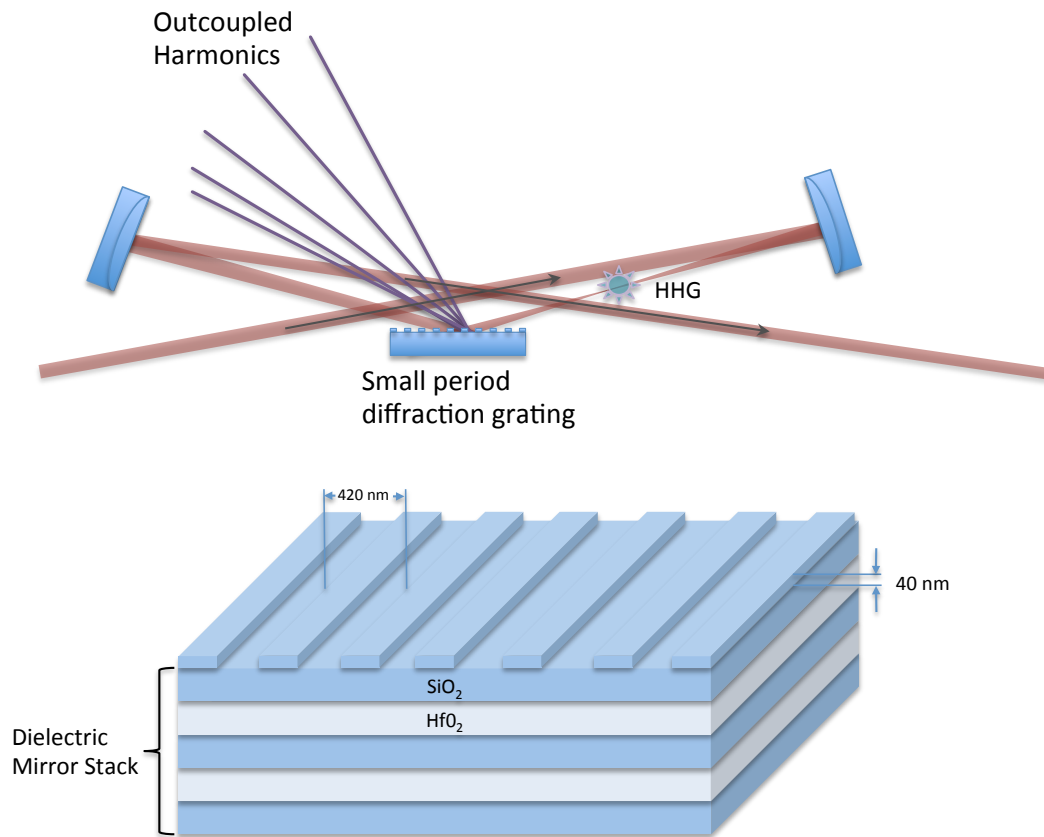
Figure 3.5: Diagram showing the operation of the subwavelength diffraction grating as an intracavity harmonic output coupler.

Table 3.1: Theoretical Efficiency of the Grating at Harmonic Wavelengths of the Incident 1070 nm Radiation

Harmonic Order	λ (nm)	coupling efficiency
3	357	0.7%
5	214	1.9%
7	153	3.5%
9	119	9.6%
11	97.3	8.5%
13	82.3	9.0%
15	71.3	10.3%
17	62.9	9.6%
19	56.3	8.4%
21	51.0	6.7%

wavelengths, however, there is substantial diffraction efficiency with the largest power being diffracted into the first order.

The efficiency of this optic at XUV wavelengths is proportional to the Fresnel reflection from the surface of the grating structure. For this reason the incident angle was designed to be 70° since the reflectivity always increases for larger incidence angles with s polarization. There is a tradeoff, however, in that the diffraction grating efficiency will drop at very high angle of incidence for an unblazed grating structure. Nevertheless, for the ninth through nineteenth harmonics, the Fresnel reflection is ≈45% with s polarization at a 70° angle of incidence.

To estimate the output coupling efficiency of the intracavity grating, it is crucial that we take into account the diffraction grating efficiency as well as the Fresnel reflection coefficients. For this purpose, we used an approximation of the rigorous integral method described in [80] with the index and absorption values taken from [81]. We maximized the efficiency for the ninth through nineteenth harmonics by adjusting the period, duty cycle, and feature height of the grating. The final grating design has a period of 420 nm, a duty cycle of 40%, and a step height of 40 nm, as shown in figure 3.5. The calculated output coupling efficiencies

are shown in Table 1. Owing to limitations in the manufacturing capability, the grating structure we used had a 47% duty cycle, which affected the performance minimally. After our initial report of this technique [82], another group etched an appropriate blazed structure into the surface of a high reflector [83] to increase the efficiency for a specific harmonic order using this method (optical characterizations were performed but the device has not yet been used to outcouple HHG radiation).

As it turns out, the efficiency of the grating at XUV wavelengths is highest when the period of the grating is as long as possible while still being short enough to have no diffracted orders for the fundamental radiation. The fundamental radiation incident on a subwavelength diffraction grating will produce an evanescent wave with decay constant, α, given by:

$$\alpha = 2\pi\sqrt{\left(\frac{\sin(\theta)}{\lambda} + \frac{m}{\lambda_g}\right)^2 - \frac{n^2}{\lambda^2}} \tag{3.1}$$

where λ is the vacuum wavelength of the fundamental radiation, λ_g is the grating period, n is the index of the upper layer of the dielectric stack (in our case SiO_2 with an index of 1.45), θ is the angle of incidence and m is the order number. Equation 3.1 is found by matching boundary conditions at the grating surface. For the highest diffraction efficiency, α approaches zero for $m = -1$ and the evanescent wave extends deep into the upper layer of the dielectric coating. It is important to take this evanescent wave into consideration when designing a grating output coupler. If the evanescent wave extends to the first high index layer of the dielectric stack (with an index of 1.9), α will be imaginary in that layer- this corresponds to a traveling wave. Therefore optical power can be coupled to a waveguide comprised of the first high index layer of the mirror dielectric stack sandwiched between low index SiO_2 layers. Through this mechanism, the fundamental radiation incident on the optic can experience additional loss. The waveguide coupling efficiency depends on the precise wavelength and angle of the grating [84]. For our grating parameters α is equal to 0.004 nm^{-1} so that the electric field drops to its 1/e value in 250 nm.

In figure 3.6, we compare intracavity spectrum for similar grating designs the first with a 100 nm thick upper SiO_2 layer ($0.4 \times$ the $1/e$ decay constant) and the second with a 460 nm upper layer ($\sim 2 \times$ the $1/e$ constant). As can be seen from the figure, the thinner SiO_2 upper layer can efficiently couple power into the high index layer producing loss at certain wavelengths. This effect is absent for the thicker upper layer since the power in the evanescent wave has decayed by $1/e^4$. In principle, one could also decrease the waveguide coupling efficiency by decreasing the period of the diffraction grating, but this tends to decrease the grating efficiency for the harmonic wavelengths whereas increasing the upper layer thickness has no effect on the grating operation in the XUV.
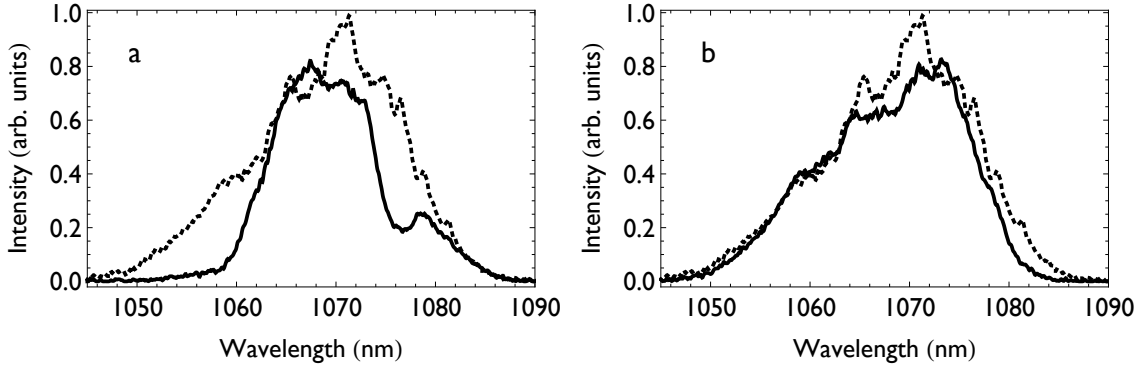
Figure 3.6: The laser spectrum incident on the enhancement cavity is compared with the intracavity spectrum for two different designs of grating output coupler. a) solid curve is the intracavity spectrum for grating output coupler with 100 nm SiO2 top layer. Dotted curve is the incident spectrum for comparison. b) same as in a) but with 460 nm SiO2 top layer for which the lack of evanescent waveguide coupling is clearly evident. Some difference between the incident and the intracavity spectra is attributed to intracavity mirror dispersion.

When we first developed this output coupling technique, we utilized a different but very similar amplified Yb-fiber frequency comb to that already described. Specific details of the laser system can be found in [85, 86]. Before enhancement, that laser system produces 10 W of power with 75 fs pulses at a 136 MHz repetition rate. The focus in our cavity is achieved with two 10 cm radius of curvature mirrors that produce a calculated focused spot area of 960 μm^2 and hence a peak intensity of 4×10^{13} W/cm^2.

We were able to measure the power in the thirteenth harmonic with an XUV-sensitive diode coated with 200 nm of In and 20 nm of MgF_2. At the time the cutoff of our harmonic radiation was observed to lie between the nineteenth and the twenty-first harmonics. This was the first demonstration of the seventeenth through twenty-first harmonic orders via intracavity HHG. When we compare the measured power in the seventeenth harmonic at 63 nm ($\sim$ 50 nW) with previous results at 61 nm [34] (the thirteenth harmonic of 795 nm fundamental light), we saw an increase in the output coupled power by nearly 4 orders of magnitude [82]. We attributed this dramatic increase in usable harmonic power to the ability of using a laser with higher peak powers for the intracavity experiment without being plagued by nonlinear dispersions introduced by an intracavity Brewster's plate. This satisfied our initial design goals– the potential for power scaling in intracavity HHG

An additional feature of the diffraction grating method which is often an advantage is that the harmonics are already spectrally dispersed when they exit the cavity. Any output coupling technique that sends harmonic and fundamental radiation from the cavity collinearly will usually require spectral filtering to select only the desired harmonic for following experiments. The two most common methods to achieve this filtering are with diffraction gratings or thin metallic filters. Without this filtering, spectroscopic experiment must be designed to be impervious to the potentially ionizing radiation of the high harmonics and the ac stark shifts from the lower harmonics and the fundamental radiation. In the XUV, such spectral filtering will typically possess only 10% - 20% efficiency under good conditions. By combining the spectral filtering element and the output coupler into a single unit we are thus able to deliver roughly an order-of-magnitude more photons to spectroscopy experiments. Additionally, the small-period diffraction grating method produces a TEM_{00} harmonic beam as compared with other output-coupling methods relying on higher-order transverse-mode fundamental beams [78, 79, 87]. When doing spectroscopy with relatively low power and using spectroscopic techniques that are susceptible to scattered background radiation, a TEM_{00} harmonic beam provides a major advantage.

In many ways, this output coupling scheme is ideal. It essentially introduces no adverse affects to the optical cavity that wouldn't also be present with the addition of a single high-reflectance dielectric mirror. For some experiments, though, one may want to keep the harmonics undispersed (attosecond pulse generation or some two-photon spectroscopy experiments) and therefore the need for other output coupling schemes still exist. Interestingly, it seems that as frequency combs continue to increase in average power, enhancement cavities may be able to generate harmonics even at very low finesse. This may make the detriments of the nonlinear phase shifts in the Brewster's plate output coupling method not so serious for future experiments. In fact, there has recently been a demonstration of high repetition rate (20.8 MHz) HHG with no enhancement cavity at all [88].

Chapter 4

Phase noise studies of high harmonic frequency combs

This chapter presents several in depth studies of the ultimate phase stability and comb linewidth of the high harmonic frequency comb. These are imperative investigations since the HHG comb was developed for the main purpose of high resolution spectroscopy. If the phase coherence is destroyed in the high harmonic generation process then much of this effort was in vain. Our estimations of the upconversion of noise in the HHG process, discussed in Chapter 1, led us to believe that the production of VUV and XUV frequency combs was possible. However, understanding these noise processes was so pertinent to our scientific goals that it necessitated more detailed investigations, and in particular, direct experimental verifications.

4.1   Study of the below-threshold harmonic dipole phase

As discussed in Chapter 1, it is clear that a good understanding of the intensity-dependent dipole phase is necessary to place a limit on how much intensity noise can be tolerated in an intracavity HHG system while still preserving phase coherence. The α_q parameters for harmonics that have energy far above the ionization energy of the target gas have been well studied, but many of the harmonic orders we are interested in using for spectroscopy are near 100 nm in wavelength– very close to or below the ionization energy of the target gas (the ionization potential of xenon is at a wavelength of 102 nm). Clearly our intuition from the semiclassical picture of harmonic generation breaks down for harmonics

near or below the ionization potential because in that picture the minimum harmonic energy possible is given by the ionization potential. Therefore, we decided to investigate the α_q parameters for the below-threshold harmonics whose magnitude and even existence was not initially known. Our collaborators Jennifer L. Tate, James Hostetter, Mette B. Gaarde and Kenneth J. Schafer provided outstanding theoretical support for the following work.

The α_q parameters can produce several measureable effects– two clear physical manifestations are a unique beam profile in the far field and in oscillations of the harmonic flux as a function of intensity. The shape of the harmonic beam in the far field is easily understood. Since, typically, the fundamental beam posesses a Gaussian transverse mode, at the focus the variation of the intensity across the beam will imprint a Gaussian phase shift upon the high-harmonic beam whose magnitude is proportional to α_q. This lensing effect will increase the harmonic beam divergence. Since there are two trajectories for above-threshold harmonic generation, in the far-field one can usually observe a bright central spot that is a result of a small lensing effect (the short trajectories), surrounded by a more divergent beam that seems to form a "halo" around the central spot (the long trajectories). The amount of defocus in the far field can indicate the magnitude of the α_q parameters. In the central part of the beam, both trajectories are overlapped and can interfere with each other. As the intensity generating the harmonic power is increased, the central part of the beam will cycle through constructive and destructive interference. This behavior is shown for our below-threshold harmonics in figure 4.1. The insets show the beam profile of the corresponding harmonics. The data is consistent with the existance of two trajectories in that the aforementioned beam profiles seem to manifest themselves in our below-threshold harmonics. Also, as expected, we see interference between the two trajectories on axis which manifests itself in oscillations of the harmonic power as the fundamental intensity is increased. For the 9th and 13th harmonics, the halos seem to be largely absent and therefore there are no real prominent oscillations in the harmonic power, again confirming that our interpretation of two trajectories as being responsible for both features is correct. The absence of a long-trajectory for some of the
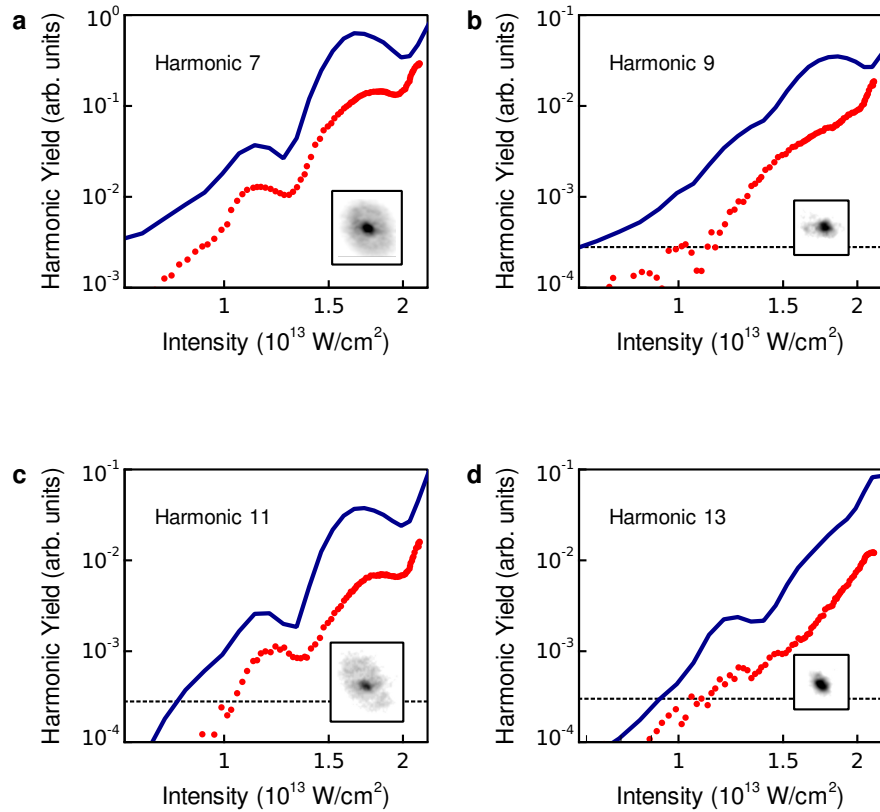
Figure 4.1: Harmonic yield as a function of the intensity at the center of the xenon jet. a) through d) Harmonics 7 to 13, respectively. The red filled circles are measured and the blue solid lines are theory, both for the on-axis yield. The harmonic yields are all roughly proportional to the sixth power of the driving intensity. The horizontal dashed lines in b) through d) show the noise floor of the CCD camera. Theoretical harmonic yields were scaled in magnitude to offer a clear comparison. The insets show the far-field spatial profile for each harmonic. Halos on the beam profile and strong oscillations in the intensity-dependent yield are clearly visible in harmonics 7 and 11, providing clear evidence of multiple generation pathways with distinct intensity-dependent phases.

harmonics is, thus far, only understood through the theoretical model without any deeper physical interpretation.

The solid lines in figure 4.1 are the theoretical calculations for the harmonic yield obtained by means of the coupled, non-adiabatic solutions of the time-dependent Schrödinger equation and Maxwell's equations for a gas of xenon atoms exposed to a 1070 nm laser pulse using the single-active-electron approximation [55, 89]. The theory values are offset from the experimental values for clarity. The good reproduction of the experimental result gives us confidence in the theory model.

The result of the theoretical calculation yields the dipole moment as a function of intensity for each harmonic order. Further analysis can be applied to understand the contributions of different trajectories to the result. For this purpose the following transform was used

$$\tilde{d}_q(\tilde{\alpha}_q, I_0) = \int d_q(I) e^{i\tilde{\alpha}_q U_p(I)/\hbar\omega} W(I - I_0) \mathrm{d}I \tag{4.1}$$

where $W(I - I_0)$ is a window function centered on I_0, $\tilde{\alpha}_q = \alpha_q \frac{\hbar\omega I}{U_p(I)}$ and q represents the harmonic order. This expansion will basically provide the contribution of different trajectories to the atomic dipole as a function of intensity. The physical basis of the expansion is the ansatz that the intensity dependent dipole phase is well approximated by piecewise linear contributions. The expansion is plotted for the harmonic orders shown in figure 4.2. From the figure, it seems that the main contribution atomic dipole comes from trajectories with $\tilde{\alpha}_q$ contributions around 0 and 2.5π. The difference in these two main $\tilde{\alpha}_q$ values is confirmed by the oscillation period in the experimental data shown in figure 4.1.

Therefore, we find that there are indeed intensity-dependent phases for the below-threshold harmonics which are analogous to the $\tilde{\alpha}_q$ parameters for above-threshold harmonics. Interestingly, though it seems that the $\tilde{\alpha}_q$ parameter for the trajectory analogous to the long trajectory is marginally larger than for above threshold harmonics. Our estimates above for the intensity variation necessary to obtain significant phase modulation of the
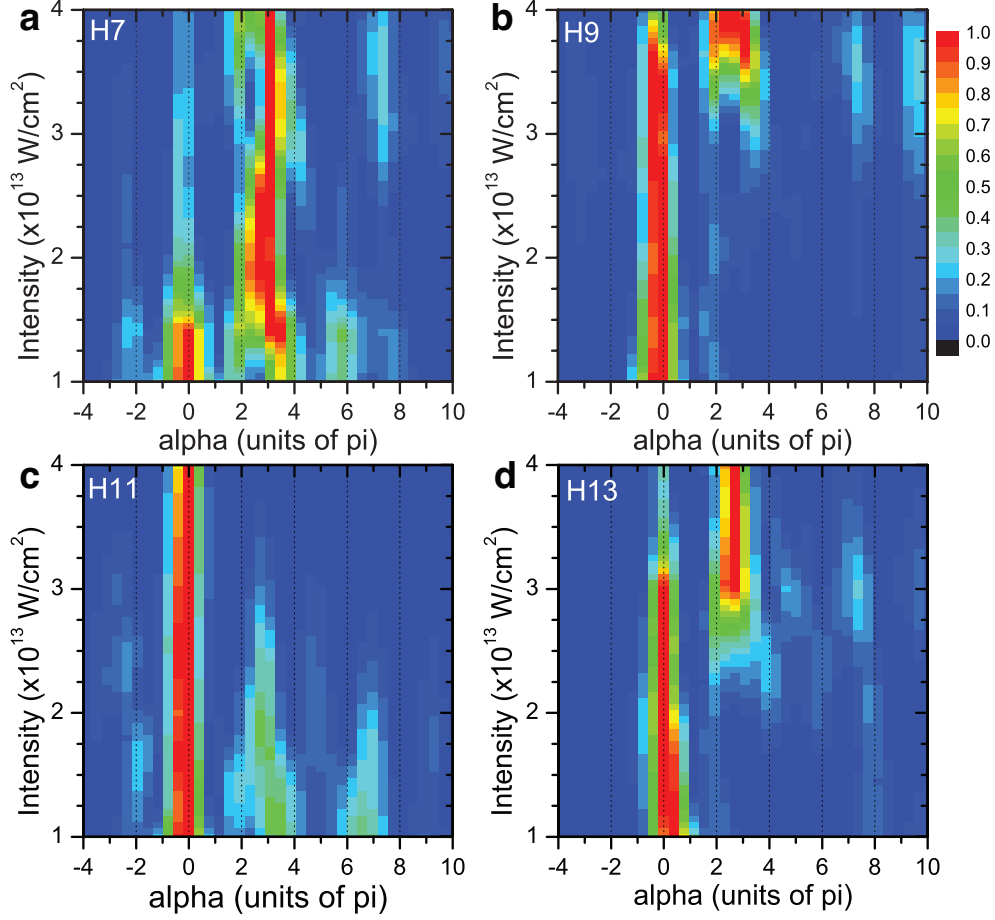
Figure 4.2: Quantum path distributions calculated for the 7th through 13th harmonic orders. The color scale has been normalized for each intensity and shows only relative strengths. The 7th and 11th harmonic orders show large quantum path contributions at $\tilde{\alpha}_q \approx 0$ and $\tilde{\alpha}_q \approx 3\pi$ that manifest themselves in the spatial profiles with halos and intensity-dependent yields with large oscillations, as shown in figure 1. The 9th and 13th harmonics do not show prominent contributions for $\tilde{\alpha}_q > 2\pi$ at intensities below 3×10^{13} W cm^2 for the 9th harmonic and 2.5×10^{13} W cm^2 for the 13th harmonic, so the features indicative of multiple quantum paths are largely absent at the driving intensities present in the experiment.

harmonics is still roughly correct. This value of amplitude-to-phase noise conversion, while not negligible, seems to be very manageable for the production of an ultraviolet frequency comb.

It is interesting to ask how we can maintain our semiclassical picture of classical electron trajectories in light of these results. As was mentioned earlier, the lowest harmonic photon energy which can be obtained in the semiclassical picture is the ionization energy of the target atom. Luckily we can keep the semiclassical picture at least in part if we consider that the effect of the spatial extent of the potential of the ion is ignored in the standard semiclassical approximation. If we include this effect, then for a long-trajectory electron, right before the electron recollides with the parent ion the external electric field is opposing its motion. This has the action of lowering the potential for recombination as compared to an unperturbed ion. This allows the emission of a below-threshold photon. For the short-trajectories, the electron recombines with the parent ion when the field is still accelerating it towards the parent ion. Therefore, it is impossible for a classical electron trajectory to adequately explain the presence of the trajectory near $\tilde{\alpha}_q = 0$. This short-trajectory contribution seems instead to arise from high-order multiphoton processes [90].

4.2 Noise propagation to the intracavity field

In the previous sections we have examined how noise processes occur in the high harmonic process itself given a certain intracavity field. Here we examine the way in which noise processes in our excitation laser are transferred to the intracavity field. Finally, we present a robust method to decrease the relevent noise in the excitation laser.

Due to the intracavity photon lifetime, the enhancement cavity is effectively a low-pass filter for phase and amplitude fluctuations of the excitation laser. It would be dangerous, however, to assume that this results in an XUV frequency comb with less phase noise than if the cavity were absent. This is because, within the bandwidth of the cavity, there is a conversion between the phase-noise of the excitation laser to amplitude-noise in the intracavity

field. Due to the APC processes in the high harmonic process discussed above, it is crucial to remove laser phase noise at Fourier frequencies within the cavity bandwidth because the phase noise of the excitation laser is not greatly attenuated and it also produces significant amplitude noise in the intracavity field.

The relative intensity noise of our excitation laser is much smaller than the intensity noise within the enhancement cavity precisely because of the phase-to-amplitude noise action of the cavity. Another noise source is environmental perturbations to the enhancement cavity but these perturbations lie well below our cavity locking bandwidth of $\sim$ 35 kHz. Our excitation laser, on the other hand, contains significant phase noise out to hundreds of kHz which is both outside our locking bandwidth and on the same order of magnitude as our cavity HWHM linewidth of $\sim$ 200 kHz. The line broadening implications for this high frequency phase noise will be more relevent than the low-frequency phase noise that lies within our cavity locking bandwidth. So while there are different physical processes which transfer noise from our intracavity field to the harmonic field the amplitude and phase noise of the intracavity field come predominantly from a single source; the phase noise of the excitation laser. Therefore, if we can eliminate or reduce that noise source, we have made real progress on all fronts.

Our laser system has a significant amount of phase noise at Fourier frequencies near 100 kHz, which is too high to be due to environmental perturbations. One of the most significant sources of phase noise that has been observed in fiber-based frequency combs is a result of residual intensity noise of the oscillator pump laser diode [91, 92]. Since pump diode intensity noise can easily produce fast fluctuations, it is reasonable for us to suspect this as a significant source of noise for our system. To mitigate this effect, we have a choice to either detect and supress this phase noise with our frequency actuators or to supress the noise source from the outset by decreasing the pump diode noise directly.

In principle, either approach would work but the issue is complicated by the fact that our frequency comb has two degrees of freedom and noise from the oscillator pump diode will

not produce fluctuations in the frequency comb in f_0 or f_r alone but in a linear combination. As discussed earlier, an easy way to conceptualize this is by assuming that there is a fixed point in the frequency comb (which may or may not be within the spectral bandwidth) which will not be affected by the particular noise process in consideration with the other comb modes "breathing" about this point in response to perturbations (it should be emphasized that every noise process or frequency actuator will, in general, have its own, unique fixed point). Therefore it is difficult to build a feedback loop which perfectly cancels this noise across the entire comb without a good understanding of the position of the fixed point and a highly enginee frequency actuator. Most likely, as long as the fixed point is not too close to the center of the spectrum, the noise will be predominantly on the translation mode and not on the central breathing mode (as defined in Chapter 3) and therefore actuating on the cavity length to eliminate this noise could be acceptable. Unfortunately, we found it difficult to measure the fixed point of our frequency comb when the pump intensity was modulated. This was in part because the fixed point seems to shift with actuation frequency. Therefore we chose to attempt to eliminate the noise at its source and suppress the pump diode RIN directly.

Other groups have studied the effects of pump induced phase noise on fiber based combs [91, 92]. In reference [91], the laser pump diode residual intensity noise (RIN) was supressed in an Erbium fiber comb by utilizing a property of the laser diode whereby the RIN decreased when operated in a high-power regime. Therefore they operated the diode in the high power regime and attenuated the output before pumping the fiber comb. This supressed the phase noise of their oscillator up to a Fourier frequency of about 80 kHz. We chose a different route and utilized an active noise servo because 1) Our diode is already operated in a high power configuration, 2) it is possible to supress noise to much higher Fourier frequencies in principle, and 3) it allows for more flexibility in system design. Through the course of this work, we discovered that the high frequency phase noise (above a few kHz) of our oscillator actually had two contributions- the pump diode RIN and amplified spontaneous emission.

Our results showed that we could supress both contributions to varying degrees with our active noise servo.

An obvious implementation for the noise servo is to detect the pump diode RIN and then feed back on the current to the pump diode to supress this noise. For the technical reason that the pump diode was fiber coupled directly to the oscillator, it was impossible for us to monitor the pump diode power directly without invasive alterations to our system. However, we did have access to a monitor of our oscillator output and we knew that the fluctuations in laser diode intensity should be highly correlated with the intensity fluctuations of our oscillator. Therefore, we chose to monitor the oscillator output and apply negative feedback onto the current driver of the pump diode. We obtained a duplicate pump diode module to study the pump diode intensity noise which was useful for understanding the system.

We detected the intensity noise of the oscillator with a home-built detector with a bandwidth of 10 MHz that was shot noise limited at > 20 μW of optical power. These specifications by themselves can be easily obtained in a commercial detector. However, for the purposes of our feedback loop, we required that the detector have a large gain (40 dB), low-delay and no response at frequencies below a few Hz. No commercial detector was available with all these requirements and we were forced to build our own. We used this detector both for our measurements of the intensity noise of the oscillator and to implement the servo.

The intensity noise at several different pump diode currents above the modelocking threshold current, I_{th}, are shown in figure 4.3a. We can easily see a relaxation oscillation near 400 kHz, especially near the modelocking threshold (the noise spike at 200 kHz is technical in nature and not related to the relaxation oscillation). In contrast, we measured the intensity noise of our replicate pump diode module to be -130 dBc and flat in Fourier frequency out to about 5 MHz. Figure 4.3b shows the response of the oscillator intensity and the pump diode intensity to current modulation applied to the pump diode. These traces
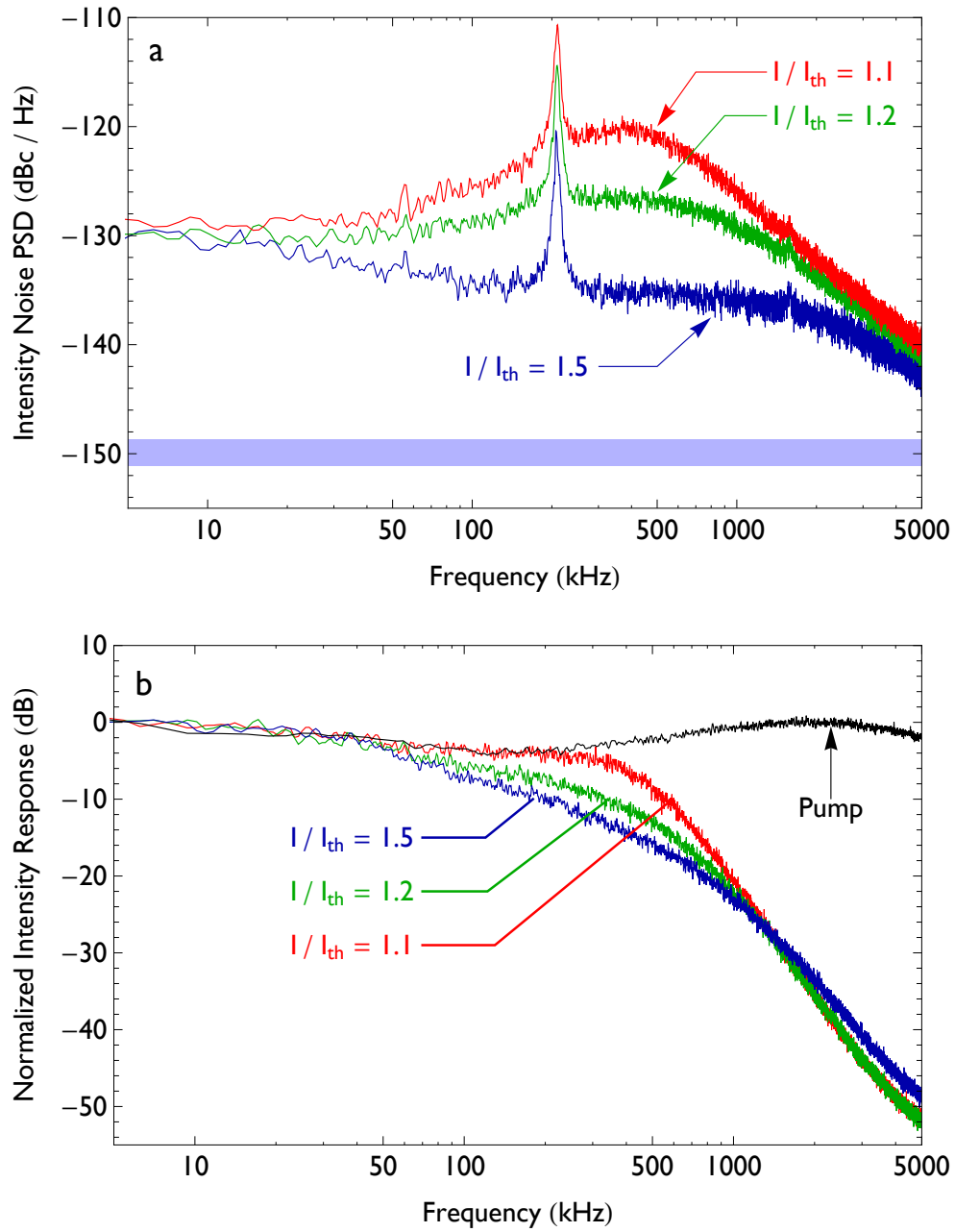
Figure 4.3: Intensity noise spectrum of the Yb oscillator at various pump powers normalized to dc signal. The shaded box indicates the shot-noise floor of the measurements. (b) Intensity modulation transfer functions for the oscillator and the pump diode.

were obtained by applying white noise to the diode current and measuring the resulting noise on a real time spectrum analyzer. Comparing figures 4.3a and 4.3b, we notice that above 1 MHz the response of the oscillator intensity to diode modulation falls off as $\sim$15 dB per octave but the laser intensity noise falls off only as 8 dB per octave. Therefore, this gives a strong indication that there are other noise sources present in addition to the RIN of the pump diode that begin to dominate at high Fourier frequencies. We hypothesize that this contribution is from quantum noise sources.

The noise sources which fall under the broad category of quantum noise include amplified spontaneous emission, fluctuations in the linear losses in the cavity, and the vacuum fluctuations entering through the output coupler. For a rigorous discussion of the effects that quantum noise sources can produce in mode-locked lasers see reference [93]. The responses of the oscillator intensity to pump and quantum fluctuations can be described by the transfer functions $T_p(f)$ and $T_{qn}(f)$, respectively. We can derive the relative functional form of these two transfer functions by solving the semiclassical rate equations for the pulse energy and making the simplifying assumption that all quantum noise sources are due to ASE (other quantum mechanical noise sources should enter the equations in a similar fashion). We take as our starting point the coupled differential equations relating the pulse energy and the gain within the laser cavity [94].

$$\dot{P} = (Se^G - 1)P + BG, \tag{4.2}$$

$$\dot{G} = a\left[R - G(1 + P)\right]. \tag{4.3}$$

Here P is the intracavity intensity divided by the saturation intensity, S is the photon survival rate ($S = 1 - \text{Loss}$), G is the gain, R is the pump rate divided by the saturation intensity, B is the fraction of relaxation processes (the upper state lifetime of Yb is $\sim 1 - 2$ ms) that yields a photon into the laser mode, and a is the ratio of the round trip time to the relaxation time of the lasing level. The time dependence is in terms of $t' = t/t_r$ where t_r is the repetition period. All quantities have time dependence except S and a. It is possible to associate

a physical meaning to each term in equations 4.2 and 4.3. For equation 4.2, $(Se^G - 1)P$ describes the amplification by stimulated emission and round trip cavity loss whereas BG describes spontaneous emission emitting photons into the laser mode. For equation 4.3, aR describes the pumping processes producing gain, $-aG$ describes a decrease in the gain from relaxation processes, and $-aGP$ describes a decrease in the gain from stimulated emission. We can simplify the equations by expanding each variable in terms of a steady state time independent portion and a smaller time dependent quantity. We therefore use the general rule $X \Rightarrow X_0 + x(t)$ to arrive at:

$$\dot{p} = (Se^{G_0}e^g - 1)(P_0 + p) + (B_0 + b)(G_0 + g), \tag{4.4}$$

$$\dot{g} = a\left[R_0 + r - (G_0 + g)(1 + P_0 + p)\right]. \tag{4.5}$$

Here, the lower-case variables all have an implied time dependence which is not written. Now we assume the the lower-case variables are all small compared with their upper-case counterparts. This means that $e^g \approx 1 + g$ and we will drop any products of two time-dependent variables. This has the added benefit of linearizing the equations. Furthermore we know that by setting the time-dependent variables equal to zero, the differential equations will have the steady state solutions relating the upper-case variables that can be used for further simplification. With all these simplifications, we arrive at

$$\dot{p} = gP_0 + B_0 g + G_0 b, \tag{4.6}$$

$$\dot{g} = a\left[r - G_0 p + g(1 + P_0)\right]. \tag{4.7}$$

We can now eliminate g from the equations above and arrive at a single equation just in terms of p.

$$\ddot{p} + a(1 + P_0)\dot{p} + a(P_0 + B_0)G_0 p = a(P_0 + B_0)r + a(1 + P_0)G_0 b + G_0\dot{b}. \tag{4.8}$$

The left-hand side of the equation is the differential equation governing the laser dynamics whereas the right hand side is the driving terms. Changes in the pump rate, r, drive

the system as $a(P_0 + B_0)r$. Variations in the amplified spontaneous emission rate drives the differential equation as $G_0 \left[a(1 + P_0)b + \dot{b} \right]$. It is easy to estimate that the $\dot{b}$ term begins to dominate over the $a(1 + P_0)b$ term at a frequency of ~ 1 kHz for our laser system. Therefore, for the frequencies of interest, we find that the pump diode fluctuations (which will produce variations in r) drive the differential equation directly whereas the first derivative of the amplified spontaneous emission drives the differential equation. Thus, the two transfer functions are related approximately by $T_{qn}(f) \propto T_p(f)f^2$. There have been more rigorous treatments that also agree with this result qualitatively, such as analytic quantum models for cw lasers [95] and numerical simulations of mode-locked lasers [96]. Thus, we compare a simple model of the form $aT_p + bT_{qn}$ to the measured intensity noise spectra to retrieve the relative contribution of the noise sources. This analysis reveals that the quantum noise begins to dominate over the pump noise at Fourier frequencies of 70, 80, and 180 kHz for pump current conditions of 1.1, 1.2, and 1.5 times I_{th}, respectively.
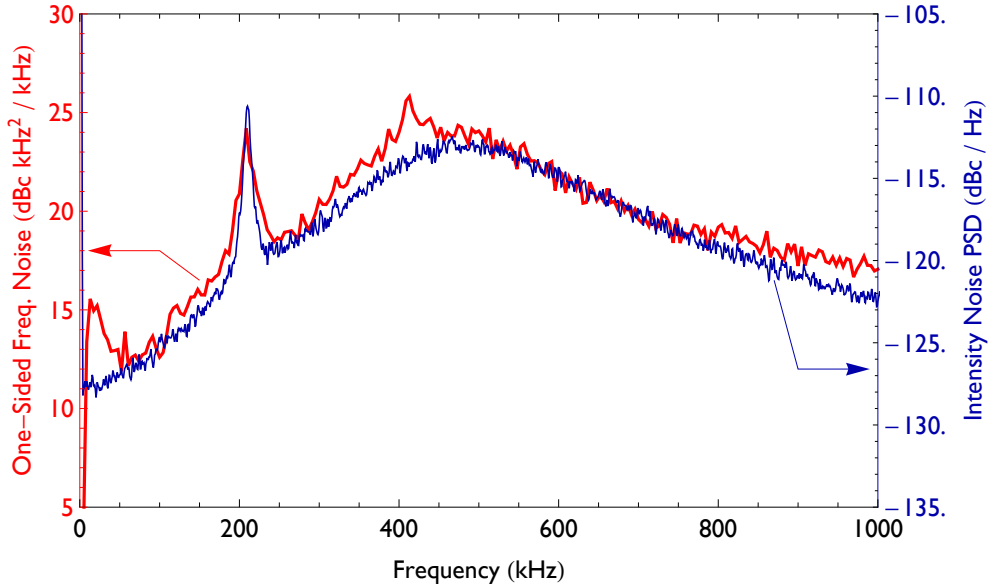
Figure 4.4: Comparison of the intensity noise spectrum with the frequency noise of a comb tooth near the optical carrier for $I \approx 1.1\ I_{th}$.

All of the previous discussion has been to find the the source of pulse energy fluctuation

in our oscillator. It is still necessary to confirm that the fluctuations in our pulse energy are the ultimate source of the phase noise. There are a multitude of amplitude-to-phase noise conversion processes that occur within a modelocked oscillator [91]. Since all of these processes are occuring inside the laser cavity, an increase in the pulse energy will produce a phase shift every round trip of the pulse which corresponds to a frequency shift of the generated comb. Therefore we are looking for a correlation of oscillator intensity noise to frequency noise (as opposed to phase noise). As a reminder, the frequency noise power spectral density and the phase noise power spectral density are related by $PSD_f = f^2 \times PSD_\phi$.
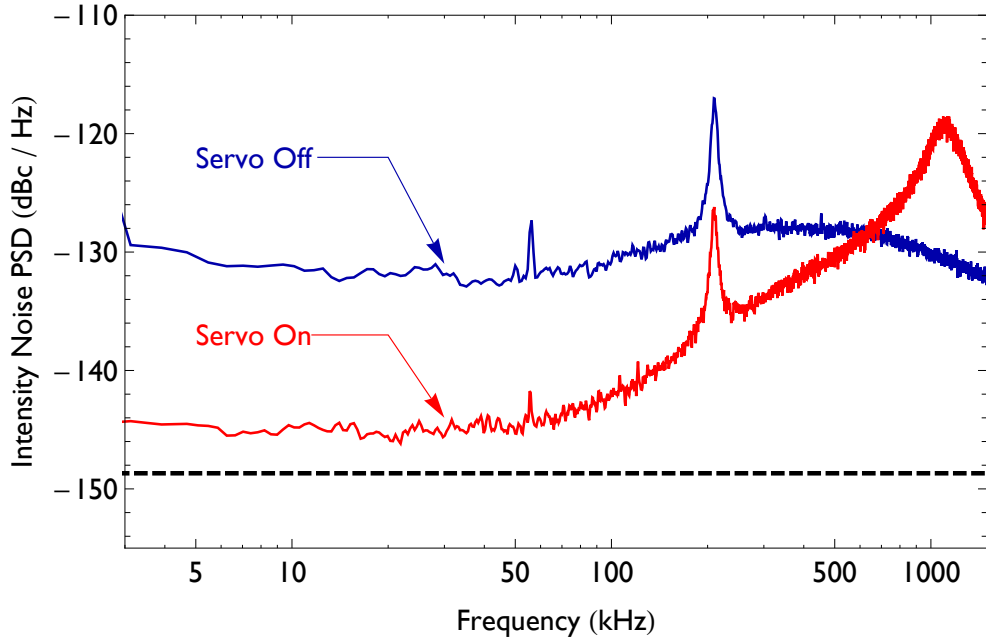
Figure 4.5: Intensity noise spectrum of the oscillator with and without the servo action. The dashed line indicates the shot-noise floor.

The frequency noise near the optical carrier frequency was measured by loosely phase locking a comb tooth to a cw 1064 nm nonplanar ring oscillator (NPRO) using our piezo-electric actuator that controls the oscillator cavity length. Figure 4.4 shows the comparison of the intensity and frequency noise spectra for $I = I_{th} \approx 1:1$. The frequency spectrum

between 50 kHz and 1 MHz is strongly correlated with the intensity spectrum, indicating that the frequency noise does indeed predominantly arise from pulse energy fluctuations. It also becomes clear that the amplitude-to-frequency noise conversion in the oscillator arises from both pump noise and quantum noise sources, with the latter begin to dominate for Fourier frequencies higher than the relaxation oscillation.

At this point, we can summarize our findings of the source of the frequency noise. We conclude that the main contribution to the frequency noise is through amplitude-to-phase noise conversion within the laser oscillator. The source of this amplitude noise arises from both amplified spontaneous emission and intensity noise of the pump diode. Of course, ASE will directly add frequency noise as well but from the high correlation of intensity and frequency noise that we observe, this noise source is apparently not dominant in our laser. We therefore built a servo to reduce the amplitude fluctuations of the oscillator output that should reduce the noise from amplitude-to-phase noise conversion- whose ultimate source is ASE and pump RIN. Of course, the effect of ASE directly adding phase noise without an amplitude-to-phase noise conversion process is also present at some lower level and will not be reduced with the intensity stabilization servo.

The error signal for the servo was derived from the oscillator output using the photodetector described above. The loop filter consisted of a single proportional/integral stage, with two cascaded lead stages in order to combat the two-pole amplitude roll-off and phase lag introduced by the measured transfer function shown in figure 4.3. The output of the servo was simply fed back to the current modulation input of the pump diode. This creates a very robust intensity noise servo.

Figure 4.5 shows the action of the noise servo on the in-loop intensity noise of the oscillator at a pump current of $\frac{I}{I_{th}} = 1.2$. The noise servo reduces intensity noise by $\sim$15 dB out to a Fourier frequency of $\sim$100 kHz with a unity gain frequency of 700 kHz. The fact that we are able to push the unity gain frequency past the relaxation oscillation is due to the cascaded lead stages. The corresponding reduction in phase noise was characterized out
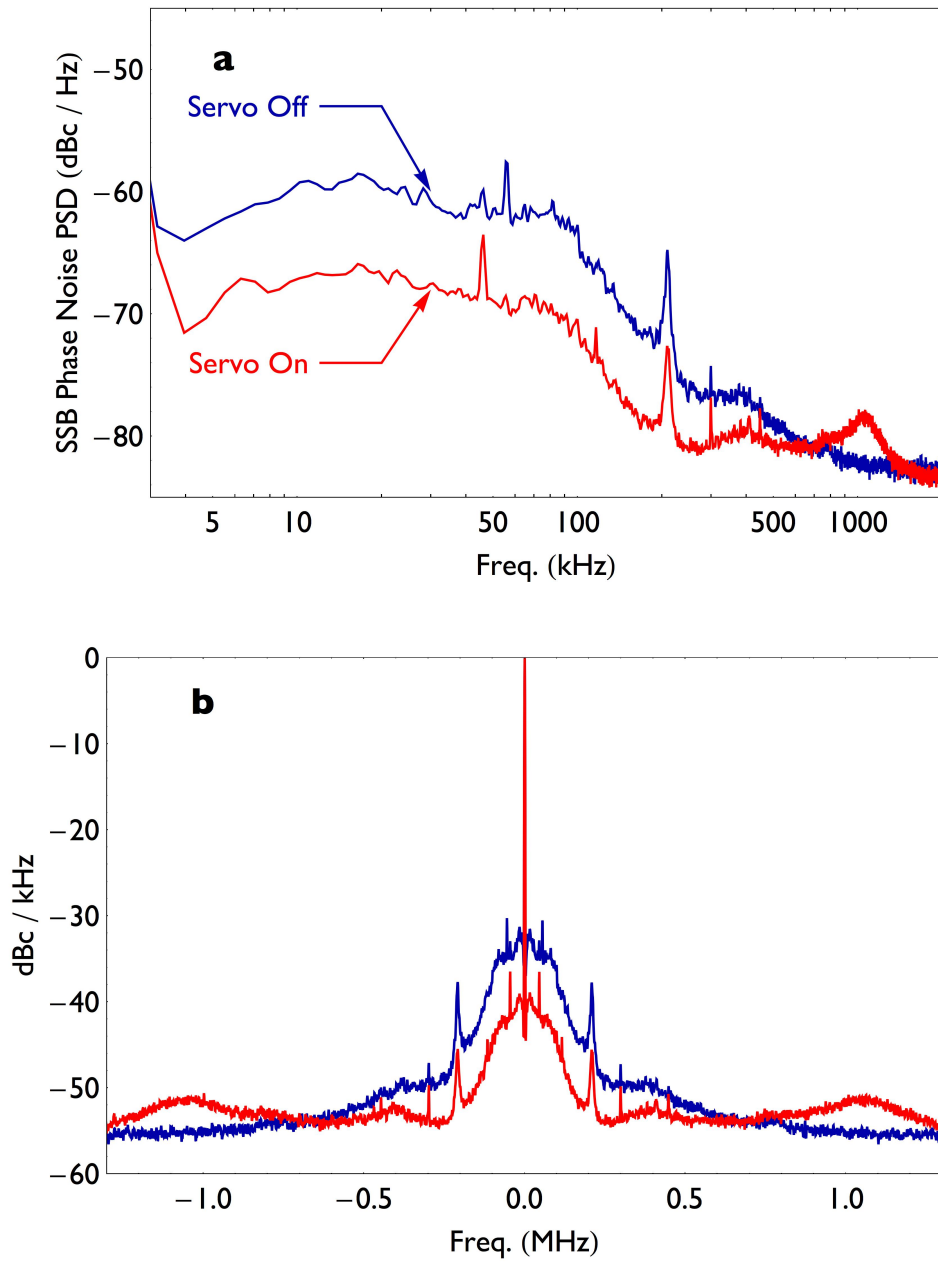
Figure 4.6: a) Reduction in the phase noise near the carrier frequency due to the servo b) rf spectrum of the phase-locked optical beatnote.
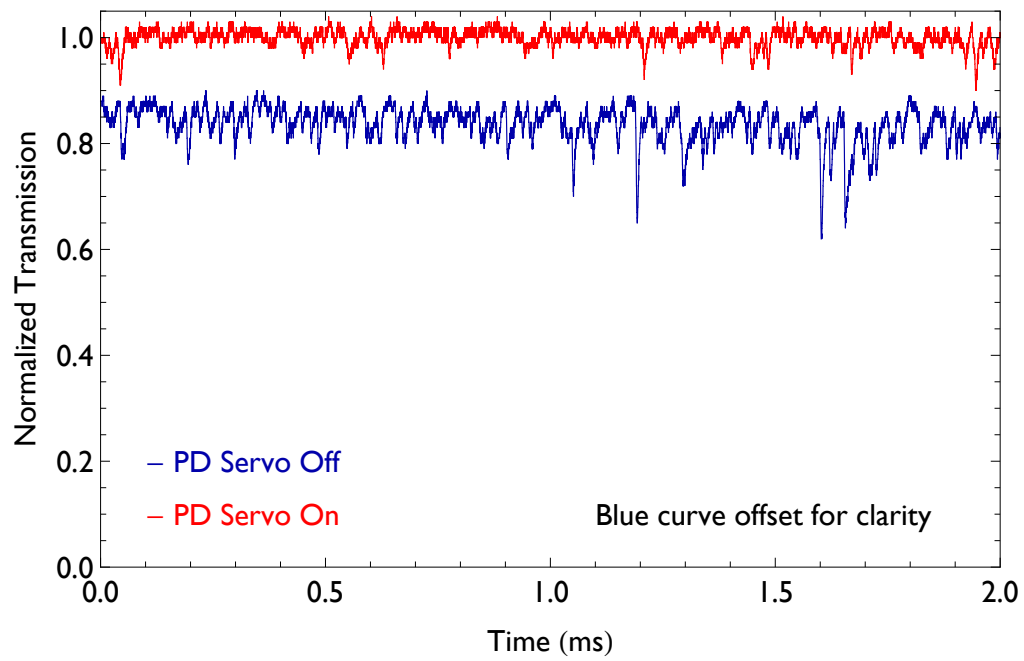
Figure 4.7: The intracavity intensity noise both with and without the action of the noise servo. The blue curve is offset for clarity. The measurement bandwidth is > 200 kHz so the predominance of relevent noise shown in figure 4.6 is included.

of loop using the heterodyne optical beat between the comb and the 1064 nm NPRO. The one-sided phase noise power spectral density with and without the action of the intensity noise servo is shown in figure 4.6, which reveals $\sim$7 dB phase noise suppression out to 100 kHz and a unity-gain frequency of 700 kHz. It is disappointing that the effect of the noise servo seems to saturate at 7 dB supression. We suspect that this is due to the direct phase noise effect of ASE mentioned earlier for which the servo can have no impact in principle. On the other hand, the integrated phase noise from 700 kHz to 2 kHz (below which phase noise due to environmental perturbations dominates over that due to RIN) drops from 0.1 rad^2 to 0.027 rad^2.

The amount of phase noise suppression depends on the pump current and can be as high as 10 dB out to 300 kHz with $I/I_{th} \sim 1$. Nevertheless, for all pump current values, the absolute phase noise spectrum and the unity gain frequency achieved with the servo is essentially the same after adjustments to the loop filter. The noise peaking past the unity-gain frequency present in both intensity and phase noise spectra leads to an additional integrated phase noise of 0.008 rad^2 above 1 MHz. However, this noise is not very important for our femtosecond enhancement cavity since it is well above our resonance width and mostly attenuated by the low-pass action of the cavity.

By using the amplitude noise servo, the phase noise of our frequency comb is supressed and therefore the lock to the enhancement cavity also becomes significantly quieter. The supression of amplitude noise in our cavity is shown in figure 4.7 which demonstrates that this is also a useful tool for increasing the coherence of our harmonic XUV frequency combs [97].

4.3   Measurement of the seventh harmonic temporal coherence

To determine the temporal coherence of a radiation source, one must compare it to something which has a similarly narrow spectral feature. This could be an optical cavity, an atom or molecule, or another radiation source. All of these possibilities are met with

difficulty in the XUV. It is impossible to build a high finesse cavity because of the very high absorption in solid materials at XUV wavelengths. Spectroscopic measurements are also difficult because of the Doppler width of the transitions ($\delta\nu \approx v/\lambda$ where now λ is an order of magnitude smaller than in the visible) and many Doppler-free spectroscopic techniques require more power than we have available. To compare with another radiation source we would effectively have to build two intracavity HHG systems (although difficult, we intend to perform this experiment in the near future).

Early in the development of high repetition-rate intracavity HHG, there were two tests of the temporal coherence of intracavity third harmonic generation [33, 34]. In this case, the third harmonic could be generated in nonlinear crystals in addition to inside the enhancement cavity. The beatnote between these two frequency combs revealed that a high level of coherence was maintained in the intracavity harmonic process with a $\sim$1 Hz resolution bandwidth limited beatnote. On the one hand, the third harmonic is certainly not a high harmonic and so clearly more tests on higher-order harmonics are necessary. However, the cavity and intracavity plasma can add decoherence to the generated harmonics as discussed above and these effects do not differentiate between the harmonic orders except in the magnitude of the effects. Therefore, these tests were important steps forward in confirming the coherence of the frequency comb generated through intracavity HHG.

As previously discussed, the mechanism for harmonic generation is unique for below-threshold harmonic generation. For this reason, we decided to test the temporal coherence of the 7th harmonic in our system. This harmonic is at 153 nm and we chose this harmonic specifically because it is at the very edge of the wavelength range where it is possible to obtain conventional beamsplitters and reasonably reflective mirrors. However, no narrow linewidth lasers are available at this wavelength, so it is impossible to test the coherence with a heterodyne beatnote. For this reason, it was necessary to conduct a coherence test by comparing the 7th harmonic radiation to itself through a self-homodyne beatnote.

In a self-homodyne beatnote, one compares the output of a laser to a time delayed

version of itself (for a rigorous analysis of this technique see [98]). If the time delay is very long then we can assume that the two fields we are comparing have uncorrelated noise. In this limit the test is no different from comparing two similar lasers through a heterodyne beatnote and the linewidth of the beatnote should about $\sqrt{2}$ times larger than the actual laser linewidth. However, this measurement is fraught with difficulties because, for the homodyne beatnote to be sensitive to a phase noise process at Fourier frequency f_1, the delay line must be at least c/f_1 long, where c is the speed of light. In this case, noise at Fourier frequency $f < f_1$ is still correlated in the two optical fields. Since, most real lasers have frequency noise processes that grow at least as fast as f^{-1} at low frequencies, it is hard to argue that one has made a long enough delay line to observe all the relevent phase noise that can contribute to the linewidth. Further, to build a homodyne beatnote experiment sensitive to noise above 10 kHz Fourier frequency will still require a delay line of 30,000 meters, which is quite impossible in the XUV (but possible in the near IR with optical fiber).

Instead of using delay lines of very long length, we can design an experiment in the other extreme and use a delay line which is so short that we can assume that there are no noise processes that occur on a shorter time scale than the temporal delay. It is certainly more reasonable on physical grounds to assume that phase noise will decrease at high-Fourier frequencies. In this case the interference signal in the homodyne beatnote is

$$I(t) = \left| A_1 e^{i[\omega t + \phi(t)]} + A_2 e^{i[\omega(t+\tau) + \phi(t+\tau)]} \right|^2, \tag{4.9}$$

$$\Rightarrow I(t) = A_1^2 + A_2^2 + 2A_1 A_2 \cos\left[\omega\tau + \phi(t+\tau) - \phi(t)\right]. \tag{4.10}$$

If we adjust our delay time precisely so that $\omega\tau = \pi/2 + 2\pi p$ then the time dependent part of equation 4.10 is proportional to

$$\sin\left[\phi(t+\tau) - \phi(t)\right] \approx \phi(t+\tau) - \phi(t) \approx \tau \frac{d\phi(t)}{dt}, \tag{4.11}$$

where we take the limit that τ is very small along with the definition of the derivative to obtain the final result. This shows that with the pulse delay set correctly (in "phase-quadrature") the intensity signal in a homodyne beatnote is proportional to the frequency

noise, $d\phi(t)/dt$, of the laser. Note that the sensitivity to frequency noise is proportional to the delay time, τ. Since, τ is assumed to be very small, usually the signal to noise must be very high to make a good measurement of the frequency noise.

It is very difficult to build a VUV delay line longer than a few meters because this line must be in vacuum and the reflectivity of mirrors at 153 nm is only $\sim 80\%$. Therefore our delay line was about 2 meters long ($\tau = 7$ ns). This is a rather short delay length so equation 4.11 provides a valid description for the analysis of the signal. Since we have a VUV frequency comb and not a cw laser, the delay time must be set precisely to the repetition period so that two subsequent pulses in the pulse train interfere with each other.

For this study, the harmonic radiation was roughly collimated and sent through a cross-correlation interferometer with a delay set so that a pulse in the harmonic train will interfere with the subsequent pulse, allowing us to measure the degree of pulse-to-pulse coherence. This setup is shown in figure 4.8. As the 7th harmonic radiation is absorbed in air, all the necessary optical alignments had to be conducted under vacuum. A MgF_2 beam splitter, CaF_2 lenses and aluminium mirrors optimized for operation in the vacuum-ultraviolet were used for the construction of the interferometer. As the reflectivity of the MgF_2 beam splitter was only due to the Fresnel reflection (0.09 for 152 nm light and s polarization), the ratio of power in the two arms was ≈ 0.12. One end-mirror of the interferometer was mounted on a piezoelectric transducer so that the optical delay of the interferometer could be scanned. To detect radiation at the output port, we used a conventional photomultiplier tube with a thin layer of sodium salicylate on the front surface (sodium salicylate fluoresces at ≈ 420 nm when excited by VUV radiation that matches very well with the peak in sensitivity of the photomultiplier tube). Since the 7th harmonic is outcoupled off of the intracavity diffraction grating, there is spatial dispersion as well as intrinsic astigmatism which produce minor effects over short distances but become quite noticeable over the two meter length of the interferometer. We modeled these effects and estimated that the ultimate contrast obtainable within the interferometer was about 10%-15%, assuming a perfect alignment.
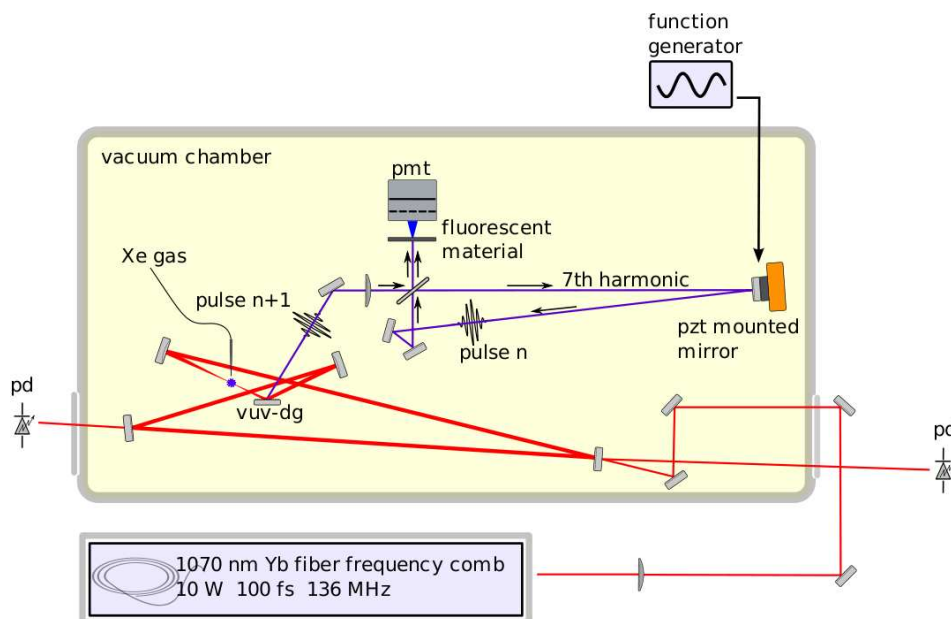
Figure 4.8: Experimental set-up for the demonstration of vacuum-ultraviolet pulse-to-pulse coherence. The diffraction grating output coupling method (VUV-dg) is used to outcouple the seventh-harmonic radiation, which is then sent through a cross-correlation interferometer. One mirror in the delay arm of the interferometer is mounted on a PZT, allowing scans of the differential path length. This PZT is also modulated at 392 kHz to provide a lock-in signal of the homodyne beatnote. The seventh-harmonic radiation at the output of the interferometer is detected by monitoring the fluorescence from a sodium-salicylate-coated plate with a PMT.
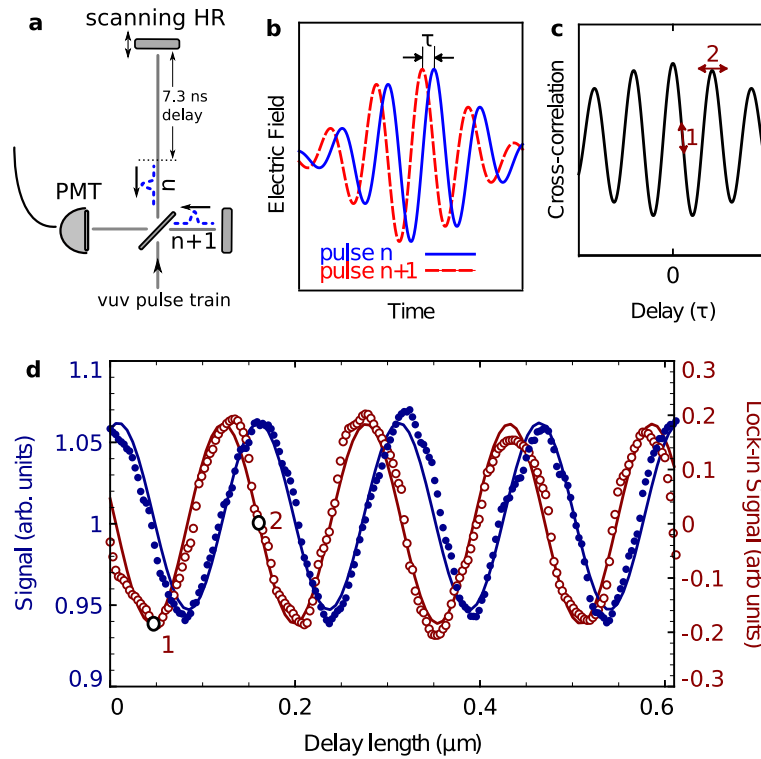
Figure 4.9: Seventh-harmonic pulse-to-pulse coherence measurement. a) Pulse-to-pulse measurement set-up. b) The electric field of pulse n interfering with the n + 1 pulse in the train. c) A cross-correlation signal results as the length of the delay line is scanned. d) The blue filled circles show our experimental measurement of the cross-correlation as the path length of the interferometer is linearly scanned. The red open circles show the signal achieved from a lock-in detection of a 392 kHz modulation of the delay line. Point 1 in c) and d) shows the positions of a maximum negative lock-in signal where the cross-correlation signal at dc has a maximum negative slope. Point 2 shows the position of a zero lock-in signal with the dc cross-correlation at its maximum.

Figure 4.9 shows the interference signal as the path length of the interferometer was scanned over 600 nm in about 2 s. The contrast ratio in the interference fringe shown is $\approx 6\%$. The coherence time of a source is defined as the time delay required for the fringe contrast to drop to 50% of the maximum. Given our estimate of the maximum contrast achievable in this interferometer, this would lead to a coherence time of ~ 10 ns. Given the likely possibility that the pulse overlap and interferometer alignment were not perfect, the ~ 10 ns should only be considered a lower bound of the source coherence time.

To provide a zero background for a significantly enhanced measurement contrast, we also used a lock-in detection by dithering the length of the interferometer at 392 kHz as the length of the interferometer was scanned. The demodulated signal is also shown in figure 4.9. This signal was also useful in that it allowed us to adjust the overlapped pulses to be in phase quadrature and measure the resulting frequency noise on an rf spectrum analyzer according to equation 4.11. The noise level measured in this manner was consistent with the shot-noise given the dc level on the detector. Therefore, this measurement did not reveal the actual noise on the XUV frequency comb but it still provided an upper bound on our frequency noise of $PSD_f \approx 15$ MHz. This places essentially the same lower bound on the coherence time as the contrast measurements if we assume that the frequency noise in our system is truly a constant as a function of frequency (i.e. our linewidth is Lorentzian). The lower bound coherence time shows that there will be frequency comb structure in the VUV frequency comb since any reasonable functional form for the frequency noise will produce a linewidth well below our repetition period.

Given our estimates of the expected noise processes at the beginning of the chapter, we would expect any frequency noise to fall significantly below the upper bound we set experimentally with this test. For instance, it is clear from the phase noise of our laser shown in figure 4.6 that there is not much noise in our system past 100 kHz. For this noise to broaden our comb linewidth to 10 MHz would require phase modulation of ~ 100 rad. No noise process that we have estimated could potentially offer that magnitude of phase

modulation. Still, we can refer back to the initial description of high harmonic generation in Chapter 1. It is easy to assume that the process is so violent that some unaccounted process will ultimately destroy the coherence even at the ~ 10 MHz level. Therefore, the 7th harmonic experiment revealed that nothing catastrophic is occuring in the process and the pulse-to-pulse phase coherence for low-order harmonics should at least be sufficient for a certain class of experiments (the measurement of transitions with ~ 10 MHz natural linewidths for instance), and could potentially be much better [90].

At the time of these coherence tests, the power of this frequency comb was still too low to perform a real world spectroscopic measurement (only ~ 100 nW per harmonic) and the coherence had not been tested even at the ~ 10 MHz level for above threshold harmonics into the XUV spectral region. The next two chapters will discuss how we increased the power in the frequency comb to a useable level and then used this source for a spectroscopic measurement in the XUV.

Chapter 5

Power scaling and plasma nonlinearities

Intracavity HHG systems have the potential to produce record-setting levels of high harmonic flux if one obtains conversion efficiencies similar to what is obtained in single-pass systems. However, difficulties intrinsic to the enhancement cavity have presented challenges in this regard. Increasing the XUV flux of our system is quite important since, as discussed in Chapter 1, high resolution DFCS will almost certainly be limited by low photon flux. Here we outline some of the most prominent difficulties in increasing the XUV flux of an intracavity HHG source and demonstrate a system that mitigates or overcomes many of these issues.

Originally, harmonic flux through femtosecond enhancement cavities was limited by mirror damage, nonlinearities intrinsic to the cavity optics (i.e. the Brewster plate output coupler used for the first demonstrations [33, 34]), and the power of the frequency comb exciting the enhancement cavity. Previous chapters have described how many of these challenges have been overcome with the exception of mirror damage. While mirror damage was once a major limitation of the intracavity technique, high damage-threshold mirror designs have improved dramatically in recent years and now damage occurs only very infrequently (although mirror contamination with cracked hydrocarbons is still problematic as will be discussed later in the chapter) [99]. These advances helped us increase the average power inside of our enhancement cavity to ~ 10 kW as opposed to the ~ 400 W which was shown in the first demonstration from our group of intracavity HHG [33]. However, with this increased

intracavity power, it became apparent that the effects of the laser generated plasma could also produce a nonlinear response in the enhancement cavity. Since the plasma is intrinsic to the HHG process, mitigating these nonlinear effects is now one of the main challenge to increasing the XUV flux generated by our system.

5.1   Plasma nonlinearities

The harmonic flux generated in a given HHG system will increase quadratically with the density of target atoms in the interaction region. Therefore, it seems advantageous to increase the target gas density as much as possible. However, at some point the density will become large enough that harmonic radiation generated at the front of target will be completely absorbed by the end of the target and the flux will saturate as a function gas density. Therefore, to optimize high harmonic flux, it makes sense to increase the gas density but not past the point where the length of the gas target is longer than a few absorption lengths (a condition known as the "absorption limit" [61]). If we achieve this optimal gas density at our intracavity focus and ionize a significant fraction of the target gas with every pass of the intracavity pulse, the laser-generated plasma can reach a level such that a significant phase-shift of the fundamental radiation occurs. This phase-shift can affect our ability to effectively couple our excitation frequency comb to the enhancement cavity resonances and introduce phase-matching difficulties.

We estimate that for the studies presented here, the free electron density can approach $\approx 10^{17} \ cm^{-3}$, which over the length of the medium can produce a significant round trip phase shift of $\sim$0.1 rad. Complicating the problem is that, for a high-repetition rate system, the intracavity pulse will interact with a given electron in the plasma several times before that electron dissipates out of the interaction region. A reasonable rate for plasma dissipation shows that the electron will be present in the interaction region for 5-10 pulses [100]. At the same time, when a single pulse propagates through the interaction region, the plasma density increases very quickly over just tens of femtoseconds. Therefore there are effectively

two different contributions to the plasma density which in turn present their own unique challenges; a steady-state density which persists from pulse to pulse and a density that increases rapidly over the duration of the pulse [101, 102].

5.1.1   Steady state plasma density

One consequence of the plasma density that persists from pulse to pulse is to create an instability in the frequency lock of the excitation laser to the buildup cavity. This instability can be understood by considering how the relationship between laser frequency and detuning from the resonance is modified by the addition of a plasma and is illustrated in figure 5.1. The intracavity power as a function of detuning from the cavity resonance is illustrated by the blue curve in figure 5.1a and essentially represents a Lorentzian function close to the resonance. With the addition of target gas, plasma whose density depends nonlinearly on the intracavity power will create a shift in the absolute frequency of the cavity resonance as shown by the dotted green curve in figure 5.1a. This detuning-dependent frequency shift modifies the trivial linear relationship between laser frequency and resonant detuning as shown in figure 5.1b. This is a manifestation of optical bistability as the portion of the curve with the negative slope (the dotted green line in part b) is unstable as can be confirmed with a linear stability analysis [103].

In a typical frequency lock that aims to minimize the comb detuning from the resonance, the cavity will lock very close to the unstable branch (point 1 in figure 5.1b). Small residual frequency error can push the system to the unstable branch after which the system will jump to point 2 in figure 5.1b. The frequency lock will correct this sudden error moving the system through points 2-4 and eventually arriving back at point 1. As this process repeats, oscillations in the system will occur. While the plasma itself will respond to perturbations on a timescale of 10 ns, the cavity lock can only respond on a timescale of about 10 μs. Therefore, the oscillations observed in figure 5.1 are limited by the slower time scale and at a frequency of about 50 kHz. The system becomes more stable to frequency error if
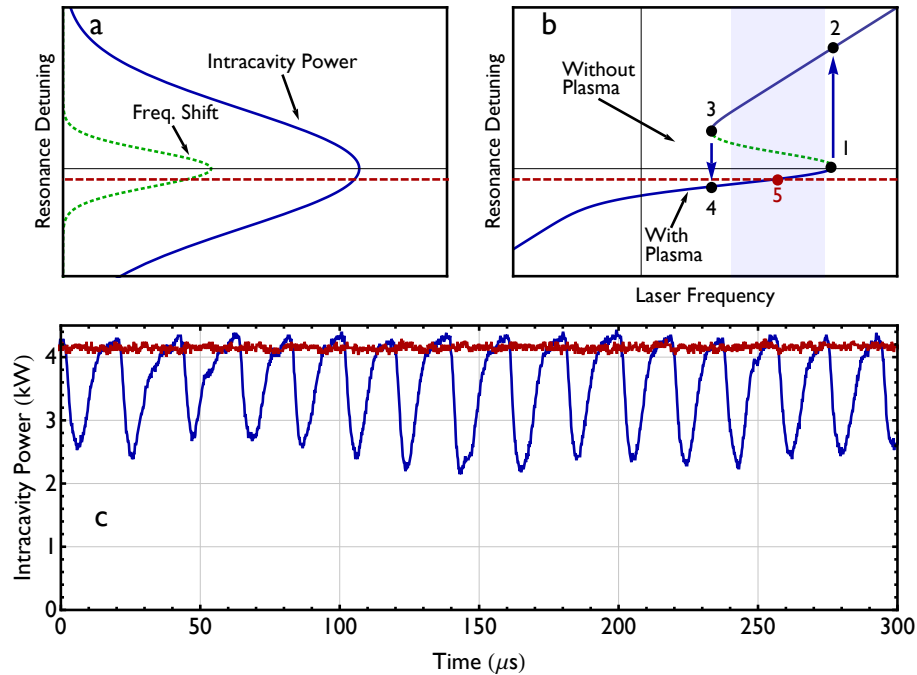
Figure 5.1: a) Diagram showing both the intracavity power as a function of resonance detuning (blue curve), as well as the frequency shift in the resonance position due to plasma (dotted green curve). b) Diagram showing the detuning from the resonance as a function of the laser frequency with the shift in the resonance position shown in a) added to the otherwise linear relationship. c) Intracavity power as a function of time with an offset of the locking position from the resonance (red curve) and without an offset (blue curve). With zero offset from the resonance, the system will lock to point 1 on b). Slight laser noise at this position will cause the system to jump to point 2. The lock will then adjust the laser frequency to minimize the detuning from the resonance, moving quickly through points 2-4 on the diagram. This cycle repeats creating characteristic oscillations as shown on the blue curve in c). By adjusting the lock so that the laser is detuned from the resonance by $\approx 1/6$ the cavity resonance width, the system locks at point 5. This position is stable against frequency noise as represented by the gray box in b) and results in elimination of the oscillations as shown in the red curve in c).

we force the laser to lock to the cavity with a slight detuning from the resonance as shown by the dashed red line in figure 5.1b. We have found that offsetting the locking point from the resonance by $\approx 1/6$ the resonance width results in a stable frequency lock.

From these results, we can also make a connection back to the discussion in Chapter 4 regarding the effect that this plasma has on the conversion of phase noise to amplitude noise within the cavity. If we detune the cavity from the peak of the resonance as described above, the cavity is effectively in a self-locking regime where a given frequency excursion of the excitation laser produces a smaller amplitude fluctuation than would occur in a cavity with no plasma. So rather than being a detriment, the phase-shift of the plasma can actually lead to less amplitude noise within the enhancement cavity.

Another effect of the steady state plasma is that we can begin to deplete the neutral gas leaving only plasma in the interaction region. In our high repetition rate system this effect is exacerbated since $\sim 1/5$ of this plasma will disipate and be replaced by neutral gas before the next pulse in the pulse train arrives. In practice, the effects of phase matching will begin to limit our harmonic generation sooner than neutral depletion since optimum phase matching occurs with only $\approx 10\%$ ionization [61]. Therefore, any technique that could remove residual plasma from the interaction region faster would allow for more single pass ionization with optimized phase matching and therefore could increase the XUV photon flux. Another option is to decrease the repetition rate by a factor of $\sim$3-10 in which case the effects of the residual plasma will not produce much additional disadvantage as compared with a single pass system (as in [104, 105]). However, for XUV-DFCS, lowering the repetition rate is not ideal as previously discussed in the introduction on frequency combs. For this reason we choose to keep our repetition frequency at 154 MHz. We studied the dependence of the harmonic power as a function intracavity power as shown in figure 5.2. Note that there are only modest improvements in power for most harmonics as the intracavity power is increased from 5.5 to 6.5 kW due in part to a decrease in phase matching as plasma density increases and also to a depletion of the on-axis neutral atom density available for HHG.
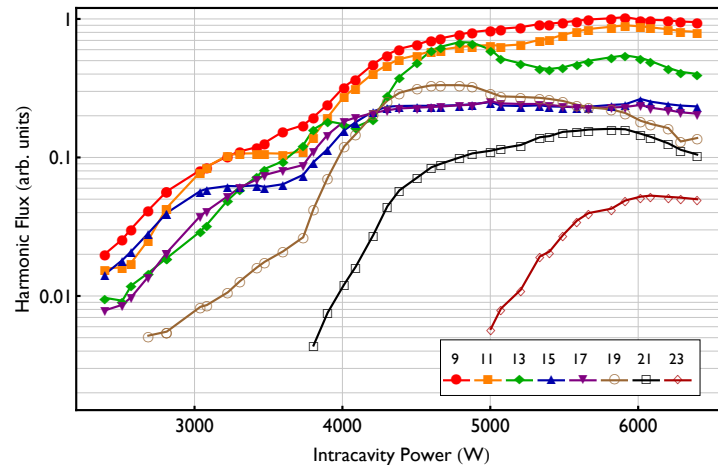
Figure 5.2: Harmonic flux plotted as a function of intracavity power for all harmonics showing a marginal increase in harmonic power for intracavity powers between 5.5 and 6.5 kW.

5.1.2   Plasma variations on the femtosecond timescale

The second challenge presented by the intracavity plasma arises from the portion of the plasma density with dynamics on the femtosecond time scale, which has recently been studied in [101, 102]. This effect results in a phase shift that varies over the duration of the intracavity pulse so that it is impossible to maintain constructive interference between the intracavity pulse and pulse exciting the cavity over the whole pulse duration. As a result, the intracavity pulse and corresponding spectrum become distorted. The intracavity power can clamp to a lower value than is achieved in a cavity without a plasma. While self-phase modulation resulting in blue-shifting of the spectrum has been seen in single-pass harmonic generation experiments, the effect observed in an enhancement cavity is distinct as it is magnified by the finesse of the cavity.

We can increase the tolerance of the system to phase mismatch between the intracavity pulse and the driving pulse train by lowering the cavity finesse. This decrease in phase sensitivity is evident when one considers that the cavity power enhancement is proportional to

$$\frac{1}{1 + \left(\frac{2\mathcal{F}}{\pi}\right)^2 \sin^2\left(\phi(t)\right)}, \tag{5.1}$$

where $\mathcal{F}$ is the cavity finesse and $\phi(t)$ is the roundtrip phase error which varies over the duration of the pulse. Since the phase error is effectively multiplied by the finesse, a robust method of mitigating the effects of a temporally varying plasma is obtained by decreasing the finesse. While lower cavity finesse significantly decreases the effects of intracavity pulse distortion, it also requires a more powerful laser to excite the enhancement cavity so that the intracavity pulse energy remains high. To excite the cavity, we require a relatively large pulse energy of ≈ 200 nJ in the external pulse train that is easily provided by the Yb fiber frequency comb described in Chapter 3.

To demonstrate the decrease in spectral distortion due to lowering the finesse we compare the performance of our system with two input couplers with different transmissions
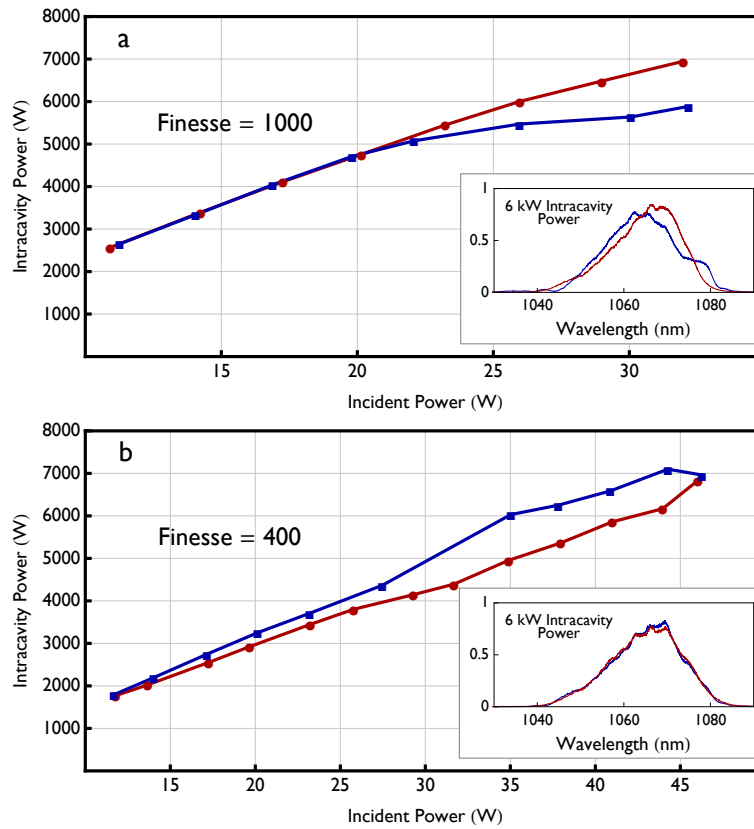
Figure 5.3: a) Intracavity power as a function of incident power for a cavity with $\mathcal{F} \approx 1000$ for both an empty optical cavity (red circles) and an optical cavity where xenon gas was injected at the focus with a 100 μm nozzle with 1.5 atm of backing pressure (blue squares). b) Same as in a) but with $\mathcal{F} \approx 400$. The insets show the intracavity spectrum at a representative power of 6 kW for the respective cases. Spectral distortion is clearly visible in the higher finesse cavity when intracavity plasma is present. The nozzle position with respect to the focus was identical in both cases. The mismatch in the buildup for the low finesse case is due to imperfect transverse mode matching. For the $\mathcal{F} \approx 400$ cavity, the power begins to clamp at 7 kW of intracavity power when xenon is used as the target gas.

while keeping all other parameters identical. A comparison of the intracavity spectrum and intracavity power as a function of incident power is shown in figure 5.3. Results are shown both with a target gas injected (with a 100 μm diameter nozzle and a backing pressure of 1.5 atm) and for no target gas. When comparing the cavities with no intracavity gas target, both cavities respond linearly with an undistorted spectrum. However, the advantage of the lower finesse cavity is clearly observed when a gas target is added at the intracavity focus. At 6 kW of average power the intracavity spectrum of the higher finesse cavity becomes distorted and the intracavity power begins to clamp while the lower finesse cavity maintains an undistorted spectrum and can still reach > 7 kW of average power.

5.1.3   Effects of the plasma on the transverse spatial mode

The effects we have discussed thus far consider the plasma to be a spatially uniform medium. This is an approximation as the plasma will be generated more rapidly at the center of the focused Gaussian beam than at points off axis. To include these effects requires a full four-dimensional model (three spatial and one time) and is very computationally intensive. Therefore, to gain intuition for how the addition of the transverse spatial effects can affect our system, here we consider a model that takes into account the two transverse dimensions but ignores the fast variations of plasma density that could occur over the duration of the pulse.

We simplify the problem further by considering a cylindrically symmetric cavity so that the spatial mode can be described in terms of a single radial coordinate, r. Variations of the mode in the polar angle θ are ignored because we assume that the generated plasma only varies in r and therefore there is nothing in the problem capable of breaking symmetry in the θ dimension. In our actual experimental setup, this symmetry is broken because of the angle of the beam on the curved mirrors and because the gas is injected from above the beam, but the qualitative result remains valid.

We implement the model by decomposing the intracavity beam into the Laguerre-
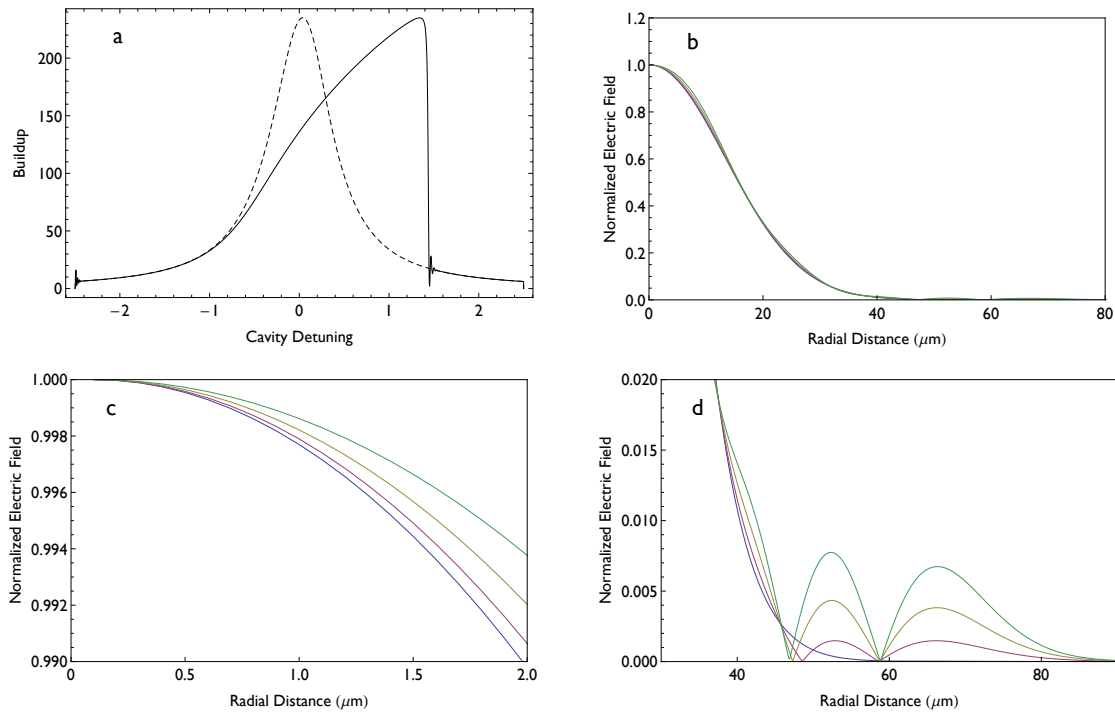
Figure 5.4: Plot showing the radial mode distortion due to the intracavity plasma. a) Buildup as a function of laser detuning for no plasma (dashed line) and with plasma at the beam focus (solid line). The self-locking effect observed can be understood from figure 5.1. b)-d) show the radial mode profiles for different plot ranges at four different positions of laser detuning. These laser detunings correspond to the laser detuning values of -1.3 (blue curve), 0 (red curve), 0.6 (yellow curve) and 1.4 (green curve) as shown in a).

Gaussian transverse normal modes $L_{\rho l}(r,\theta)$ where ρ and l are integers giving the radial and angular mode orders, respectively [46]. With the symmetry discussed above, the expansion proceeds just in terms of the $l = 0$ modes for which there is no θ variation.

$$E_{tr}(r) = \sum_{\rho} c_{\rho} \, L_{\rho,0}(r). \tag{5.2}$$

Propagation around the cavity is fairly simple with this formalism. The algorithm for propagation through the cavity proceeds as follows: 1) every coefficient, c_{ρ} is multiplied by the field loss of the cavity every round trip; 2) We assume that we are coupling our excitation laser perfectly to the $L_{0,0}$ mode so we add the excitation field only to the complex c_0 coefficient; 3) The coefficients, c_{ρ}, receive a phase shift given by

$$\phi_{\rho} = (1 + 2\rho)\tan^{-1}\left(-\frac{\text{Im}[A + B/q]}{\text{Re}[A + B/q]}\right), \tag{5.3}$$

which is essentially a generalized Gouy shift where A and B are defined from the ABCD matrix of the cavity [46]. Without some mechanism to couple power between the c_{ρ} coefficients, only the c_0 coefficient will be non-zero and this will simply describe the enhancement cavity power buildup that is obtained by completely ignoring the transverse mode. However, if we introduce a power dependent plasma, coupling between the c_{ρ} coefficients will occur every round trip.

At the focus we can calculate the radially varying intensity through equation 5.2. We can then include a plasma whose density is nonlinearly related to this intensity (for this model, we approximate an I^5 dependence), which produces an r-dependent phase shift. After this phase shift has been added to the spatial profile of the beam, we expand the electric field in terms of the c_{ρ} coefficients once again so that we can propagate through the cavity. The simulation consists of repeating this process once for every round trip through the cavity and including enough round trips (determined by the cavity finesse) to achieve steady state behavior.

We perform this simulation as a function of laser detuning from the cavity resonance and the results are shown in figure 5.4a. The figure shows the power buildup when scanning
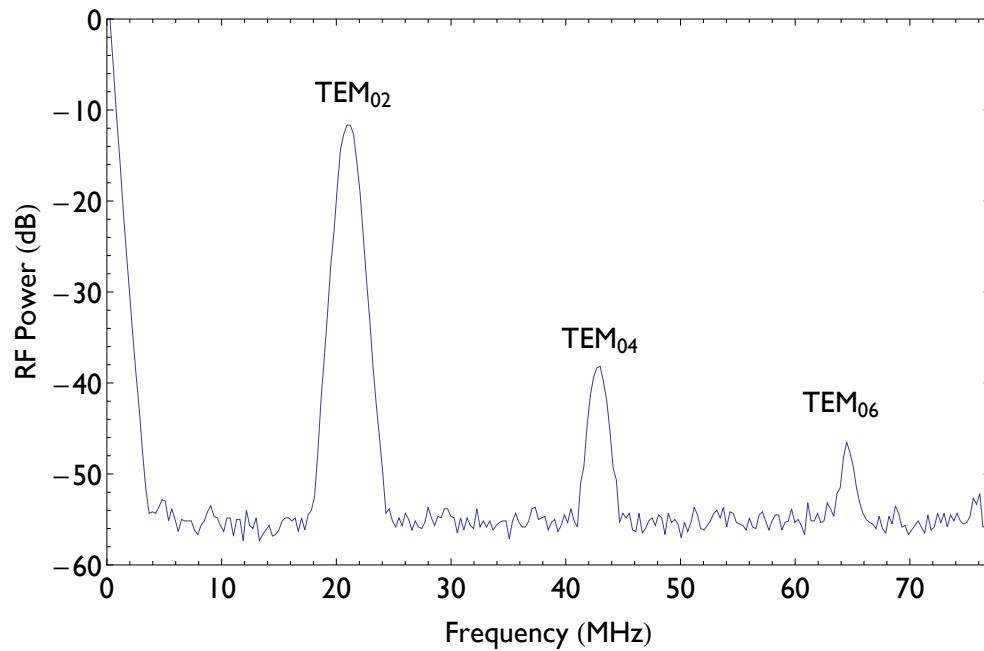
Figure 5.5: Radio frequency spectra of the intracavity power signal with 1 MHz resolution bandwidth. The rf spectral features are labeled with the higher-order modes that would produce the corresponding beat frequency with the fundamental TEM_{00} mode. This data was taken with a $\mathcal{F} = 1000$ enhancement cavity. The modulation amplitudes were observed to decrease by about 20 dB when using a $\mathcal{F} = 400$ enhancement cavity

through the cavity resonance in the absence of plasma phase shifts and when a plasma is present. The effects of self locking are clearly evident and can be understood by considering sweeping across the resonance from left to right in figure 5.1. The plasma density was increased until the self-locking effect seen in the figure 5.4 is similar to what is observed in our experiment (a shifting of the cavity resonance by ~ 3 of the unperturbed resonance widths).

The effect on the intracavity mode is seen in the figure 5.4b. It is clearly evident that the intracavity mode shape is altered. Zooming in on figure 5.4b, as shown in figures 5.4c and 5.4d displays a very distinct shape which could lead to the question of whether the higher order mode content is being dominated by just one higher order cavity mode. By comparing the mode shape from the simulation with the $L_{\rho,0}$ modes, we find that this is not the case.

While there is certainly a noticeable effect of spatial mode distortion in our simulation, it would be difficult to see this effect in the mode profile experimentally (the variations of the mode structure are somewhat subtle as can be seen in figure 5.4b). However, this effect can still be observed experimentally because the higher order modes have a different round trip phase shift as described in equation 5.3. When the intracavity plasma places optical power into these higher order modes they will interfere with the fundamental mode producing intensity fluctuations in our intracavity power with frequency $1/(2\pi)(\phi_0 - \phi_\rho)\mathrm{FSR}$ (this effect is also known as transverse mode beating [46]). We have observed these transverse mode beats in our system as shown in figure 5.5.

Since in our actual experimental setup, the symmetry between the two transverse dimensions is broken, we assign a Hermite-Gaussian mode to each of the observed rf modulation frequencies. Inspection of the cavity's higher-order mode structure indicates the modulation comes from beating between the fundamental TEM_{00} mode of the cavity with the progression of higher order modes of even symmetry in the vertical direction (labeled as such in figure 5.5). We hypothesize that mode coupling in the vertical direction is preferentially excited due to the plasma gradient in this dimension (along which the gas nozzle is aligned). This

transition to multimode operation is observed to occur abruptly as the intracavity power and gas flow are increased and occurs at conditions beyond those optimal for the best XUV photon flux (when phase matching due to the plasma has begun to severely limit the system). However, it is still important to understand and control this effect since this high frequency modulation would place unwanted sidebands on the XUV comb.

5.2 Mirror contamination

As our system began to produce increasing levels of XUV radiation, we also obtained an increase in the production of low-order harmonics. The large amount of radiation generated at the 3rd and 5th harmonic (357 nm and 214 nm) is capable of cracking hydrocarbons which are present at trace levels in our vacuum chamber. This process can contaminate mirror surfaces with the hydrocarbon constituents. The cavity mirrors in our system are relatively transmissive at these wavelengths so we believe the highest power of ultraviolet and deep ultraviolet radiation in our cavity is present at the surface of the first few mirrors encountered after the radiation is generated in the plasma. After the first few reflections from cavity optics the UV radiation is significantly attenuated.

This hypothesis is confirmed in that we have observed visible contamination of the mirror surfaces for both the grating output coupler and the first curved mirror which the UV radiation encounters after the plasma. The contamination is well localized to a spot which is somewhat smaller than the fundamental beam transverse mode. We have yet to notice visible contamination on the other mirror surfaces, which we attribute to the decreased level of UV radiation incident on those mirrors. The contamination can lead to heating on the surface of the mirrors, which can slightly warp the mirror surface producing intracavity transverse mode distortion.

Another interesting effect of the hydrocarbon contamination is that the grooves of the diffraction grating output coupler can actually become filled with these hydrocarbons. Strangely, this action of filling the grooves seems to occur uniformly over the surface of
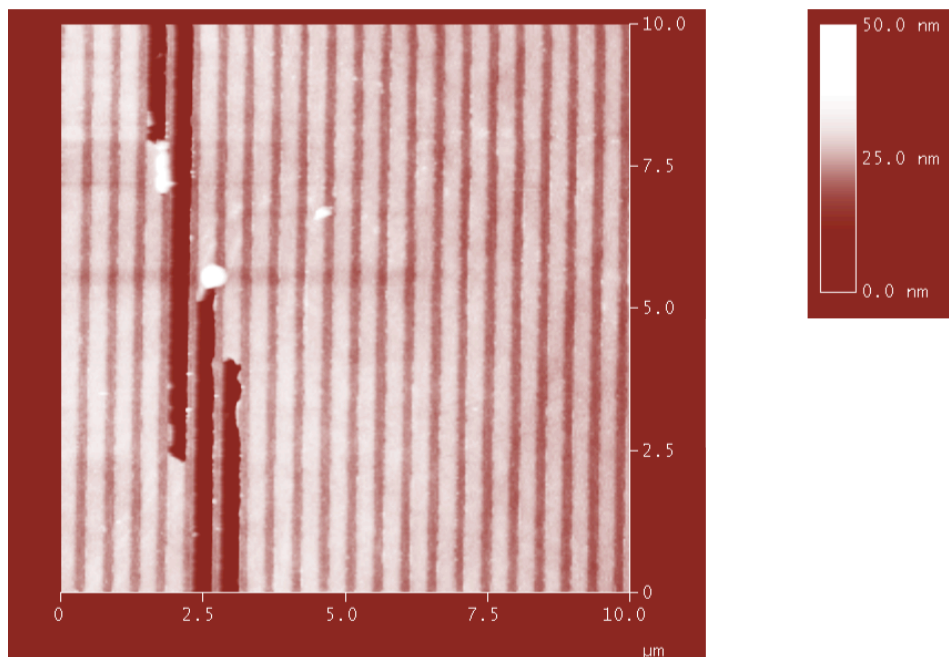
Figure 5.6: AFM image of the surface of the grating output coupler after heavy use. The grooves have been completely filled in and have even begun to mound up with hydrocarbons. By chance, a few grooves at the 2.5 μm mark have remained partially clean, which offers a good comparison.
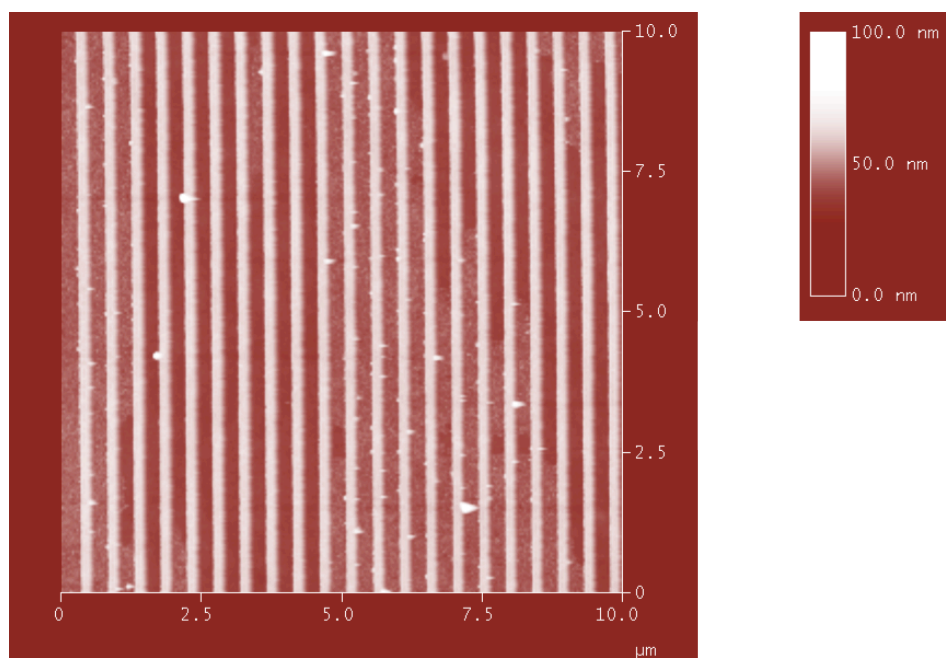
Figure 5.7: AFM image of the the same grating after being cleaned with oxygen plasma. The operation of the grating is fully restored.

the grating, unlike the contamination that is localized to the beam spot size. An image of a contaminated grating surface taken with an atomic force microscope (AFM) after heavy use within our enhancement cavity is shown in figure 5.6. The grating grooves have been so completely filled in that hydrocarbons have even begun to mound-up higher than the surface of the mirror. We first noticed this effect because the diffraction efficiency of the optic began to drop (and therefore a decrease in the output coupling efficiency of the grating) after a prolonged use of the output coupler with a large flux of XUV radiation.

By removing the optic from the cavity and exposing the surface to an oxygen plasma we can clean the hydrocarbons from the grooves and restore the grating to its initial condition as shown in figure 5.7. This process can also remove the contamination from the curved mirror surface effectively. Because this cleaning process requires removing optics from the cavity, it requires realignment of the cavity whenever mirrors become contaminated. Obviously, one solution is to diligently maintain a low level of residual hydrocarbons within the enhancement vacuum chamber. However, we were also able to clean the mirrors *in-situ* by filling the chamber with ~ 1 Torr of oxygen and operating the cavity with ~ 10 kW of average intracavity power. This produces an oxygen plasma at the intracavity focus and thus removes hydrocarbons from the mirror surface in a less invasive manner. This technique is certainly less effective than exposing the mirror surfaces to a direct oxygen plasma outside of our experimental setup. However, it would usually allow us to continue taking experimental data without major interruption in spite of hydrocarbon contamination.

5.3   Power scaling results

With the techniques described in this chapter, we were able to get significantly higher harmonic flux, as shown in figure 5.8, than we had obtained before. The 13th harmonic power was measured with an XUV photodiode (IRD Inc.), which had a coating of Indium and MgF_2 specially designed to pass the 13th harmonic while blocking higher orders and the fundamental radiation. We used this measurement to calibrate an image of all the
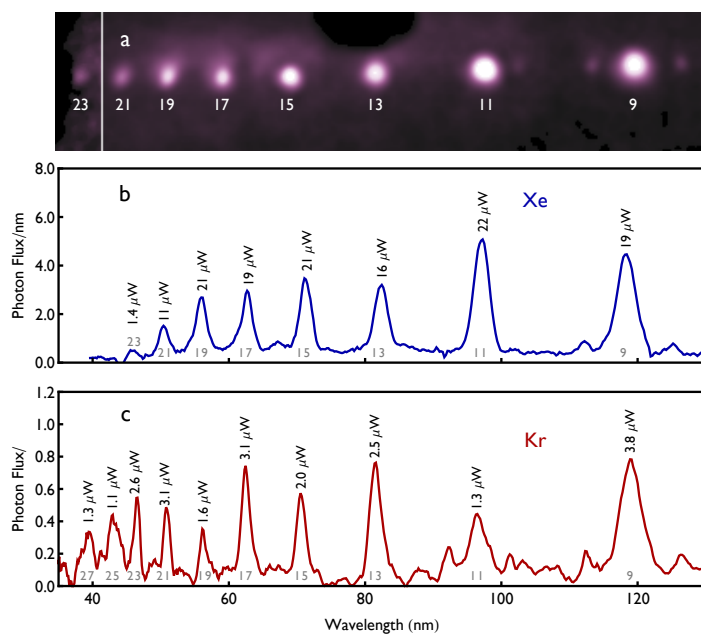
Figure 5.8: **a**. A characteristic image of the harmonics generated in xenon on a plate coated with fluorescent material. The threshold of the image was adjusted for the 23$^{\mathrm{rd}}$ harmonic to make it more visible. The measured outcoupled power as a function of wavelength for harmonics generated in **b**. xenon and **c**. krypton target gas. The observed widths of the harmonic orders are given by the instrument wavelength resolution.

harmonics fluorescing on a sodium salicylate plate. Sodium salicylate has a near uniform quantum efficiency between 40 and 100 nm so that the relative harmonic powers can be determined from these images [106]. The estimated calibration uncertainty is 20-30%. We similarly measured the harmonic power that we can generate using krypton as a target gas, which is shown in figure 5.8c. The flux obtainable with krypton is lower but the XUV cutoff extends to higher photon energy due to the higher ionization potential. As seen in the figure, with xenon as the target gas we are now able to generate more than 200 μW per harmonic and outcouple about 20 μW for spectroscopy experiments. This is a gain of ~ 100 compared to our previous results [82] and helped to enable our spectroscopy experiments to be discussed in the next chapter. To summarize, this increase is not attributable to one factor alone, but was the result of more robust cavity mirrors, a lower cavity finesse (~ 400), a more powerful excitation laser (200 nJ per pulse), an offset cavity lock to stabilize our system against oscillations, and optimized high harmonic phase-matching. It has required a detailed understanding of the nonlinear dynamics of our system and constant technical improvements to all critical components of the cavity.

Chapter 6

XUV frequency comb spectroscopy in argon

The most stringent test of the suitability of our XUV comb for DFCS is to actually conduct a spectroscopic measurement. This is important because it both requires the temporal coherence from the comb to be intact and demonstrates that the femtosecond enhancement cavity technique can generate sufficient useable XUV power for this purpose. As discussed earlier, through the HHG process, we have only 10-100 μW of average comb power per harmonic. For direct frequency comb spectroscopy of a single-photon transition, we effectively use only the power of a single comb tooth. Since the comb has $\sim$100,000 comb teeth per harmonic, each comb tooth posesses only 100 pW to 1 nW of continuous (cw) power (the actual power which is available for spectroscopy is even lower due to a few sources of loss in the optical setup). Therefore, even if the temporal coherence of our source is perfect, the low power available may make spectroscopy very difficult or impossible. Only with a very carefully designed system can the signal-to-noise of a spectroscopic measurement be tenable.

Nevertheless, in this chapter we present the excitation and detection of the $3s^23p^6$ J=0 $\Rightarrow$ $3s^23p^55d$ J=1 electric dipole (E1) transition in neutral argon at 82 nm with the 13th harmonic of our fundamental frequency comb. We were able to measure the absolute frequency of that transition with 3 MHz uncertainty, limited only by systematics involving residual Doppler shifts of the atomic source. Performing this measurement was composed of overcoming several difficulties: 1) we had to stabilize the XUV frequency comb to a calibrated frequency standard; 2) we had to produce a skimmed atomic beam to overcome

Doppler broadening limitations with sufficient atomic density; 3) our detector efficiency had to be optimized and the background scattering needed to be supressed to the level where spectroscopy was possible with only $\sim$ 10 pW of power; 4) we had to conduct the measurement at many different values of the repetition frequency to determine the frequency comb mode used to excite the transition and finally; 5) we had to carefully characterize the residual Doppler shift in our system to determine the absolute frequency of the transition.

6.1   Stabilization of the XUV comb

The most straightforward method of stabilizing a visible or near-infrared frequency comb is to lock the f_r and f_0 frequencies to calibrated rf sources. One difficulty for using this technique for high resolution DFCS is that a very small degree of phase noise on the rf source used to stabilize f_r will get multiplied by the comb mode number (since $\nu = nf_r + f_0$). For our visible frequency comb, the comb mode number is $\approx 2 \times 10^6$ so the requirement on the rf source used to lock f_r is very stringent. In practice, It is difficult to achieve a comb mode linewidth below 1 MHz when locking f_r tightly to an rf source. For our XUV comb, the situation is even more severe because the relevant mode number is about 2×10^7.

In contrast, a stable high-finesse optical cavity can posess an incredibly high quality factor. In fact, cw lasers stabilized to such cavities can now demonstrate $<$ Hz level linewidths while having carrier frequencies of several hundred THz [107]. Therefore, a good strategy to stabilize a frequency comb, which we employ for these measurements, is to lock one comb tooth to a visible or near-infrared cw laser which is itself stabilized to a high-finesse optical cavity. A conceptually simple parameterization of the frequency comb in this case is

$$\nu_0 = \nu_{YAG} + \Delta' + mf_r, \tag{6.1}$$

where ν_{YAG} is the reference laser and Δ' is an rf offset frequency present when stabilizing the comb mode through a heterodyne beatnote. This form is exactly equivalent to our normal definition of the frequency comb in terms of f_0 and f_r except now f_0 has been replaced by

the quantity $\nu_{YAG} + \Delta'$, and m is orders of magnitude smaller than n for the comb teeth of interest. Therefore the large multiplication of rf phase noise by the mode number has been significantly reduced. If our comb is parameterized by equation 6.1 and we are keeping Δ' constant through the use of a feedback loop, then adjusting the repetition frequency will result in a breathing motion with a fixed point $(\nu_{YAG} + \Delta')$ within the optical bandwidth. For this fixed point there is an associated fixed comb tooth with comb tooth number n_{YAG}. Therefore, neither f_r or f_0 is fully stable but only the combination $n_{YAG}f_r + f_0$. This constrains the frequency comb in such a fashion that $\delta f_r = -\delta f_0/n_{YAG}$, where δf_r and δf_0 represent drifts in f_r and f_0 respectively. Therefore, the remaining drift in the frequency comb can be determined by measuring either f_r or f_0.

Given the definition of our fundamental frequency comb as given in equation 6.1, the comb obtained by the 13th harmonic of our fundamental comb can be written as

$$\nu_{13} = 13 \times \nu_{YAG} + \Delta + mf_r, \tag{6.2}$$

where $\Delta = \text{Remainder}[13 \times \Delta'/f_r]$. It is this harmonic frequency comb that we will use for spectroscopy since the 13th harmonic of our fundamental frequency comb (≈ 82 nm) overlaps with the transition of interest.

The cavity stabilized laser we utilize to reference our near IR frequency comb (ν_{YAG}) is provided to us by Dr. John Hall. It is maintained in the JILA quiet room and delivered to our setup via an optical fiber. The laser is an Nd:YAG NPRO (non-planar ring oscillator) locked to a stable reference cavity. The laser output is at 1064 nm which overlaps with bandwidth from the high-power excitation frequency comb so that frequency comparisons between the two sources are easy to implement. A simplified stabilization setup for the NPRO laser is shown in figure 6.1. The lock to the stable reference cavity provides a very low phase noise source with an absolute linewidth of ~ 1 kHz. The absolute frequency of the NPRO (called NPRO 1 in the figure) is found by conducting a heterodyne beatnote with another a similar laser (called NPRO 2 in the figure) referenced to a molecular iodine

transition.

To accomplish the reference of the second Nd:YAG (NPRO 2) laser to an absolute frequency standard, the laser is frequency doubled in an enhancement cavity and locked to the a_{10} component of the R(56) 32-0 transition in $^{127}I_2$ ($\nu_{a10} = 563, 260, 223, 514$ kHz) through saturated absorption spectroscopy in an iodine cell [108]. The pump beam for the saturated absorption spectroscopy setup is shifted by 80 MHz with an acousto-optic modulator (AOM) before being sent to the cell. Since the pump and probe beam are not at the same frequency, this results in the Doppler free absorption signal being due not to the zero velocity class molecules but the velocity class which is Doppler shifted by 40 MHz.

The heterodyne beatnote between the two NPROs is at roughly 840 MHz and is extremely stable day to day (520 Hz of drift per day). Nevertheless, we monitor the beatnote continuously during our experiment to obtain an exact frequency marker. Through this process the uncertainty in the absolute frequency of the cavity stabilized laser is only 5 kHz, limited by residual amplitude modulation. In the end the frequency of NPRO 1 is given by

$$\nu_{YAG} = \frac{1}{2}(\nu_{a10} - \frac{f_{AOM}}{2} + f_{beat}) = \frac{1}{2}(\nu_{a10} - 40 \text{ MHz} + 840 \text{ MHz}). \qquad (6.3)$$

Any errors in the absolute frequency of this reference will impact the absolute frequency determinations in the XUV so it is imperative that the value is correct. It is relatively easy to make a sign error in equation 6.3, so we checked our frequency calculation by measuring the frequency of the NPRO with a Ti:Sapp frequency comb which has spectral overlap at 1064 nm when broadened, which confirmed our determined value of ν_{YAG}.

To implement the stabilization of one comb tooth of our high-power excitation frequency comb to the stable cw laser (NPRO 1), we sample the frequency comb radiation before the power amplifier and perform a heterodyne beatnote with the NPRO. We compare this beatnote to a frequency reference, Δ', with a digital phase/frequency detector and feed the error signal to the laser oscillator cavity length with the fast transducer described in Chapter 3. We are able to scan our laser frequency by adjusting the rf frequency Δ'. The
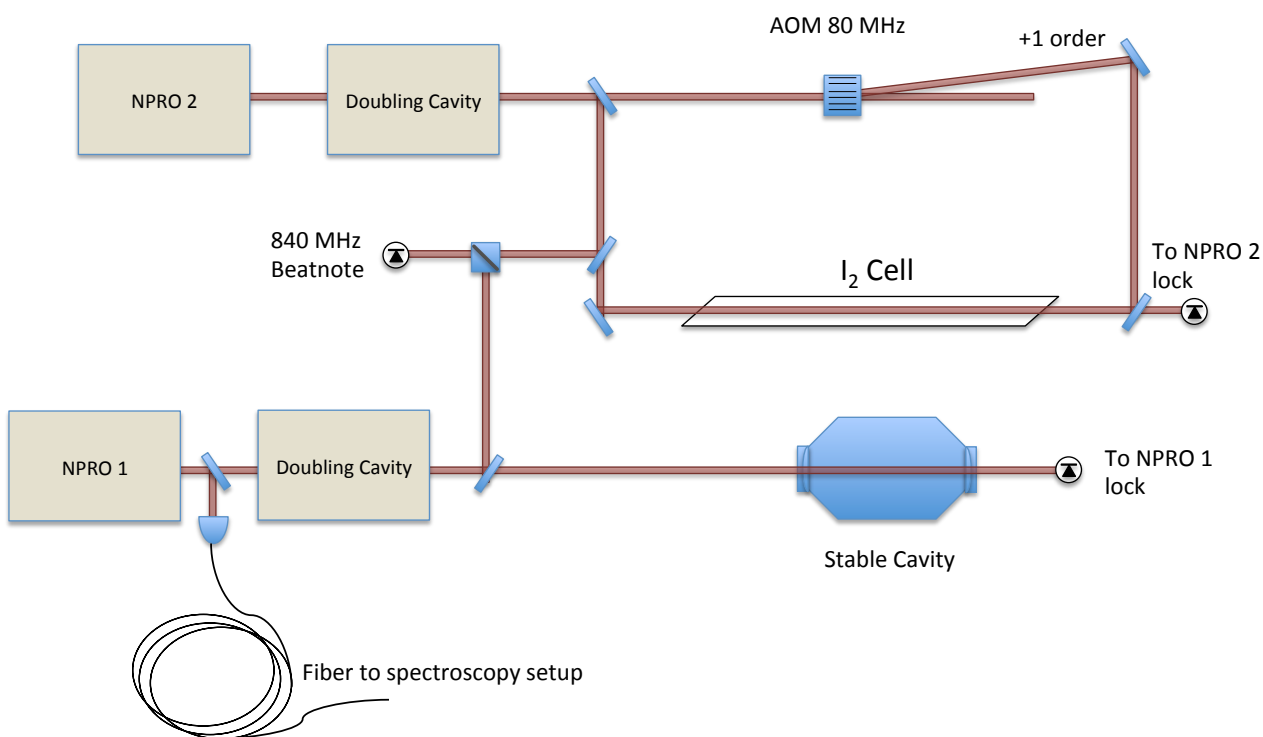
Figure 6.1: Stabilization setup for the NPRO lasers which provides our frequency comb with an absolute optical frequency marker. The cavity stabilized laser has very low phase noise (~ 1 Hz level linewidth). The iodine stabilized Nd:YAG laser (NPRO 2) is locked to the R(56) 32-0 transition in $^{127}\text{I}_2$ ($\nu_{a10} = 563,260,223,514$ kHz). The cavity stabilized Nd:YAG (NPRO 1) is compared to the I_2 stabilized laser and also sent to our setup in an adjacent laboratory via an optical fiber.

125
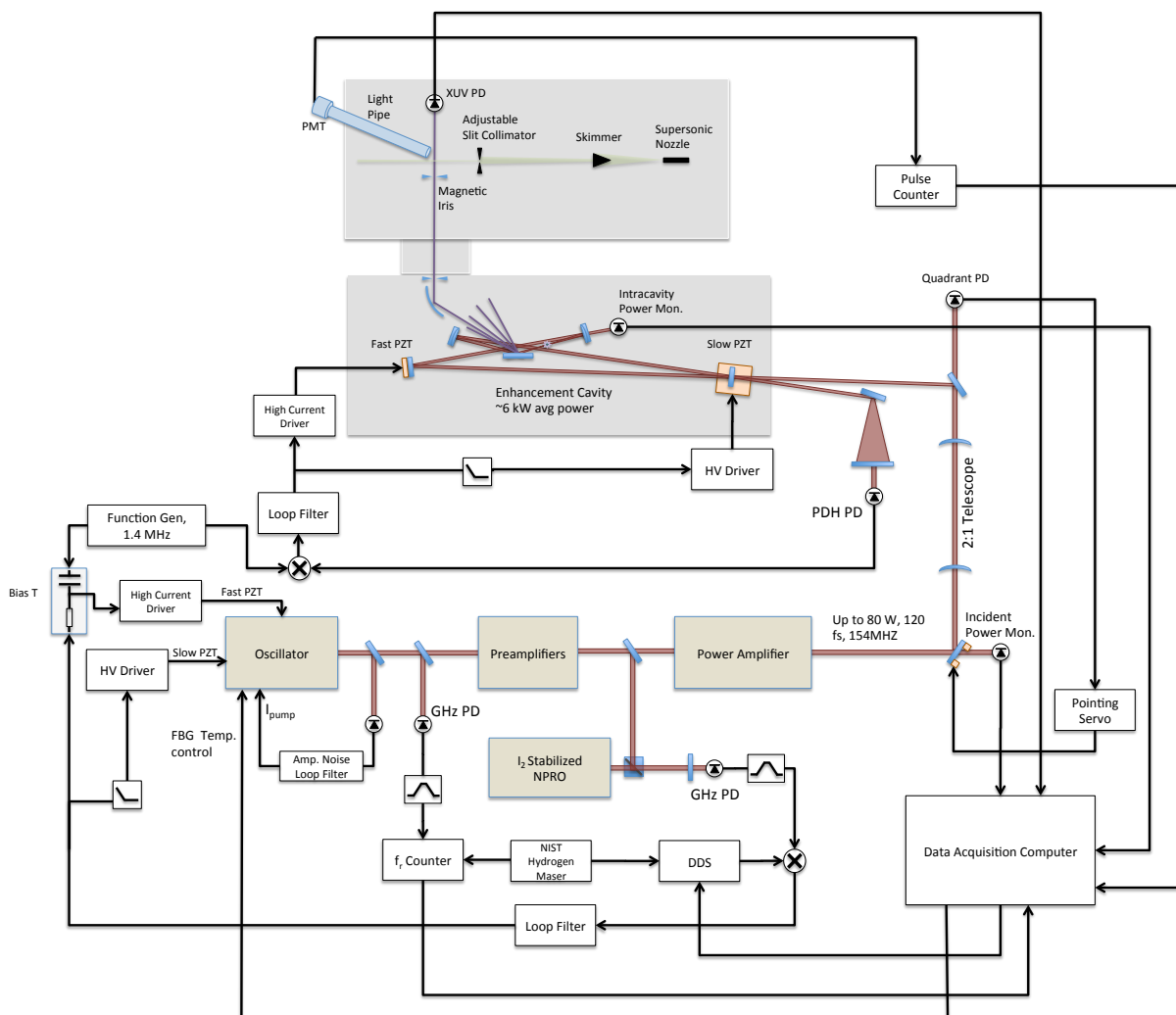
Figure 6.2: Diagram showing the whole stabilization setup for both the enhancement cavity and the excitation laser. This shows most aspects of the spectroscopy experiment.

bandpass filters we utilize to lock the beatnote give a tuning range of 40 MHz $< \Delta' <$ 60 MHz (for our 13th harmonic frequency comb this translates into a tuning range for Δ of 20 MHz $\times 13 = 260$ MHz). Before the comb can be considered fully defined we also have to determine f_r in equation 6.2. We detect the pulse train on a photodetector (Newport D-30) and count the repetition frequency. To implement a frequency scan of our comb, we adjust Δ' and simply record the f_r value at every data point. Any drift in f_r during the measurement is taken into account during the post processing of the data.

With our frequency comb essentially fixed, we must have an actuator within the enhancement cavity to maintain the resonance condition between this fixed frequency comb and the cavity. Therefore, we installed one mirror of the enhancement cavity on a piezo-electric transducer and used that transducer to perform the PDH lock. We were initially concerned that our system would become much less stable by using an intracavity mirror as the length actuator. This is because to keep intracavity losses small, we have to use 0.5 inch diameter optics in the cavity and such a large mass usually results in slow actuation. However, through careful design of the actuator, we were still able to achieve a 35 kHz locking bandwidth. There are several pertinent techniques which were necessary to to enable this large locking bandwidth [109]. One crucial element that is necessary for actuating a large mirror in particular is that the size of the piezoelectric transducer must match the mirror diameter. We utilize square stack PZT's that are 1 cm x 1 cm in size for this purpose (PiezoMechanik PCh 150/10x10/2). To prevent the fast intracavity actuator from running out of range, we also place the input coupler on a translation stage that is actuated with a long travel PZT and use the same technique as discussed in Chapter 3 to ensure that our fast intracavity actuator does not run out of travel. For reference the stabilization setup for both the enhancement cavity and excitation laser is shown in figure 6.2.

6.2　　Atomic beam

The transition at 82 nm will be Doppler broadened to about 4 GHz at room temperature. Since our frequency comb spacing is 154 MHz, roughly 25 comb modes will be resonant with the transition at any given time. In order to see any frequency resolution as we scan Δ, it is necessary that the Doppler width be below the frequency comb spacing such that only one frequency comb mode excites the transition at a given time. To reduce the Doppler width, we use a crossed-beam geometry whereby our XUV frequency comb radiation orthogonally crosses a skimmed, supersonic beam of argon. In the direction of the propagation vector, there is very little atomic motion and therefore the first-order Doppler broadening (given by $\Delta\nu = \mathbf{k} \cdot \mathbf{v}/2\pi$) is minimized.

The supersonic argon source consists of a pulsed valve nozzle (0.5 mm diameter), a 0.5 mm diameter skimmer, and a secondary slit located 33 cm from the skimmer. Both the slit width and its horizontal position are adjustable in order to reduce the Doppler broadening and orthogonalize the atomic beam and XUV beam (see figure 6.2). As an example, with the slit before the interaction region open to 0.5 mm the collimation angle is about 3 mrad, the velocity of the atoms as seen by the XUV radiation has a spread of about 0.75 m/s and the corresponding transverse temperature is around 10 mK. At 82 nm the Doppler broadened width for this slit opening is around 10 MHz.

The supersonic valve generates 500 μs long pulses which we run at a repetition rate of 20 Hz with an argon backing pressure of 0.5 atm. This results in a large gas load given our limited pumping speed (roughly 500 l/s). When increasing the duty cycle of the gas pulses beyond 1%, we observe the pulse density decrease severely (as monitored with a fast ion gauge), which limits further increases in the duty cycle of the gas pulses. To prevent a rising background of argon gas in the interaction chamber which could lead to spurious excitation signal from room temperature atoms, the region between the skimmer and secondary slit was independently evacuated so that there are effectively two differential pumping stages

between the the source chamber and the interaction chamber.

We found nothing to be more difficult in the course of this work than an absolute calibration of our atomic beam density. We commonly used a fast ion gauge to measure the shape of the gas pulses and relative heights under various conditions. Despite our best efforts, the fast ion gauge could not provide us with an absolute measurement of the beam density due to uncertainty in the transfer function and collection area of the detector. In the end, we were forced to estimate our atomic beam density through the magnitude of our fluorescence signal, the cross-section of the transition and our estimated detection efficiency. Through this calculation, we determine that the beam density is about $\sim 10^7$ atoms/mm^3. There is a large uncertainty is the detection efficiency so this can only be considered an order-of-magnitude estimate. Before our system was optimized sufficiently to detect the fluorescence signal, the atomic beam density remained a major uncertainty, hampering our efforts to trouble-shoot the experiment.

When producing a supersonic atomic source, there is the potential to form atomic clusters. Argon gas, being relatively heavy, possesses a large polarizability and therefore has a particular affinity to form clusters. For reference, within a gas species, the cluster formation rate scales as $(P_0 d)/T_0^2$, where P_0 is the backing pressure, d is the nozzle diameter and T_0 is the reservoir temperature [110]. Clustering can cause several unwanted effects. One is an associated heating of the atomic beam. For our purposes though, the most detrimental effect which could be present is the shifting and broadening of the atomic resonance– this could eliminate any frequency structure in our scans of the frequency comb.

We first saw evidence of atomic clustering when comparing a supersonic beam of argon and a supersonic beam of neon with a fast ion gauge. This behavior is shown in figure 6.3. As can be seen, when backing the nozzle with a larger pressure, the argon pulses continue to grow in density whereas the neon pulses stay constant. The property of the neon pulse height to saturate as a function of gas pressure is expected because the rising background pressure in the atomic source chamber will scatter atoms out of the supersonic beam lowering the
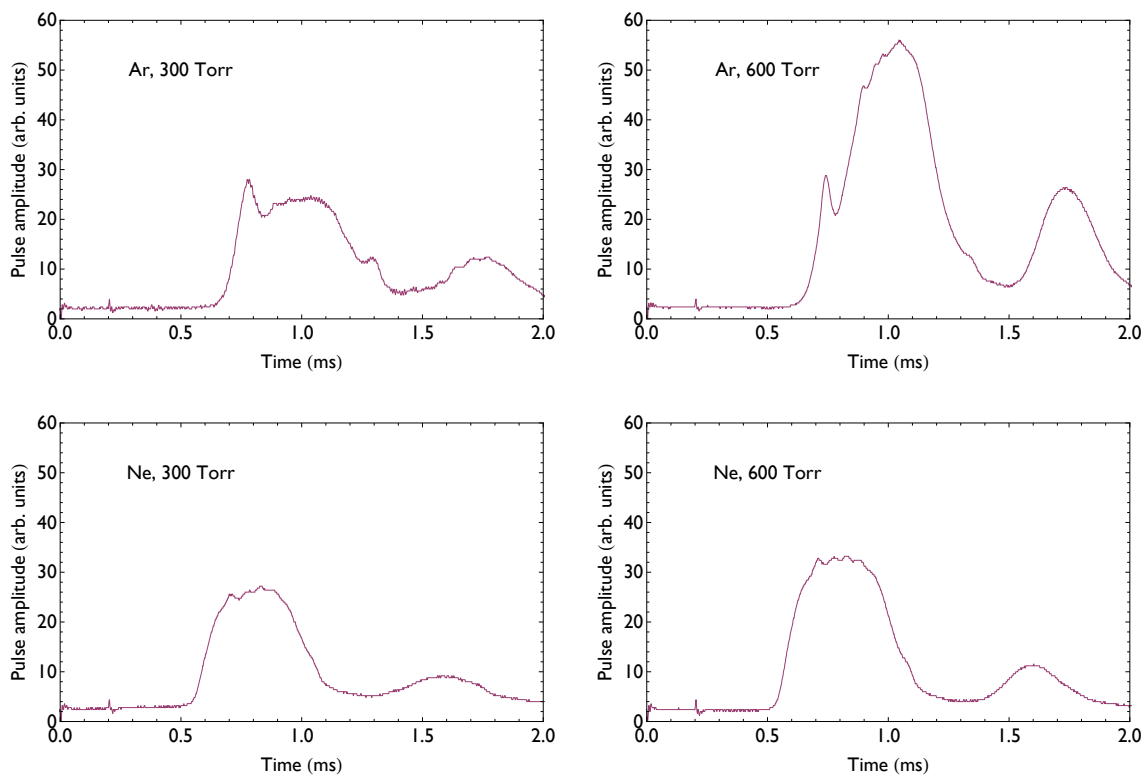
Figure 6.3: Comparison of neon and argon skimmed supersonic gas pulses measured with a fast ion gauge. The nozzle diameter was 0.5 mm as was the first skimmer. As can be seen from the plots, as the gas pressure is increased, the neon pulse height stays essentially the same whereas the argon pulse height grows and distorts somewhat. Also evident in the figure is the slower arrival time of the argon pulses due the larger mass of argon. The secondary pulse present ≈ 800 μs after the main pulse is due to the valve bouncing open briefly after being closed.

density. The property of the argon pulse density to appear to grow as a function of backing pressure as shown in the figure is anomolous. While we do not completely understand this behavior we hypothesize that it is due to clustering in the argon beam. It may be possible that a cluster is not easily scattered from the supersonic beam or that a cluster is more readily detected by the fast ion gauge. In any case neon would not show the same effect because of its lower affinity to cluster. To eliminate clustering of our beam, one possibility is to heat the nozzle. While we have attempted this solution, a higher temperature beam is also more difficult to collimate and we found it more straightforward to keep the backing pressure on the gas nozzle sufficiently low.

6.3   Excitation and detection

After the harmonic frequency comb is generated and outcoupled from the cavity, it is roughly collimated using a toroidal mirror with an effective focal length of 16 cm (see figure 6.2). A toroidal mirror is a focusing optic designed to be used at a glancing angle of incidence and thus it has a different radii of curvature in the vertical and horizontal dimension to minimize astigmatism– this particular mirror has a design incidence angle of 60°. Our toroidal mirror is composed of fused silica. It has no optical coating which has only $\sim 30\%$ reflectivity even at the 60° angle of incidence. After collimation, the 13th harmonic beam is sent through a 1.5 mm diameter pinhole placed in an aluminum plate near the port of the enhancement cavity chamber. This pinhole eliminates much of the long trajectory radiation, which is not well collimated, and also blocks background radiation from plasma recombination, the intense scattered fundamental radiation or other harmonic orders. The long trajectory component of the harmonic frequency comb will, in general, be less coherent due to the larger α_q parameter discussed in Chapter 4. However, our main reason for attenuating the long tajectory radiation is to maintain a very high beam quality. This is crucial for the detection of our fluorescence signal with low scattered photon background.

After the 13th harmonic beam exits the pinhole it propagates through a vacuum tube
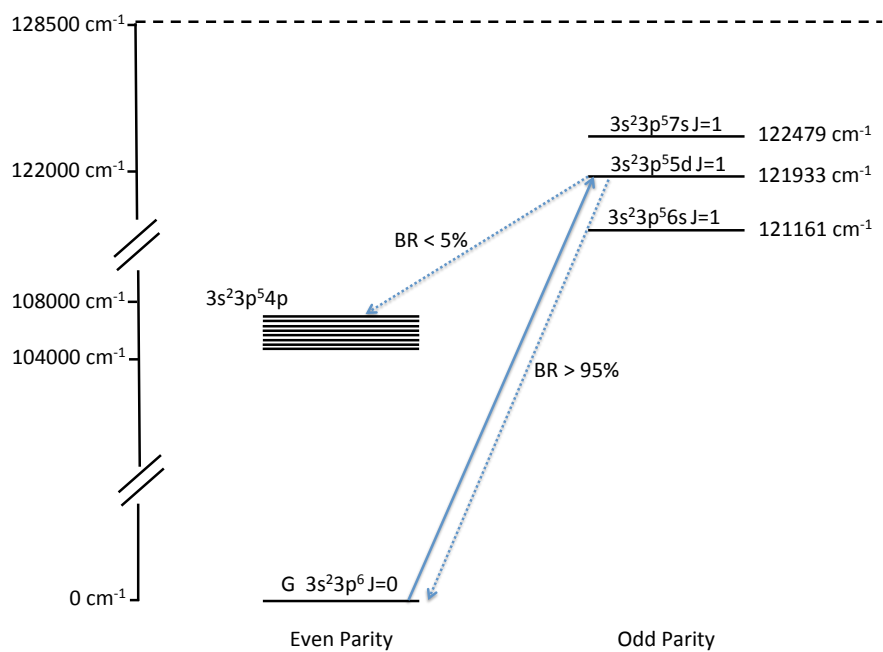
Figure 6.4: Relevant energy levels in neutral argon for spectroscopy at 82 nm. After excitation to the $3s^23p^55d$ J=1 state, radiative decay can occur to the ground state with a branching ration (BR) of $\sim 95\%$. Population can also decay to several levels with the configuration $3s^23p^54p$ as shown in the figure, but the BR for these decays is only $\sim 5\%$ collectively.

to the spectroscopy chamber. An adjustable iris is placed directly before the interaction chamber that serves both to reduced scattered photons (originating from the first pinhole and the background light in the harmonic chamber) and to provide differential pumping as there is a high background of xenon gas in the enhancement cavity chamber. Excess xenon gas in the interaction region can be ionized and then radiatively recombine producing background. A small rare-earth magnet is attached to the iris so that it is adjustable from outside of the vacuum chamber with the use of another magnet. This is helpful because we can align the harmonic beam precisely on the center of the iris before reducing the final diameter to 1-2 mm– all without breaking vacuum.

In the interaction region the harmonic beam crosses the atomic beam at a near 90° angle exciting the transition. As can be seen in figure 6.4, there are several levels which could be excited without XUV frequency comb in principle. The harmonic bandwidth of our frequency comb is uncertain therefore we did not initially know if we would excite a single transition or several simultaneously. By doing frequency scans, we found that we were exciting only one transition. Later, by determining the absolute frequency of the transition, we found that we were exciting the 5d J=1 transition at 121933 cm^{-1}.

After excitation, the argon atoms can radiatively decay to the ground state or a few other high lying states. While the transition rates to the high lying states are known, the transition rate to the ground state is not. However, since spontaneous emission rates are proportional to λ^{-3}, for reasonable estimates of the dipole moments the atoms will decay predominantly back to the ground state with $\sim 95\%$ efficiency. For this reason we detect the fluorescence directly at our 82 nm excitation wavelength which is also convenient since detectors at this wavelength will typically be insensitive to background visible light.

An interesting feature of the fluorescence pattern from decay of the excited state to the ground state arises because we are exciting a J=0 to J=1 transition with a π polarization (in the lab frame this corresponds to vertical polarization). Therefore excitation is from the $m_j = 0$ state to the $m_j = 0$ state and decay is between only these two states as well. Therefore

the fluorescence has a well defined dipole radiation pattern with no fluorescence emitted directly along the axis of the dipole. Because our polarization is vertical, this means that there is no fluorescence emitted directly above our interaction region. To complicate matters further, the atomic and harmonic beams are propagating in the xy plane so the detector must be placed in the least-ideal position directly above the interaction region to avoid interfering with the path of the beams. We can find the geometric collection efficiency by integrating over the dipole radiation pattern as shown in figure 6.5. With this calculation, it becomes clear that the collection efficiency is adversely affected unless the detector subtends a large solid angle. Our detector area is about 1 cm and we therefore place this detector only a few mm above the interaction region ($d/s \approx 0.5$ in the figure). This makes our system extremely sensitive to any scattered photons and the alignment through the pinhole and the iris shown in figure 6.2 must be nearly perfect. Additionally, the flux of radiation that contributes to our background is 10^5 times larger than what contributes to our signal. One advantage for the detection of XUV radiation is that scattered radiation levels are somewhat reduced due to the efficient absorption of XUV radiation by all solid materials.

The alignment of the harmonic beam to the interaction region is difficult because harmonic light can only be generated when the entire system is under vacuum and there is only one optical element (the toroidal mirror) which can be used for this alignment. The use of only one optic is intentional since, at XUV wavelengths, optics have quite poor reflectivity and we desire to maintain a high flux of photons for spectroscopy. Therefore, the toroidal mirror is both translated and angle adjusted for perfect alignment through all the apertures. We accomplish this by first aligning a tracer laser beam at 532 nm exactly colinearly with the harmonic beam with the system under vacuum. We then break vacuum to adjust the toroidal mirror, aligning the tracer beam precisely through all the apertures. Afterwards, with the system back under vacuum and generating harmonic radiation, final small adjustments to the alignment are accomplished using motorized actuators on the toroidal mirror.

Our fluorescence detector consists of a UV grade lucite lightpipe whose front surface
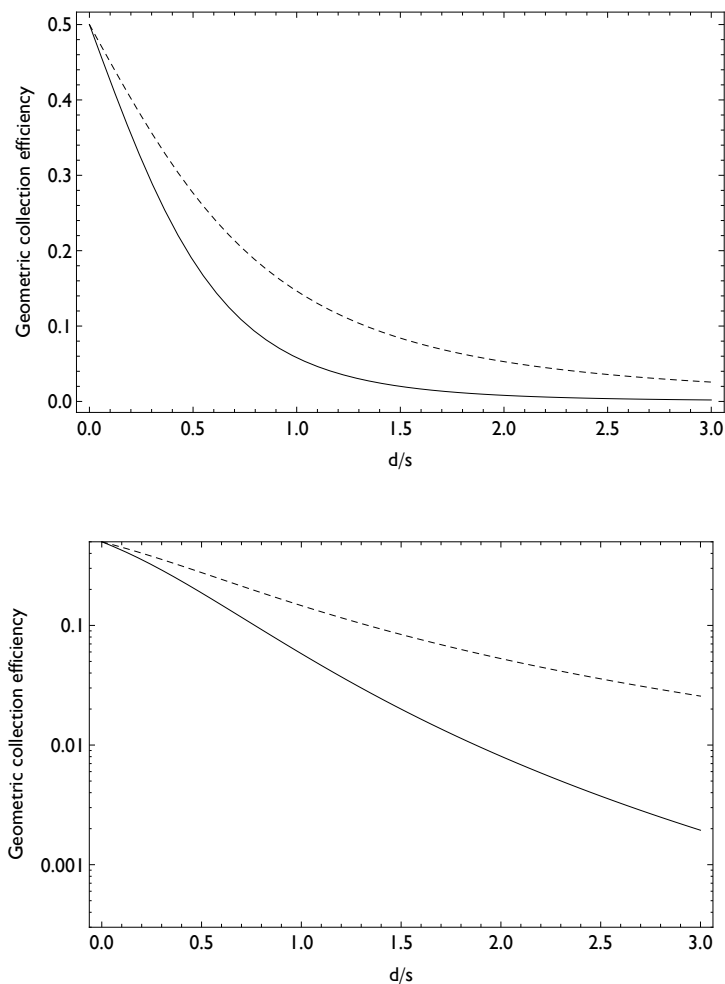
Figure 6.5: The geometric collection efficiency of our detector as a function of the ratio d/s, where d is distance of the detector from the interaction region and s is the radius of the detector. The dotted line shows the result if the fluorescence is emitted uniformly into 4π Steradians. The solid line shows the integration of our actual dipole fluorescence pattern. As can be seen from the figure our experimental collection efficiency has a lower geometric collection efficiency than the uniform fluorescence pattern for all values of d/s except when $d = 0$ at which point both have a collection efficiency of 50%. The lower panel is identical to the upper panel only on a logarithmic scale.

is coated with sodium salicylate. When an 82 nm photon is incident on this surface, it excites the sodium salicylate which fluoresces at ~ 420 nm. A large portion of this radiation is then guided by the light pipe outside of the vacuum chamber where it is detected by a photomultiplier tube optimized for single photon detection (Hamamatsu H11123) and a pulse counter (Stanford Research, SR400). Since our harmonic frequency comb is essentially a continuous source while our atomic beam is pulsed, it is useful for us to record the photon counts both with and without argon gas present at the interaction region for differential measurements. Therefore the pulse counter is gated twice every gas pulse repetition period–once coincident with the argon pulse arrival time to measure the actual signal, and once between argon pulses to measure background. For all the frequency scans presented, we subtract the background counts so that the average value of the signal should be zero with the frequency comb detuned from the transition.

The harmonic power that our system generates is not very constant over time and can drift significantly over the course of an individual frequency scan (~ 150 s). Therefore, it is necessary to normalize the fluorescence signal to the total 13th harmonic power which transverses the interaction region. To accomplish this normalization, we place an XUV photodiode after the interaction region. The diode is turned so the radiation bounces off the diode at a near $90°$ angle and is sent to a beam dump to help decrease scatter. When the frequency comb is on resonance with the transition, only a single comb mode is partially absorbed.

6.4 Frequency scan results

Our attempts to observe high resolution spectroscopy signal as we scanned the XUV frequency comb over the argon transition were initially unsuccessful. To increase the atom number in the interaction region, we had initially performed frequency scans with a high backing pressure of argon gas on the supersonic nozzle (usually several atmospheres). We chose this strategy because, as discussed earlier, we initially did not know our pulse density

and so we were concerned that a lack of signal was indicative of a low atom density. At these pressures, we were never able to see a narrow spectral feature in our frequency scans.

After seeing evidence of atomic clusters as discussed earlier and shown in figure 6.3, we decided to use 300 Torr of backing pressure on the nozzle to reduce the clustering rate as much as possible. At this pressure, we were able to observe single comb-tooth resolved spectroscopy for the first time and ascertained that it was very probable that the lack of frequency resolution had been due to a high percentage of atomic clusters within the beam. In figure 6.6, we compare the fluorescence signal obtained at 300 Torr backing pressure with the signal obtained at 600 Torr of backing pressure. As can be seen in the figure, we obtain essentially no frequency structure with the higher backing pressure. There is some increase in overall counts above the baseline which leads us to believe that the main effect we are seeing is a broadening of the transition width. Therefore, we use the relatively low backing pressure of 300 Torr for all of our frequency scans to determine the absolute frequency of the transition.

Shown in figure 6.7 are the fluorescence counts as a function of $\Delta = 13\Delta'$, the XUV offset frequency. By scanning over the full 250 MHz of scan range in the XUV we see two separate comb modes excite the transition, separated by our repetition rate of 154 MHz. For this long scan range, the atomic beam collimation was set to be ≈ 40 MHz and by fitting the line, we find that the width of the transition is ≈ 46 MHz, in good agreement. The atomic beam was only collimated to this level because we wanted to maintain a high level of signal for the large scan range. The photon counts are normalized to the total XUV flux and the background photon counts, determined from the second gate of the pulse counter, was subtracted as previously described. Figure 6.7 also shows that with the scattered photon background subtracted (which is roughly twice the magnitude as the signal), the baseline of the frequency scans is consistent with zero. This is an important point because it shows that there is not a significant background of incoherent radiation except the power that resides in the comb teeth.
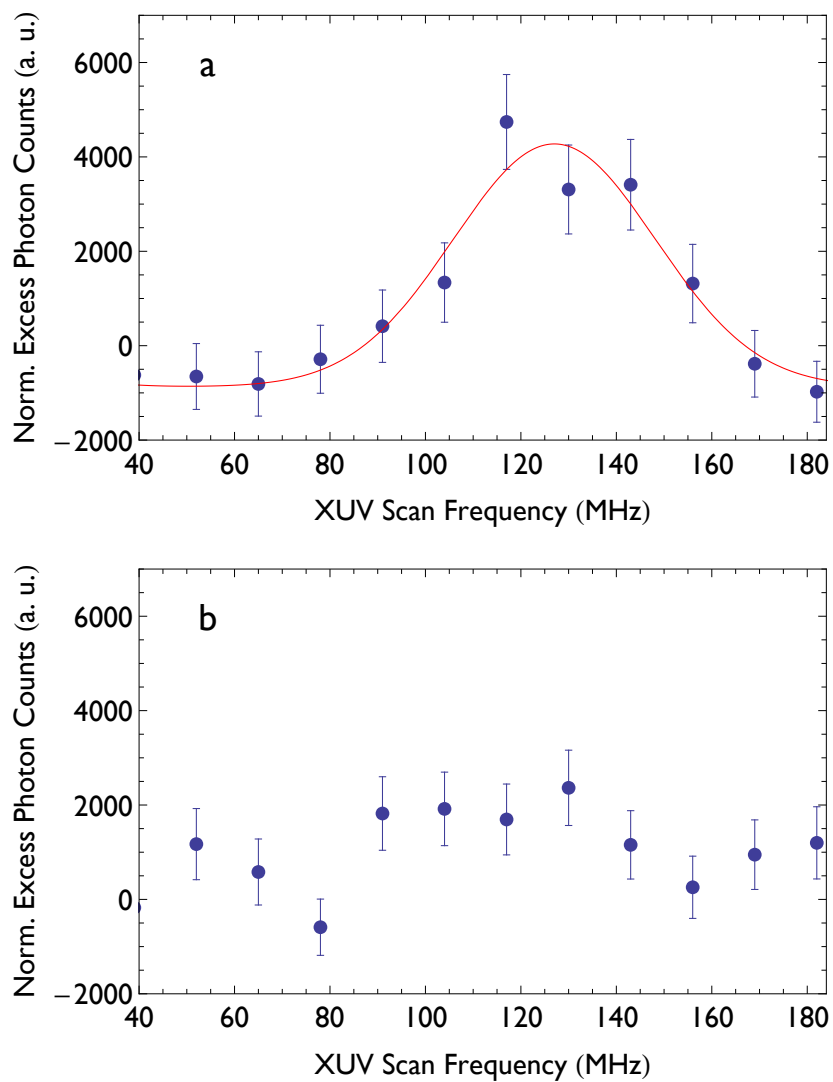
Figure 6.6: Back-to-back frequency scans. a) with a backing pressure of 300 Torr. b) with a backing pressure of 600 Torr. We hypothesize that the disappearence of frequency resolved signal at the higher pressure is due to clustering of the atomic beam as described in the text.
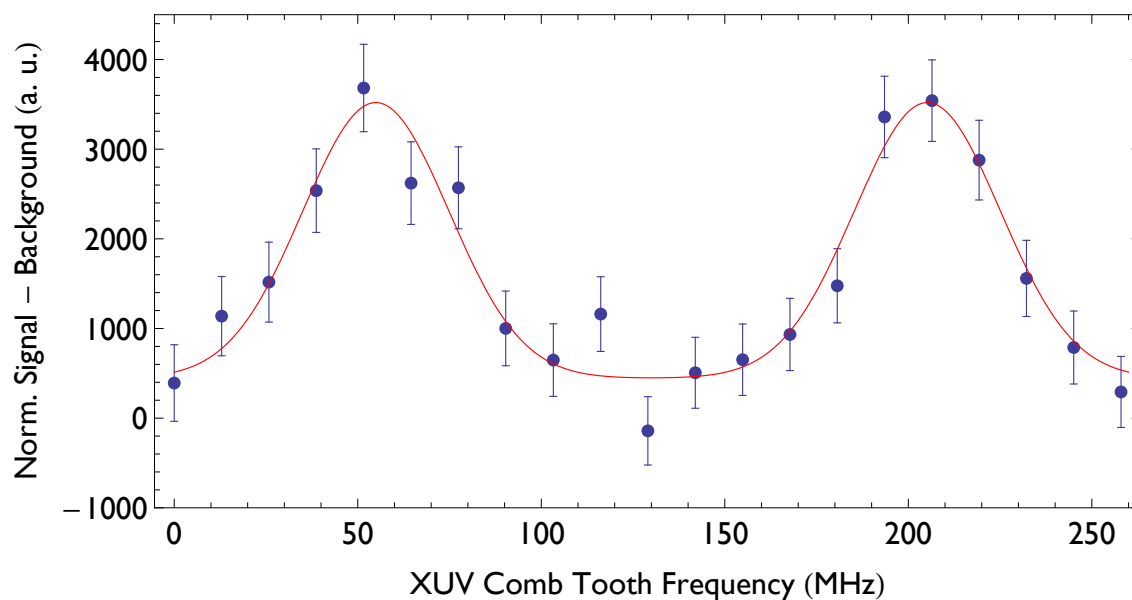
Figure 6.7: Scan of the frequency comb over the excited transition in neutral argon. Since $\Delta = 13\Delta' = 250$ MHz two separate comb teeth in our 154 MHz repetition rate frequency comb excite the transition. The collimation of the atomic beam was set to provide a ~ 40 MHz Doppler broadened linewidth. The red curve is the result of fitting the data with two gaussian functions. The recovered linewidth obtained by fitting the data gives a linewidth of 46 MHz in good agreement.
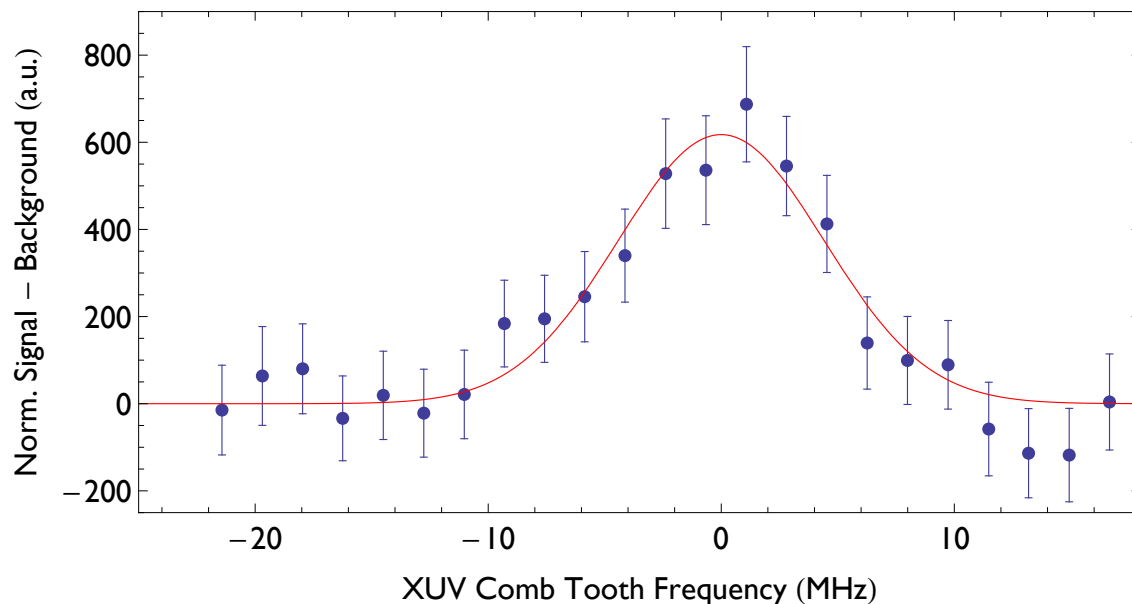
Figure 6.8: Scan of the frequency comb over the excited transition in neutral argon. In this case, the collimation of the atomic beam was set to provide a ~ 10 MHz Doppler broadened linewidth. The recovered linewidth obtained by fitting the data with a Gaussian function (red curve) gives a linewidth of 10.6 MHz in good agreement. Fitting the data with a Lorentzian function as opposed to a Gaussian leads to statistically equivalent fit errors (therefore our data does not give an indication of whether the linewidth is limited by Doppler effects or the natural linewidth of the transition).

There is no reported value for the dipole moment between the ground state and the excited state, but reasonable estimates lead to a transition width of $\approx$ 10 MHz. To test the XUV comb linewidth further, we increased the collimation to the same level (this was accomplished by setting the second collimation slit width to 0.5 mm). The recovered width of the transition is apparently still Doppler limited as the width continued to decrease in accordance with the increase in collimation all the way to 10 MHz. The signal size also falls with increased collimation so that it was very difficult to decrease the Doppler-broadened linewidth further to determine the true natural linewidth. From this demonstration, we can safely claim that the linewidth of the comb teeth and the natural linewidth of the transition are both below 10 MHz.

6.5   Comb mode number determination

By scanning our frequency comb mode over the transition and determining the line center we effectively make a single measurement which, through equation 6.2, constrains the argon transition according to

$$\nu_{ar} = mf_{ri} + 13\ \nu_{YAG} + \Delta_i. \tag{6.4}$$

Here m is unknown and therefore this single measurement does not determine ν_{ar}. Therefore, at least one more comparable measurement at a different repetition frequency is required.

$$\nu_{ar} = (m + \Delta m_f)f_{rf} + 13\ \nu_{YAG} + \Delta_f. \tag{6.5}$$

Here, we assume that we know the change in comb number, Δm_f, exactly. Solving these two equations for m gives

$$m = \frac{\Delta_f - \Delta_i + \Delta m_f f_{rf}}{f_{ri} - f_{rf}}. \tag{6.6}$$

To accurately determine the comb tooth number, the uncertainty in this determination must be less than 1. Therefore we require that

$$\sigma_m \approx \frac{\sqrt{\sigma_{\Delta_i}^2 + \sigma_{\Delta_f}^2}}{f_{ri} - f_{rf}} < 1, \tag{6.7}$$

where we use the notation that σ_x is the measured uncertainty in the quantity x. Equation 6.7 takes into account that error in the repetition frequency is much smaller than the value of Δ at the resonance. Experimentally, we find that the uncertainty in the extracted Δ of our frequency scans is about 1 MHz. Thus to determine the comb tooth number we have to change our repetition frequency by at least 1.4 MHz between our initial and final measurements.

We assume that we know the Δm_f perfectly in the previous analysis but we need an algorithm for determining this. We can obviously count the number of times that the transition is excited as we move the repetition frequency from f_{ri} to f_{rf}. This would be an extremely tedious and time consuming process though. Instead, we implement an algorithm where we perform several additional scans at specially selected repetition frequencies chosen to ensure that we do not lose track of Δm between any two measurements.

If we have a rough idea of the value of m, then we can determine Δm exactly for a given repetition rate change provided that the change is not too large. We first move our repetition frequency from f_{ri} to f_{r1} where $|f_{ri} - f_{r1}| << |f_{ri} - f_{rf}|$.

$$\Delta m_1 = \frac{m_i(f_{ri} - f_{r1}) - \Delta_1 + \Delta_i}{f_{r1}} \tag{6.8}$$

$$\Rightarrow \sigma_{\Delta m_1} \approx \frac{\sigma_{m_i}(f_{ri} - f_{r1})}{f_{r1}} \tag{6.9}$$

Here m_i and σ_{m_i} is our initial knowledge of m and its uncertainty, respectively. Equation 6.9 is obtained because the uncertainty in equation 6.8 is dominated by the uncertainty in m. Obviously, if we want to keep $\sigma_{\Delta m_1} < 1$, and our initial uncertainty in m is large then the first change in repetition frequency will have to be small. If the condition in equation 6.9 is met, however, we can use the analogues of equations 6.6 and 6.7 to obtain a more precise value of m.

$$m_1 = \frac{\Delta_1 - \Delta_i + \Delta m_1 f_{r1}}{f_{ri} - f_{r1}} \tag{6.10}$$

$$\sigma_{m_1} \approx \frac{\sqrt{\sigma_{\Delta_i}^2 + \sigma_{\Delta_1}^2}}{f_{ri} - f_{r1}} \tag{6.11}$$

Therefore, through our two measurements, we did not obtain the precise value of m, but we did obtain a value with a corresponding σ_m which is smaller than the initial uncertainty.

Now a viable algorithm emerges. When we make a repetition rate change, we calculate Δm and $\sigma_{\Delta m}$ given equations 6.8 and 6.9 using our best previous value for m. We make the repetition rate small enough to ensure that $\sigma_{\Delta m} < 1$ and we therefore know Δm exactly. Then we calculate a new, more precise value for m using equation 6.10 and an uncertainty in that number using equation 6.11. We can then repeat this process and make another measurement at a different repetition frequency. Since our value for m has now increased in precision our repetition rate change can be larger than for the previous measurement. We simply repeat this process with increasingly large changes in the repetition rate until the total difference in the initial and final repetition rates is large enough that the requirement in equation 6.7 is met. At that point, we have determined our comb mode number exactly. If we know the comb mode number exactly, we can then use any individual measurement to determine the absolute transition frequency to a precision limited by σ_Δ.

We can estimate how many measurements we will need to make an absolute frequency determination. It is easy to show that if we make three measurements then the uncertainty in the change in comb tooth number for the third measurement is given by

$$\sigma_{\Delta n_3} \approx \frac{\sqrt{\sigma_{\Delta_2}^2 + \sigma_{\Delta_3}^2}}{f_{r3}} \times \frac{(f_{r1} - f_{r3})}{(f_{r1} - f_{r2})} \tag{6.12}$$

For our experiment, our linecenter determination is accurate to approximately 1 MHz so that the first factor in equation 6.12 is roughly 0.01. Therefore, for every subsequent measurement, we are able to change the repetition frequency by two orders of magnitude more than the previous change. Our initial uncertainty in the comb mode number is roughly 1×10^6 simply because we know that our spectral bandwidth is not more than a few nm centered around 82 nm. This translates into an initial repetition rate change of no more than 100 Hz. With every repetition rate change being two orders of magnitude larger, we should be able to easily complete the absolute frequency determination in four measurements (by making an initial
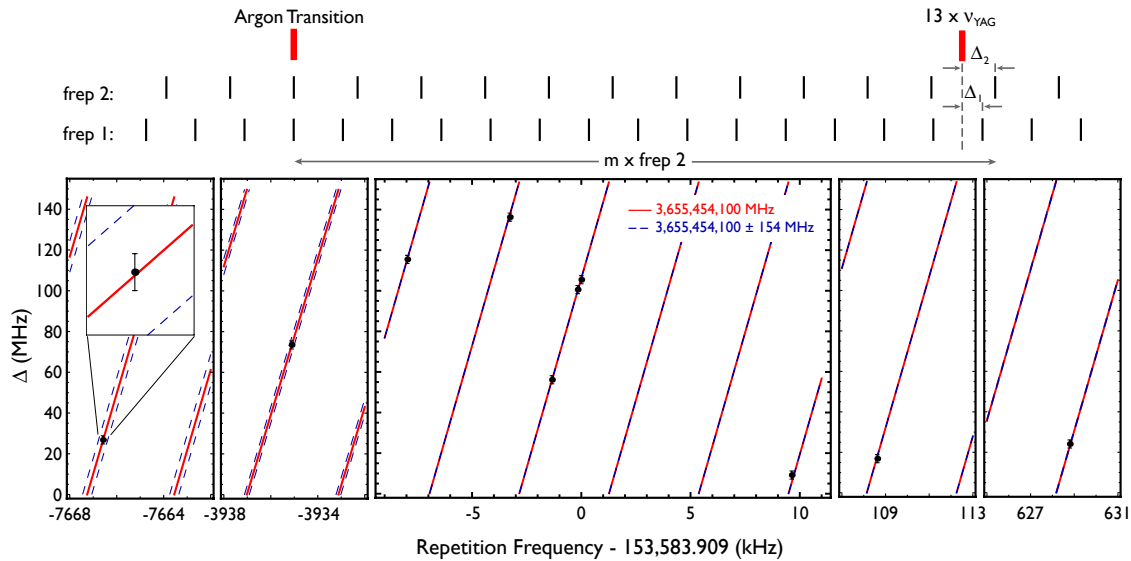
Figure 6.9: Measurement of the resonance centre frequency at 10 different values of f_r parameterized by the offset, Δ, of the 13th harmonic fixed point from $13 \times \nu_{YAG}$. Also plotted are three lines: a solid red line showing the expected location of the resonance centers for the extracted comb tooth number, m, and two blue dashed lines showing the expected locations for $m \pm 1$. The inset shows a zoomed in version of a measurement, which demonstrates that the comb tooth number is unambiguously determined. The comb mode number depends on the repetition frequency but at a repetition frequency of 153,583,909 Hz (the reference frequency on the graph), m=-37,391.

measurement and then changing the repetition rate by roughly 100 Hz, 10 kHz and 1 MHz). For the actual experimental determination, we made ten measurements to offer redundancy.

With all of our measurements completed, they should all comply with the following equation for Δ.

$$\Delta = \nu_{ar} - \nu_{ref} - m f_r = \nu_{ar} - \nu_{ref} - \text{Ceiling} \left[\frac{\nu_{ar} - \nu_{ref}}{f_r} \right] f_r \qquad (6.13)$$

where Ceiling[ ] is the round-up function. This is shown in figure 6.9 along with our experimental data. The lines correspond to three different values of ν_{ar}, separated by 154 MHz, and demonstrate the unambiguous comb tooth determination graphically. Note that according to the equation, Δ wraps when m changes by 1.

If the atomic beam and 13th harmonic beam do not cross at a perfect $90°$ angle, there will be a systematic error given by the residual Doppler shift of $(v \, \delta\theta)/\lambda_{13}$ where $\delta\theta$ is the error in the angle, v is the velocity of the atomic beam and λ_{13} is the 13th harmonic wavelength of 82 nm. This systematic is inconsequential in determining the comb mode number provided the systematic shift does not vary between measurements. This can be understood because to determine the comb mode we are only concerned with the difference in the measurements represented by equation 6.4. However, if the beam pointing changes significantly between measurements at different repetition frequencies, then the determination of the absolute comb mode number is impossible. To account for this effect we monitored the 13th harmonic XUV beam position at the exit of our spectroscopy chamber to ensure that the beam pointing variations between measurements produced Doppler shift errors below our statistical uncertainties. Through careful realignment of the enhancement cavity after repetition rate changes, we did not observe beam pointing changes above this level.

6.6   Absolute frequency determination

Once the comb mode number m is determined, we must correct our final measurement determined through equation 6.4 for a possible residual Doppler shift arising from a variation

of the alignment of the laser and the atomic beam away from a 90° angle. For a rough align-ment of the atomic and XUV beams, we measured the angle between visible tracer beams which we aligned through the relevent apertures. To measure the angle more precisely, we compared the measured transition frequency of a pure argon beam with that of a helium argon mixture (5:1 helium/argon partial pressures). Since the gas mixture of helium and argon should have a faster velocity than the pure argon beam, the Doppler shift systematic should also be proportionally larger. Therefore, this gives us a means to identify and elim-inate that systematic effect by adjusting the angle of the atomic beam. In practice this is accomplished by translating the final atomic beam collimation slit until the two measured transition frequencies for different argon beam velocities agree, which ensures orthogonality between the laser and the atomic beams to within our measurement error.

In order to judge the sensitivity of this procedure, it was necessary to measure the beam velocity of both the gas mixtures and the pure argon beam. In principle the fast ion gauge can provide this information but we found that the distortion and length of the gas pulse made this an imprecise measurement. A more precise technique is to measure the transition frequency in argon at several different angles of the atomic beam for both the pure argon beam and a 3:1 helium/argon mixture. This is shown in figure 6.10. The slope of the lines shown in the figure provide the essential information to calculate the beam velocity since we know the distance from the skimmer to the collimating slit. From this data, we found that the velocity of the pure argon beam is 520 ± 20 m/s and the velocity of the 3:1 mixture is 646 ± 20 m/s. We also measured a 5:1 mixture of helium and argon at a single angle. By measuring the comparative shift we found that beam velocity of the 5:1 mixture to be 740 ± 60 m/s. We decided to use the 5:1 mixture with the higher velocity beam to orthogonalize the angle between the XUV beam and the atomic beam. Our motivation for this is simply based on the fact that the larger the velocity difference between the two beams, the more sensitive the measurement will be to a misalignment leading to a Doppler shift.

After performing the orthogonalization procedure, the results of two frequency scans
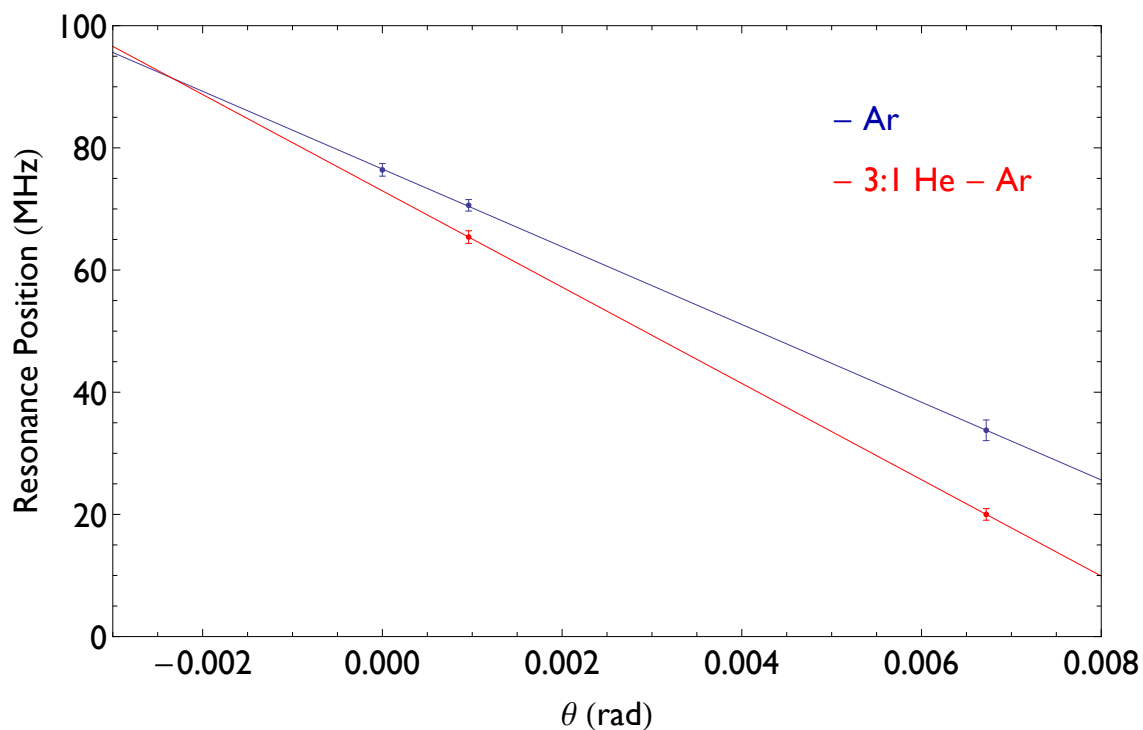
Figure 6.10: Transition frequency as a function of the angle of the atomic beam for both a pure argon beam (blue curve) and a 3:1 mixture of argon and helium (red curve). From this plot, the velocities of the of the two mixtures can be determined as well as the adjustment required to reach orthogonality (the intersection of the lines). The velocity of the pure argon beam was found to be 520±20 m/s while the velocity of the 3:1 mixture is 646±20 m/s. Note that the angle $\theta = 0$ in the graph is only nominally zero and the orthogonal position of the two beams occurs when $\theta \approx -0.002$
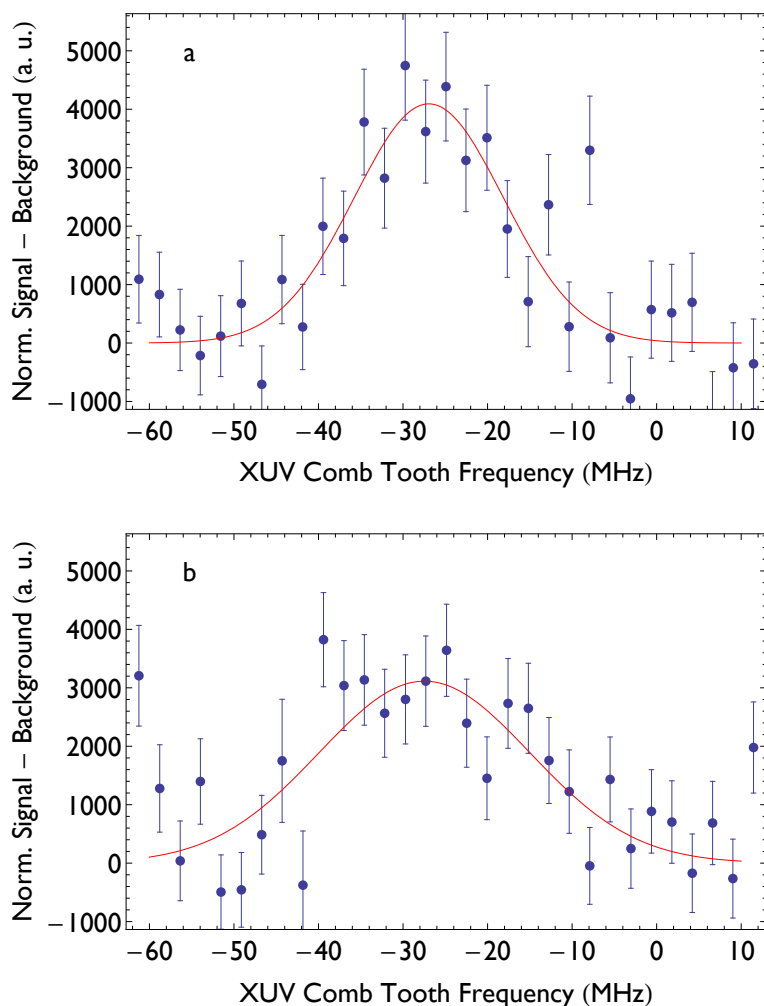
Figure 6.11: The measurement of the 5d transition frequency in a) a pure argon atomic beam and b) in a 5:1 helium/argon gas mixture. The gas mixture is about 40% faster than the pure argon beam but the measured transition frequency found by fitting the data only disagrees by 0.5 MHz which is within the statistical uncertainty of ~ 1 MHz. Note that the transition width is also wider for b) since the residual Doppler width from the finite collimation angle also scales with the velocity. The error bars shown on these plots are larger than for our other frequency scans because we averaged for less time per point.

(one in pure argon and one in a 5:1 mixture of helium and argon) are shown in figure 6.11. From the fractional change in the velocity of the two beams, the statistical uncertainty in the two measurements shown in the figure leads to an uncertainty in the deviation of the crossing angle of the XUV and atomic beams from orthogonality of about 0.5 mrad (0.03°). This, in turn, leads to a systematic uncertainty of the Doppler shift of 3 MHz. This is our largest systematic uncertainty.

All other systematic shifts such as recoil, density, and Stark shifts, as well as the uncertainty in ν_{YAG}, are estimated to be smaller than 1 MHz. The recoil shift is the largest at ≈ 630 kHz. The ac stark shift is inconsequential due to our low intensity in the excitation radiation (we estimate the shift is less than 1 Hz). The density shift is also very small since our atomic beam has only a pressure of $\sim 10^{-6}$ Torr– the corresponding shift is on the order of 1 Hz. The uncertainty in the frequency of the reference laser, ν_{YAG}, is 5 kHz. This leads to an uncertainty at the 13th harmonic of 65 kHz.

We have also investigated whether there are unconsidered systematic effects in the calibration of the XUV comb frequencies that depend on the pressure of the xenon gas target or the generating laser power. Although we did not take data while specifically varying these experimental quantities, due to instabilities in our HHG system, these parameters varied significantly in subsequent frequency scans. This allowed us to bin our data for different laser operation conditions to check these systematic effects. We found no systematic shifts at the 2 MHz level for 30% change in xenon backing pressure. We also found no systematic effects for a 20% change in the intracavity power for HHG.

The final absolute frequency for this transition is 3,655,454,073±3 MHz. This agrees well with the previous best measurement of this transition frequency which has an uncertainty of 2.3 GHz [111].
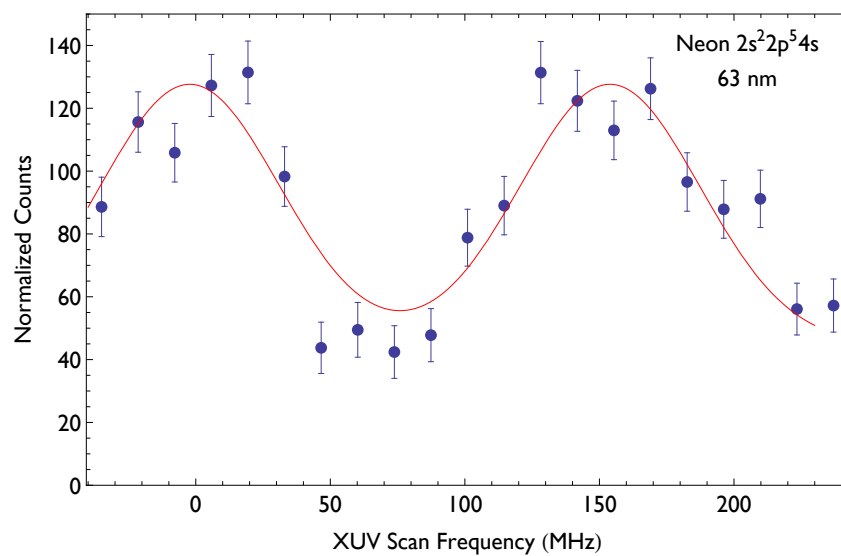
Figure 6.12: The signal for the neon transition with $\sim$ 4 mrad collimation angle. The contrast and signal-to-noise are lower due to the increased Doppler width and the smaller absorption cross-section, respectively.

6.7 Spectroscopy of neon with the seventeenth harmonic

To show the versatility of our harmonic frequency combs and our ability to push the system even deeper into the XUV spectral region, we also excited a transition in neutral neon (with configuration $2s^2 2p^5 4s$) that lies within our 17th harmonic bandwidth. The harmonic is centered at about 63 nm– far into the above-threshold HHG region.

Due to the smaller atomic mass of neon, the atomic beam velocity is significantly higher (the increase in speed can clearly be seen in figure 6.3). This makes it more challenging to obtain a narrow Doppler width through geometric collimation. In addition, the cross section of a closed transition is given by $\lambda^2/(2\pi)$. The transitions we excite in both argon and neon are not closed transitions but this is still a reasonable estimate since the radiative decay is predominantely to the ground state. Therefore the absorption cross section in neon is about 60% the cross section in argon. This, along with the increased atomic beam velocity, made it more challenging to excite and detect fluorescence from a well collimated supersonic beam of neon.

We were able to scan through the Doppler broadened transition as shown in figure 6.12. This demonstration shows that, in principle, the same absolute frequency measurements can also be completed in neon at 63 nm with the 17th harmonic.

Chapter 7

Conclusion

With the spectroscopic measurements utilizing an XUV frequency comb presented in this thesis, we have effectively shown that there is a feasible path towards ultrahigh resolution spectroscopy below 100 nm. If the wealth of science enabled by the optical frequency comb is any indication, we anticipate that the XUV frequency comb will have many unanticipated applications beyond what we have so far imagined.

Still, while the XUV frequency comb is now a viable scientific tool, it is far from being a "mature" technology. As mentioned in Chapter 4, there is currently a disconnect between the level of noise measurable in the XUV comb and the level of noise that we anticipate to be present due to the estimated noise upconversion processes. In the field of stable lasers, this situation may seem strange since the first optical heterodyne beatnotes were demonstrated within a few years of the first laser. However, it should be stressed, that even the most simple optical techniques necessary to perform such tests become difficult– or impossible– in the XUV. Obtaining a beamsplitter and a narrow-linewidth XUV source for a heterodyne beatnote experiment is orders-of-magniture more challenging below 100 nm where there is no material transmission, the entire optical setup must remain in vacuum and the radiation source is difficult to produce. However, to truly observe the relevent noise processes and to study the high-harmonic process itself will require that we take these steps.

Our current Yb fiber frequency comb is capable of supplying 80 W of average power. We currently use only ∼30 W of this output. It is feasible to consider splitting the power

to excite two enhancement cavities simultaneously. We could then perform a heterodyne beatnote between the two generated XUV frequency combs to study the noise processes. Of course, since some of the noise in the XUV frequency combs will be correlated (any noise traceable back to the phase noise of the Yb frequency comb), this test in and of itself will not fully determine the linewidth. However, by introducing differential amplitude and phase fluctuations onto the field exciting one cavity independent of the other cavity, every noise process can be fully quantified.

Once the noise processes are fully understood and experimentally determined, it will be fruitful to investigate exactly how precise the XUV frequency comb can be made. If, as we anticipate, the noise in the XUV comb is entirely traceable back to environmental perturbations on the enhancement cavity or noise in the Yb excitation frequency comb, then there will be almost no limit to how sharp we will be able to make the individual XUV comb teeth (excepting our patience). We will simply need to push for exceptional feedback loops (in terms of locking bandwidth) at every stage in our system, and eliminate any noise entering our setup at the source, if possible. One could speculate that soon the ultimate limit to the linewidth of the XUV comb will be due to the vanishingly small phase noise present on current, state-of-the-art ultra-stable visible lasers locked to high-finesse cavities as discussed in Chapter 6.

With the XUV frequency comb, there are also already published plans for conducting high resolution spectroscopy on neutral helium (the 1^1S-2^1S at 2×120 nm) in a magic-wavelength dipole trap [112]. There is a published proposal to measure the 1S-2S transition in He$^+$ as well. This proposal involves holding a single He$^+$ ion in an ion trap and sympathetically cooling it with Mg$^+$ (2×61 nm) [113]. These ambitious proposals highlight two needs for further XUV comb research and development. The first is a continued increase in XUV flux as the count rates predicted for these experiments are relatively low. The second need is for wavelength tunable XUV frequency combs. Our current system is not tunable and we currently come close to exciting the transitions cited above but most likely our laser

system and enhancement cavity would have to be somewhat redesigned to perform either of these experiments. A relevent scientific goal for the future would be to develop quasi-tunable XUV frequency combs. Ti:Sapp would certainly provide a more tunable laser system but would most likely be limited by the enhancement cavity dispersion.

An intriguing idea proposed in reference [104] is to extend a technique proposed by Schiller [114], dual-comb spectroscopy, into the VUV. The principle behind this technique is to compare the heterodyne beatnote between two frequency combs with slightly different repetition frequencies. In the time domain one can consider that, due to the repetition frequency difference, every pair of pulses from the two combs will have a slightly different time separation. Given enough time, these two pulses will scan over each other in exact analogy to an Fourier-transform spectrometer. By extending these ideas to the VUV and XUV, one would be able to examine transitions that are not as narrow as we require for more standard DFCS. Proposals, such as this, are a great example of the versatility and applicability that we expect from XUV frequency combs in the future.

In summary, through the course of this work, we have been able to show a large increase in harmonic flux through intracavity HHG (in the end, more than 10^6 increase in flux at 63 nm). Through these technical advances, we have also demonstrated frequency comb coherence in both the VUV and XUV spectral regions. Finally, we have been able to perform direct frequency comb spectroscopy at a wavelength of 82 nm, as well as observing another atomic transition at 62 nm, opening the door to a wide variety of high resolution laser spectroscopy below 100nm.

Bibliography

[1] T. H. Maiman, "Stimulated Optical radiation in Ruby," Nature **187**, 493 (1960).

[2] A. Javan, W. R. Bennett, and D. R. Herriot, "Population Inversion and Continuous Optical Maser Oscillation in a Gas Discharge Containing a He-Ne Mixture," Phys. Rev. Lett **6**, 106 (1961).

[3] C. H. Townes, "Development of the physics of microwaves, and its unification with infrared and optical science," J. Europ. Opt. Soc. Rap. Public. **5**, 10043s (2010).

[4] R. L. Barger and J. L. Hall, "Pressure Shift and Broadening of Methane Line at 3.39 μ Studied by Laser-Saturated Molecular Absorption," Phys. Rev. Lett. **22**, 4 (1969).

[5] R. W. P. Drever, J. L. Hall, F. V. Kowalski, J. Hough, G. M. Ford, A. J. Munley, and H. War, "Laser Phase and Frequency Stabilization Using an Optical Resonator," App. Phys. B **31**, 97 (1983).

[6] T. Hänsch, I. Shahin, and A. Schawlow, "High-Resolution Saturation Spectroscopy of the Sodium D Lines with a Pulsed Tunable Dye Laser," Phys. Rev. Lett. **27**, 707 (1971).

[7] W. D. Phillips, "Laser cooling and trapping of neutral atoms," Rev. Mod. Phys **70**, 721 (1998).

[8] T. Udem, A. Huber, B. Gross, J. Reicherta, M. Prevedelli, M. Weitz, and T. W. Hänsch, "Phase-Coherent Measurement of the Hydrogen 1S-2S Transition Frequency with an Optical Frequency Interval Divider Chain," Phys. Rev. Lett. **79**, 2646 (1997).

[9] H. Schnatz, B. Lipphardt, J. Helmcke, F. Riehle, and G. Zinner, "First Phase-Coherent Frequency Measurement of Visible Radiation," Phys. Rev. Lett. **76**, 18 (1996).

[10] C. Schwob, L. Jozefowski, B. de Beauvoir, L. Hilico, F. Nez, L. Julien, F. Biraben, O. Acef, J.-J. Zondy, and A. Clairon, "Optical Frequency Measurement of the 2S-12D Transitions in Hydrogen and Deuterium: Rydberg Constant and Lamb Shift Determinations," Phys. Rev. Lett **82**, 4960 (1999).

[11] J. E. Bernard, A. A. Madej, L. Marmet, B. G. Whitford, K. J. Siemsen, and S. Cundy, "Cs-Based Frequency Measurement of a Single, Trapped Ion Transition in the Visible Region of the Spectrum," Phys. Rev. Lett **82**, 3228 (1999).

[12] J. L. Hall, "Optical Frequency Measurement: 40 Years of Technology Revolutions," IEEE J. Sel. Top. Quant. Elec. **6**, 1136 (2000).

[13] W. H. Knox, R. L. Fork, M. C. Downer, R. H. Stolen, C. V. Shank, and J. A. Valdmanis, "Optical pulse compression to 8 fs at a 5-kHz repetition rate," Appl. Phys. Lett. **46**, 1120 (1985).

[14] R. L. Fork, B. I. Greene, and C. V. Shank, "Generation of optical pulses shorter than 0.1 psec by colliding pulse mode-locking," Appl. Phys. Lett. **38**, 617 (1981).

[15] J. G. Fujimoto, A. M. Weiner, and E. P. Ippen, "Generation and measurement of optical pulses as short as 16 fs," Appl. Phys. Lett. **44**, 832 (1984).

[16] R. L. Fork, C. H. B. Cruz, P. C. Becker, and C. V. Shank, "Compression of optical pulses to six femtoseconds by using cubic phase compensation," Opt. Lett. **12**, 483 (1987).

[17] D. E. Spence, P. N. Kean, and W. Sibbet, "60-fsec pulse generation from a self-mode-locked Ti : Sapphire laser," Opt. Lett. **16**, 42 (1991).

[18] G. Mourou, "The ultrahigh-peak-power laser: present and future," Appl. Phys. B. **65**, 205 (1997).

[19] T. Brabec and F. Krausz, "Intense few-cycle laser fields: Frontiers of nonlinear optics," Rev. Mod. Phys. **72**, 545 (2000).

[20] D. J. Jones, S. A. Diddams, J. K. Ranka, A. Stentz, R. S. Windeler, J. L. Hall, and S. T. Cundiff, "Carrier-Envelope Phase Control of Femtosecond Mode-Locked Lasers and Direct Optical Frequency Synthesis," Science **288**, 635 (2000).

[21] T. Udem, J. Reichert, R. Holzwarth, and T. W. Hänsch, "Absolute Optical Frequency Measurement of the Cesium D1 Line with a Mode-Locked Laser," Phys. Rev. Lett. **82**, 3568 (1999).

[22] S. A. Diddams, D. J. Jones, J. Ye, S. T. Cundiff, and J. L. Hall, "Direct Link between Microwave and Optical Frequencies with a 300 THz Femtosecond Laser Comb," Phys. Rev. Lett. **84**, 5102 (2000).

[23] S. T. Cundiff and J. Ye, "Femtosecond optical frequency combs," Rev. Mod. Phys. **75**, 325 (2003).

[24] R. Holzwarth, T. Udem, T. W. Hänsch, J. C. Knight, W. J. Wadsworth, and P. S. J. Russell, "Optical Frequency Synthesizer for Precision Spectroscopy," Phys. Rev. Lett. **85**, 2264 (2000).

[25] T. Udem, R. Holzwarth, and T. W. Hänsch, "Optical frequency metrology," Nature **416**, 233 (2002).

[26] S. S. Schweber, <u>QED and the Men Who Made It</u> (Princeton University Press, 1994).

[27] E. Peik and C. Tamm, "Nuclear laser spectroscopy of the 3.5 eV transition in Th-229," Europhys. Lett. **61**, 181 (2003).

[28] W. G. Rellergert, D. DeMille, R. R. Greco, M. P. Hehlen, J. R. Torgerson, and E. R. Hudson, "Constraining the Evolution of the Fundamental Constants with a Solid-State Optical Frequency Reference Based on the ^{2}29Th Nucleus," Phys. Rev. Lett. **104**, 200802 (2010).

[29] C. J. Campbell, A. G. Radnaev, and A. Kuzmich, "Wigner Crystals of 229Th for Optical Excitation of the Nuclear Isomer," Phys. Rev. Lett. **106**, 223001 (2011).

[30] M. T. Murphy, J. K. Webb, and V. V. Flambaum, "Further evidence for a variable fine-structure constant from Keck/HIRES QSO absorption spectra," Monthly Notices of the Royal Astronomical Society **345**, 609 (2003).

[31] J. K. Webb, J. A. King, M. T. Murphy, V. V. Flambaum, R. F. Carswell, and M. B. Bainbridge, "Evidence for spatial variation of the fine structure constant," Phys. Rev. Lett **107**, 191101 (2011).

[32] A. Marian, M. C. Stowe, J. R. Lawall, D. Felinto, and J. Ye, "United Time-Frequency Spectroscopy for Dynamics and Global Structure," Science **306**, 2063 (2004).

[33] R. J. Jones, K. D. Moll, M. J. Thorpe, and J. Ye, "Phase-Coherent Frequency Combs in the Vacuum Ultraviolet via High-Harmonic Generation inside a Femtosecond Enhancement Cavity," Phys. Rev. Lett. **94**, 193201 (2005).

[34] C. Gohle, T. Udem, M. Herrmann, J. Rauschenberger, R. Holzwarth, H. A. Schuessler, F. Krausz, and T. W. Hänsch, "A frequency comb in the extreme ultraviolet," Nature **436**, 1234 (2005).

[35] R. T. Zinkstok, S. Witte, W. Ubachs, W. Hogervorst, and K. S. E. Eikema, "Frequency comb laser spectroscopy in the vacuum-ultraviolet region," Phys. Rev. A **73**, 061801 (2006).

[36] D. Z. Kandula, C. Gohle, T. J. Pinkert, W. Ubachs, and K. S. E. Eikema, "Extreme Ultraviolet Frequency Comb Metrology," Phys. Rev. Lett. **105**, 063001 (2010).

[37] M. J. Thorpe, K. D. Moll, R. J. Jones, B. Safdi, and J. Ye, "Laser Frequency Combs for Astronomical Observations," Science **311**, 1595 (2006).

[38] K.-K. Ni, S. Ospelkaus, M. H. G. de Miranda, A. Pe'er, Neyenhuis, J. J. Zirbel, S. Kotochigova, P. S. Julienne, D. S. Jin, and J. Ye, "A high phase-space-density gas of polar molecules," Science **322**, 231 (2008).

[39] T. Steinmetz, T. Wilken, C. Araujo-Hauck, R. Holzwarth, T. W. Hänsch, L. Pasquini, A. Manescau, S. D'Odorico, M. T. Murphy, T. Kentischer, W. Schmidt, and T. Udem, "Laser Frequency Combs for Astronomical Observations," Science **321**, 1335 (2008).

[40] S. A. Diddams, "The evolving optical frequency comb," J. Opt. Soc. Am B **27**, B51 (2010).

[41] R. Ell, U. Morgner, F. X. Kärtner, J. G. Fujimoto, E. P. Ippen, V. Scheuer, G. Angelow, T. Tschudi, M. J. Lederer, A. Boiko, and B. Luther-Davies, "Generation of 5-fs pulses and octave-spanning spectra directly from a Ti:sapphire laser," Opt. Lett. **26**, 373 (2001).

[42] A. Bartels and H. Kurz, "Generation of a broadband continuum by a Ti:sapphire femtosecond oscillator with a 1-GHz repetition rate," Opt. Lett. **27**, 1839 (2002).

[43] J. K. Ranka, R. S. Windeler, and A. J. Stentz, "Visible continuum generation in air-silica microstructure optical fibers with anomalous dispersion at 800 nm," Opt. Lett. **25**, 25 (2000).

[44] N. R. Newbury and W. C. Swann, "Low-noise fiber-laser frequency combs," J. Opt. Soc. Am. B **24**, 1756 (2007).

[45] M. C. Stowe, A. Pe'er, and J. Ye, "Control of Four-Level Quantum Coherence via Discrete Spectral Shaping of an Optical Frequency Comb," Phys. Rev. Lett. **100**, 203001 (2008).

[46] A. E. Siegman, Lasers (University Science Books, 1986).

[47] Y. Wang, E. Granados, M. A. Larotonda, M. Berrill, B. M. Luther, D. Patel, C. S. Menoni, , and J. J. Rocca, "High-brightness injection-seeded soft-x-ray-laser amplifier using a solid target." Phys. Rev. Lett **97**, 123901 (2006).

[48] P. Zeitoun, G. Faivre, S. Sebban, T. Mocek, A. Hallou, M. Fajardo, D. Aubert, P. Balcou, F. Burgy, D. Douillet, S. Kazamias, G. de Lacheze-Murel, T. Lefrou, S. le Pape, P. Mercere, H. Merdji, A. S. Morlens, J. P. Rousseau, and C. Valentin, "A high-intensity highly coherent soft x-ray femtosecond laser seeded by a high harmonic beam," Nature **431**, 426 (2004).

[49] Y. Liu, M. Seminario, F. G. Tomasel, C. Chang, J. J. Rocca, and D. T. Attwood, "Achievement of essentially full spatial coherence in a high-average-power soft-x-ray laser," Phys. Rev. A **63**, 033802 (2001).

[50] R. T. Zinkstok, S. Witte, W. Ubachs, W. Hogervorst, and K. S. Eikema, "Frequency comb laser spectroscopy in the vacuum-ultraviolet region," Phys. Rev. A **73**, 061801R (2006).

[51] M. Ferray, A. L'Huillier, X. F. Li, L. A. Lompre, G. Mainfray, and C. Manus, "Multiple-harmonic conversion of 1064 nm radiation in rare gases," J. Phys. B **21**, L31 (1988).

[52] A. L'Huillier and P. Balcou, "High-order harmonic generation in rare gases with a 1-ps 1053-nm laser," Phys. Rev. Lett. **70**, 774 (1993).

[53] K. C. Kulander and B. W. Shore, "Calculations of Multiple-Harmonic Conversion of 1064-nm Radiation in Xe," Phys. Rev. Lett. **62**, 524 (1989).

[54] P. B. Corkum, "Plasma perspective on strong field multiphoton ionization," Phys. Rev. Lett. **71**, 1994 (1993).

[55] K. J. Schafer, B. Yang, L. F. DiMauro, and K. C. Kulander, "Above threshold ionization beyond the high harmonic cutoff," Phys. Rev. Lett. **70**, 1599 (1993).

[56] M. Lewenstein, P. Balcou, M. Y. Ivanov, A. L'Huillier, and P. B. Corkum, "Theory of high-harmonic generation by low-frequency laser fields," Phys. Rev. A **49**, 2117 (1994).

[57] T. Popmintchev, M.-C. Chen, P. Arpin, M. M. Murnane, and H. C. Kapteyn, "The attosecond nonlinear optics of bright coherent X-ray generation," Nat. Phot. **4**, 822 (2010).

[58] L. V. Keldysh, "Ionization in the field of a strong electromagnetic wave," Sov. Phys. JETP **20**, 1307 (1965).

[59] N. B. D. M. V. Ammosov and V. P. Krainov., "Tunnel ionization of complex atoms and atomic ions by an alternating electromagnetic field," Sov. Phys. JETP **64**, 1191 (1986).

[60] P. Balcou, P. Salieres, A. LHuiller, and M. Lewenstein, "Generalized phase-matching conditions for high harmonics: The role of field gradient forces." Phys. Rev. A **55**, 3204 (1997).

[61] E. Constant, D. Garzella, P. Breger, E. Mvel, C. Dorrer, C. L. Blanc, F. Salin, and P. Agostini, "Optimizing High Harmonic Generation in Absorbing Gases: Model and Experiment," Phys. Rev. Lett. **82**, 1668 (1999).

[62] J. J. Carrera, S.-K. Son, and S.-I. Chu, "Ab initio theoretical investigation of the frequency comb structure and coherence in the vuv-xuv regimes via high-order harmonic generation," Phys. Rev. A. **77**, 031401 (2008).

[63] X. M. Tong and C. D. Lin, "Empirical formula for static field ionization rates of atoms and molecules by lasers in the barrier-suppression regime," J. Phys. B **38**, 2593 (2005).

[64] A. LHuillier, P. Balcou, S. Candel, K. J. Schafer, and K. C. Kulander, "Calculations of high-order harmonic-generation processes in xenon at 1064 nm," Phys. Rev. A **46**, 2778 (1992).

[65] M. B. Gaarde and K. J. Schafer, "Quantum path distributions for high-order harmonics in rare gas atoms," Phys. Rev. A **65**, 031406(R) (2002).

[66] J. E. Geusic, H. J. Levinstein, J. J. Rubin, S. Singh, and L. G. V. Uitert, "The Nonlinear Optical Properties of $Ba_2NaNb_5O_{15}$," Appl. Phys. Lett. **11**, 269 (1967).

[67] R. G. Smith, "Theory of intracavity optical second-harmonic generation," IEEE J. Quantum Electron **QE-6**, 215 (1970).

[68] R. J. Jones and J. Ye, "Femtosecond pulse amplification by coherent addition in a passive optical cavity," Opt. Lett. **27**, 1848 (2002).

[69] A. G. Fox and T. Li, "Resonant modes in an optical maser," Bell .Sys. Tech. J. **40**, 453 (1961).

[70] T. Eidam, S. Hanf, E. Seise, T. V. Andersen, T. Gabler, C. Wirth, T. Schreiber, J. Limpert, and A. Tünnermann, "Femtosecond fiber CPA system emitting 830 W average output power," Opt. Lett. **35**, 94 (2010).

[71] J.Tate, T. Auguste, H. G. Muller, P. Salieres, P. Agostini, and L. F. DiMauro, "The Scaling of Wave Packet Dynamics in an Intense Mid-Infrared Field," Phys. Rev. Lett. **98**, 013901 (2007).

[72] A. D. Shiner, C. Trallero-Herrero, N. Kajumba, H.-C. Bandulet, D. Comtois, F. Légaré, M. Giguére, J.-C. Kieffer, P. B. Corkum, and D. M. Villeneuve, "Wavelength Scaling of High Harmonic Generation Efficiency," Phys. Rev. Lett. **103**, 073902 (2009).

[73] B. Bernhardt, A. Ozawa, I. Pupeza, A. Vernaleken, Y. Kobayashi, R. Holzwarth, E. Fill, F. Krausz, T. W. Hänsch, and T. Udem, "Green Enhancement Cavity for Frequency Comb Generation in the Extreme Ultraviolet," CLEO p. QTuF3 (2011).

[74] A. Ruehl, A. Marcinkevicius, M. E. Fermann, and I. Hartl, "80 W, 120 fs Yb-fiber frequency comb," Opt. Lett. **35**, 3015 (2010).

[75] M. Farries, C. Ragdale, and D. Reid, "Broadband chirped fibre Bragg filters for pump rejection and recycling in erbium doped fibre amplifiers," Electron. Lett. **28**, 487 (1992).

[76] T. W. Hänsch and B. Couillard, "Laser frequency stabilization by polarization spectroscopy of a reflecting reference cavity," Opt. Commun. **35**, 441 (1980).

[77] K. D. Moll, R. J. Jones, and J. Ye, "Nonlinear dynamics inside femtosecond enhancement cavities," Opt. Express **13**, 1672 (2005).

[78] K. D. Moll, R. J. Jones, and J. Ye, "Output coupling methods for cavity-based high-harmonic generation," Opt. Express **14**, 8189 (2006).

[79] A. Ozawa, A. Vernaleken, W. Schneider, I. Gotlibovych, T. Udem, and T. W. Hänsch, "Non-collinear high harmonic generation: a promising outcoupling method for cavity-assisted XUV generation," Opt. Express **16**, 6233 (2008).

[80] L. I. Goray, "Numerical analysis of the efficiency of multilayer-coated gratings using integral method," Nucl. Instrum. Methods Phys. Res. A **536**, 211 (2005).

[81] E. D. Palik, <u>Handbook of Optical Constants of Solids</u> (Academic, 1998).

[82] D. C. Yost, T. R. Schibli, and J. Ye, "Efficient output coupling of intracavity high-harmonic generation," Opt. Lett. **33**, 1099 (2008).

[83] Y.-Y. Yang, F. Süßmann, S. Zherebtsov, I. Pupeza, J. Kaster, D. Lehr, H.-J. Fuchs, E.-B. Kley, E. Fill, X.-M. Duan, Z.-S. Zhao, F. Krausz, S. L. Stebbings, and M. F. Kling, "Optimization and characterization of a highly- efficient diffraction nanograting for MHz XUV pulses," Opt. Express **19**, 1954 (2011).

[84] T. Tamir and S. T. Peng, "Analysis and design of grating couplers," App. Phys. **14**, 235 (1977).

[85] I. Hartl, T. R. Schibli, A. Marcinkevicius, D. C. Yost, D. D. Hudson, M. E. Fermann, and J. Ye, "Cavity-enhanced similariton Yb-fiber laser frequency comb: 3 x 10^{14} W/cm^2 peak intensity at 136 MHz," Opt. Lett. **32**, 2870 (2007).

[86] T. R. Schibli, I. Hartl, D. C. Yost, M. J. Martin, A. Marcinkevicius, M. E. Fermann, and J. Ye, "Optical frequency comb with submillihertz linewidth and more than 10 W average power," Nat. Phot. **2**, 355 (2008).

[87] J. Weitenberg, P. Rußbüldt, T. Eidam, and I. Pupeza, "Transverse mode tailoring in a quasi-imaging high-finesse femtosecond enhancement cavity," Opt. Express **19**, 9551 (2011).

[88] A. Vernaleken, J. Weitenberg, T. Sartorius, P. Russbueldt, W. Schneider, S. L. Stebbings, M. F. Kling, P. Hommelhoff, H.-D. Hoffmann, R. Poprawe, F. Krausz, T. W. H. "ansch, and T. Udem, "Single-pass high-harmonic generation at 20.8 MHz repetition rate," Opt. Lett. **36**, 3428 (2011).

[89] M. B. Gaarde, J. L. Tate, and K. J. Schafer, "Macroscopic aspects of attosecond pulse generation." J. Phys. B **41**, 132001 (2008).

[90] D. C. Yost, T. R. Schibli, J. Ye, J. L. Tate, J. Hostetter, M. B. Gaarde, and K. J. Schafer, "Vacuum-ultraviolet frequency combs from below-threshold harmonics," Nat. Phys. **5**, 815 (2009).

[91] J. J. McFerran, W. C. Swann, B. R. Washburn, and N. R. Newbury, "Elimination of pump-induced frequency jitter on fiber-laser frequency combs," Opt. Lett. **31**, 1997 (2006).

[92] I. L. Budunoglu, C. Ulgudur, B. Oktem, and F. O. Ilday, "Intensity noise of mode-locked fiber lasers," Opt. Lett. **34**, 2516 (2009).

[93] H. A. Haus and A. Mecozzi, "Noise of mode-locked lasers," IEEE J. of Quant. Elec. **29**, 983 (1993).

[94] J. T. Verdeyen, <u>Laser Electronics</u> (Prentice Hall, 1995).

[95] C. C. Harb, T. C. Ralph, E. H. Huntington, H.-A. B. D. E. McClelland, and I. Freita, "Intensity-noise dependence of Nd:YAG lasers on their diode-laser pump source," J. Opt. Soc. Am. B **14**, 2936 (1997).

[96] R. Paschotta, "Noise of mode-locked lasers (Part II): timing jitter and other fluctuations," Appl. Phys. B **79**, 163 (2004).

[97] A. Cingöz, D. C. Yost, T. K. Allison, A. Ruehl, M. E. Fermann, I. Hartl, and J. Ye, "Broadband phase noise suppression in a Yb-fiber frequency comb," Opt. Lett. **36**, 743 (2011).

[98] M. Ohtsu, <u>Highly coherent semiconductor lasers</u> (Artech House, 1991).

[99] http://www.layertec.de.

[100] E. P. Kanter, R. Santra, C. Hhr, E. R. Peterson, D. A. A. J. Rudati, E. M. Dufresne, R. W. Dunford, D. L. Ederer, B. Krssig, E. C. Landahl, S. H. Southworth, and L. Young, "Characterization of the spatiotemporal evolution of laser-generated plasmas," J. Appl. Phys. **104**, 073307 (2008).

[101] T. K. Allison, A. Cingoz, D. C. Yost, and J. Ye, "Extreme Nonlinear Optics in a Femtosecond Enhancement Cavity," Phys. Rev Lett. **107**, 183903 (2011).

[102] D. R. Carlson, J. Lee, E. M. Wright, and R. J. Jones, "Intracavity ionization and pulse formation in femtosecond enhancement cavities," Opt. Lett. **36**, 2991 (2011).

[103] R. W. Boyd, "Nonlinear Optics, Second Edition," Nature (Academic, 2003).

[104] J. Lee, D. R. Carlson, and R. Jones, "Intracavity high harmonic generation with fs frequency combs," Accepted to Optics Express (2011).

[105] A. Ozawa, J. Rauschenberger, C. Gohle, M. Herrmann, D. R. Walker, V. Pervak, A. Fernandez, R. Graf, A. Apolonski, R. Holzwarth, F. Krausz, T. W. Hänsch, and T. Udem, "High Harmonic Frequency Combs for High Resolution Spectroscopy," Phys. Rev. Lett. **100**, 253901 (2008).

[106] J. A. R. Samson, <u>Techniques of Vacuum Ultraviolet Spectroscopy</u> (V U V Associates, 1990).

[107] A. D. Ludlow, X. Huang, M. Notcutt, T. Zanon-Willette, S. M. Foreman, M. M. Boyd, S. Blatt, and J. Ye, "Compact, thermal-noise-limited optical cavity for diode laser stabilization at 1×10^{-15}," Opt. Lett. **32**, 641 (2007).

[108] S. A. Diddams, D. J. Jones, J. Ye, S. T. Cundiff, J. L. Hall, J. K. Ranka, R. S. Windeler, R. Holzwarth, T. Udem, and T. Hänsch, "Direct Link between Microwave and Optical Frequencies with a 300 THz Femtosecond Laser Comb," Phys. Rev. Lett. **84**, 5102 (2000).

[109] T. C. Briles, D. C. Yost, A. Cingöz, J. Ye, and T. R. Schibli, "Simple piezoelectric-actuated mirror with 180 kHz servo bandwidth," Opt. Express **18**, 9739 (2010).

[110] G. Scoles, <u>Atomic and molecular beam methods</u> (Oxford University Press, 1988).

[111] L. Minnhagen, "Spectrum and the Energy Levels of Neutral Argon, Ar I," J. Opt. Soc. Am **63**, 1973 (1973).

[112] E. Eyler, D. Chieda, M. Stowe, M. Thorpe, T. Schibli, and J. Ye, "Prospects for precision measurements of atomic helium using direct frequency comb spectroscopy," Eur. J. Phys. D **48**, 43 (2008).

[113] M. Herrmann, M. Haas, U. D. Jentschura, F. Kottmann, D. Leibfried, G. Saathoff, C. Gohle, A. Ozawa, V. Batteiger, S. Knünz, N. Kolachevsky, H. A. Schüssler, T. W. Hänsch, and T. Udem, "Feasibility of coherent xuv spectroscopy on the 1S-2S transition in singly ionized helium," Phys. Rev. A **79**, 052505 (2009).

[114] S. Schiller, "Spectrometry with frequency combs," Opt. Lett. **27**, 766 (2002).